UNIVERSIDADE D
COIMBRA

Alexandra Reis Pereira

INITIAL DEVELOPMENT OF A RAMAN SPECTROMETER FOR MELANOMA DIAGNOSIS APPLICATIONS

Dissertation submitted to the Department of Physics of the Faculty of Sciences and Technologies of University of Coimbra for the degree of Master's in Biomedical Engineering with specialization in Biomedical Instrumentation, supervised by PhD Inês Pereira dos Santos and PhD Pedro Guilherme Vaz

December 2021

1 2 9 0

FACULDADE DE CIÊNCIAS E TECNOLOGIA
UNIVERSIDADE D COIMBRA

Initial Development of a Raman Spectrometer for melanoma diagnosis application

Submitted in Partial Fulfilment of the Requirements for the Degree of Master in Biomedical Engineering in the speciality of Biomedical Instrumentation

Desenvolvimento inicial de um Espetrómetro de Raman para aplicação no diagnóstico de melanoma

Author

Alexandra Reis Pereira

Advisors

PhD Inês Pereira dos Santos

PhD Pedro Guilherme Vaz

Jury

President	**Prof. Dr. Maria Paula Matos Marques**
Advisor	**Prof. Dr. Inês Pereira dos Santos**
Vowel	**Prof. Dr. Francisco Paulo de Sá Campos Gil**

Institutional Collaborations

LIBPhys

LiBPhys-UC

Química-Física Molecular Unidade de I&D

Instituto Química-Física Molecular-UC

Coimbra, December 2021

“If we knew what we were doing, it would not be called research, would it?”

- Albert Einstein

Aos meus avós Elisabete e Alcides

À memória da minha bisavó Maria Idalina

Agradecimentos

O trabalho que aqui se apresenta só foi possível graças à colaboração e apoio de algumas pessoas, às quais não posso deixar de prestar o meu reconhecimento.

Gostava de começar por agradecer aos meus orientadores, Prof. Dra. Inês Santos e Prof. Dr. Pedro Vaz. O vosso conhecimento, apoio e disponibilidade foram fundamentais para a conclusão desta dissertação, que culmina com os inúmeros ensinamentos e aprendizagens que adquiri convosco.

De seguida, gostava de agradecer aos meus colegas de laboratório de Engenharia Física e Biomédica, em especial à Patrícia, por toda a ajuda, amizade e companheirismo durante todo o processo. As nossas horas de almoço de partilhas e gargalhadas serão sempre recordadas como o ponto alto deste último ano.

Um obrigada a todos os colegas e amigos que se cruzaram neste meu percurso académico e que, de algum modo, estiveram presentes e me acompanharam por todas as tradições académicas, bem como os momentos de euforia e exasperação.

Obrigada àqueles que me acompanharam nos programas de intercâmbio universitário em Bolonha e Copenhaga. Foram a minha família durante alguns meses. Grazie! Tak!

Em especial, quero agradecer, às amigas que a Engenharia Biomédica me deu: Ana Catarina, Bea Barros, Bia Martinho, Catarina, Carolina e Mariana, aquelas que sempre estiveram lá para me apoiar, dando-me força para continuar quando mais precisei, e para celebrar comigo cada vitória pessoal e académica ao longo destes 5 anos. Um obrigada enorme pelas inúmeras noitadas de estudo, pelas tantas baladas choradas, pelos outros tantos desabafos e partilhas de frustrações, bem como pelas inúmeras gargalhadas. Que assim continue por muitos anos! Obrigada por serem o melhor que Coimbra me deu.

Queria ainda agradecer à Joana, que mesmo distante fisicamente sempre esteve perto, à distância de uma chamada, para me dar a mão. Obrigada por tudo!

Um agradecimento muito especial à minha família, particularmente aos meus pais, ao meu irmão e aos meus avós, que foram, são e serão sempre o meu suporte. Sem vocês não teria sido possível chegar onde hoje me encontro. Obrigada por me ensinarem

todos os dias que devo lutar pelos meus objetivos e que tenho mais força do que penso. Obrigada pelo amor e apoio incondicional ao longo deste percurso que teve os seus altos e baixos. Saibam que estas vitórias são também vossas. Não há palavras suficientes que demonstrem a minha gratidão, mas deixo-vos a frase que o meu querido avô tantas vezes me diz: *"p'alante es p'allá".*

Por fim, um obrigada a esta cidade que me viu nascer e mais tarde me acolheu como sua estudante. Uma vez Coimbra, Coimbra para sempre!

Abstract

Melanoma is the most aggressive and lethal form of skin cancer. In 2020, there were 324 635 estimated new cases of the disease and 57 043 deaths worldwide for both sexes and all ages. The high mortality rate associated with melanoma is due to (i) its difficult distinction from benign melanocytic lesions (BML), (ii) the current standard diagnosis being solely morphology-based, and (iii) its high metastatic propensity. Consequently, clinical diagnosis of melanoma often leads to unnecessary resections of benign lesions and, worse, missing early-stage lesions, melanoma *in situ* (MIS). Diagnosis of MIS lesions is extremely important since they are non-invasive melanomas that can be treated by a complete resection of the lesion, with a success rate of 97% 5-years.

Raman Spectroscopy (RS) is an objective, non-invasive and non-destructive optical vibrational spectroscopic technique that gives insight into the biochemical composition of the sample. Because of its great potential, it has been increasingly employed in biomedical applications to complement the clinical diagnosis of early-stage diseases or to assist oncological surgery guidance.

The main objective of the presented dissertation is the initial development of a Raman spectrometer that can detect early-stage melanomas, providing a simple, fast and operator-independent diagnosis to assist clinicians in the clinical setting. This spectrometer will use a near-infrared (NIR) laser and operate in the high wavenumber (HWVN) region of the spectrum to avoid tissue autofluorescence. This region was used effectively to distinguish MIS from BML in the past.

In this work, all the components needed for this instrument were selected, and the Raman spectrometer was simulated using the *3DOptix* software. Considering the knowledge acquired during the simulation, the initial prototype was assembled in the optical table. Additionally, alignment and calibration procedures were carried out using several lamps (neon, halogen and mercury (Hg)). Finally, the built-in Raman spectrometer was tested with a cyclohexane sample.

The calibration was fully accomplished with a detection range from 487 to 1100nm and an experimental resolution of less than 3 nm with the Hg lamp. However,

although the built-in spectrometer has successfully detected the Hg lamp's spectrum, it was not sensitive to the Raman signal of a cyclohexane's sample. Hence, it was concluded that the used detection system (CMOS sensor) needs to be replaced by a more sensitive detector, such as InGaAs array detector, which has higher sensitivity to signals with longer wavelengths (above 1100 nm), in order to detect weak signals such as Raman signals.

Keywords Raman Spectroscopy, Melanoma, Optical diagnosis, High wavenumber region, Near-infrared laser

Resumo

O melanoma é o cancro da pele mais agressivo e letal. Em 2020, o número estimado de novos casos foi de 324 635 e 57 043 pessoas (de ambos os sexos e todas as idades) morreram no mundo da doença. A elevada letalidade deve-se (i) ao facto de o melanoma ser de difícil distinção em relação a outras lesões melanocíticas benignas, (ii) ao seu diagnóstico ser apenas baseado em aspetos morfológicos, e (iii) à sua alta probabilidade de metastização. Consequentemente, o processo de diagnóstico de melanoma leva a: excisões desnecessárias de lesões benignas e, mais grave, à não identificação de lesões em estado inicial, ou seja, melanomas *in situ* (MIS). O diagnóstico de MIS é de extrema importância, uma vez que, sendo lesões não invasivas que podem ser tratadas através de uma excisão completa da lesão, apresentam uma taxa de sucesso de cura de 97% a 5 anos.

A espetroscopia de Raman é uma técnica ótica de espetroscopia vibracional objetiva, não-invasiva e não-destrutiva que fornece informação da composição bioquímica de uma amostra. Como consequência do seu grande potencial, tem sido cada vez mais usada em aplicações biomédicas para complementar o diagnóstico clínico de doenças em fase inicial ou para assistir na orientação da cirurgia oncológica.

O objetivo principal apresentado nesta dissertação é desenvolver um espetrómetro de Raman inicial, simples, com aquisições rápidas, independente do operador e que permita detetar lesões MIS, assistindo clínicos no diagnóstico em ambiente de consulta. O espetrómetro irá incluir um laser na zona do infravermelho próximo e analisar a região espetral dos elevados números de onda, de forma a evitar a influência da autofluorescência dos tecidos pigmentados no sinal adquirido. Esta região espetral já provou ser suficiente para distinguir lesões MIS e lesões melanocíticas benignas.

Nesta dissertação, todos os componentes necessários foram selecionados e, de seguida, a montagem do espetrómetro de Raman foi simulada no software *3DOptix*. Considerando o conhecimento adquirido durante a simulação, o protótipo foi implementado na mesa ótica. De seguida, foram realizados procedimentos de alinhamento e calibração, usando lâmpadas de elementos químicos (halogéneo, néon e mercúrio (Hg)). Finalmente, o espetrómetro Raman desenvolvido foi testado com uma amostra de ciclohexano.

A calibração do espetrómetro foi realizada com sucesso, tendo sido obtida uma região de deteção entre os 487 e 1110 nm e uma resolução experimental de menos de 3 nm com a lâmpada de Hg. Embora o espetrómetro desenvolvido tenha detetado com sucesso o espetro da lâmpada de Hg, o mesmo não foi possível com o sinal Raman de uma amostra de ciclohexano. Assim, concluiu-se que o sistema de deteção utilizado (sensor CMOS) terá de ser substituído por um detetor mais sensível, como um detetor de InGaAs, que tem maior sensibilidade para sinais de comprimentos de onda mais longos (acima de 1100 nm), a fim de detetar sinais fracos como o sinal Raman.

Palavras-chave: Espetroscopia de Raman, Melanoma, Diagnóstico ótico, Região de elevados números de onda, Laser infravermelho próximo

Contents

List of Figures

List of Tables

List of Acronyms

AF – Autofluorescence

BML – Benign Melanocytic Lesions

CARS – Coherent Anti-Stokes Raman Spectroscopy

CCD – Charge Coupled Device

CI – Confidence Interval

CMOS – Complementary Metal Oxide Semiconductor

CS – Compressive Sensing

DFS- Detector Fixation System

DMD – Digital Micromirror Device

DOS – Diffuse Optical Spectroscopy

DRS – Diffuse Reflectance Spectroscopy

EIS – Electrical impedance Spectroscopy

EMSC – Extended Multiplicative Scatter Correction

FS – Fluorescence Spectroscopy

FT-Raman – Fourier Transform Raman

HWVN – High Wavenumber

InGaAs – Indium-Gallium-Arsenide

IR – Infrared

LIFS – Laser-induced Fluorescence Spectroscopy

MI – Multiphoton Imaging

MIS – melanoma *in situ*

NIR – Near-infrared Region

OCT – Optical Coherence Tomography

OD – Optical density

OFS – Optical Fibre System

RCM – Reflectance confocal microscopy

ROI – Region of Interest

RS – Raman Spectroscopy

SERDS – Shifted Excitation Raman Difference Spectroscopy

SERS – Surface-enhanced Raman Spectroscopy

SLM – Spatial Light Modulator

SNR – signal-to-noise ratio

SPI – Single-Pixel Imaging

SRS – Stimulated Raman Scattering

SWIR – Short-wavelength near-infrared

USC – Universal Sample Cage

UV – Ultraviolet

VS – Vibrational Spectroscopy

1. INTRODUCTION

Chapter 1 is subdivided into four parts: 1.1 consists in the description of the problem addressed in this dissertation. Then, in 1.2, the proposed goals are presented. Following, in 1.3, the structure of this work is described, and, finally, in 1.4, the institutions involved in the execution of this project are introduced.

1.1. Motivation

Melanoma is the most aggressive and lethal form of skin cancer [1]. It is a neoplasm characterized by the proliferation of malignant pigment-producing skin cells, the melanocytes [2]. In 2020, the estimated number of new cases of melanoma was 324 635, and 57 043 have died from the disease worldwide for both sexes and all ages [1].

Melanoma lesions can be classified as: (i) non-invasive, meaning that the lesions are still confined to the epidermis, known as melanoma *in situ* (MIS), or (ii) invasive when malignant melanocytes have penetrated the basal layer into the dermis (and subsequently able to disseminate to distant organs, as a metastatic disease).

When melanoma is diagnosed at an early-stage, such as MIS, the rate of survival is high by performing a complete surgical excision (5-year survival rate of 97%), being MIS considered a curable disease upon surgical resection [3], [4]. However, melanomas detected in advanced stages have a much poorer prognosis with a severely higher mortality rate, due to the risk of metastasis, which makes melanoma to be considered a life-threatening disease [1], [5]. Therefore, the detection of early-stage melanomas is crucial to increase the survival rate of these patients.

Also, cutaneous melanoma lesions are often difficult to identify given the variations in colour, size and morphology, being similar to benign melanocytic lesions (BML) and so, minor feature differences are worthy of clinical attention [6], [7].

Currently, clinical diagnosis is done by a physician through direct observation of lesions. Dermatologists can be assisted by some tools based on morphological features [8]. However, due to melanoma difficult distinction, the dermatologists' sensitivity to detect melanoma, even with the help of those morphology-based tools, is only 69-96%, and the specificity is 3.7-66% [9]. Moreover, primary care practitioners have an even lower

performance. Consequently, 30% of early-stage melanomas, MIS, are missed in first inspections, which represents a risk of disease progression to a metastatic stage [10]–[12].

Due to its risk of progression to a lethal metastatic disease, all lesions suspected of being malignant are surgically excised. This leads to many unnecessary excisions of BML for histopathology examination and, due to poor clinical sensitivity, to missing early-stage lesions. Hence, the number of excisions of malignant lesions at more advanced stages will increase and, consequently, resulting in poorer patient prognosis.

The available add-on tools to assist dermatologists in the clinical diagnosis of melanoma are based on morphological features (dermoscope) or visual inspection algorithms (e.g., ABCDE, CUBED, and other similar ones) [5], [8], [13]. Thus, other techniques are being investigated based on non-invasive imaging/electrical data acquisitions, such as reflectance confocal microscopy, electrical impedance spectroscopy combined with digital dermoscopy, optical coherence tomography, cross-polarized light and fluorescence photography, and high-frequency ultrasound [5]. Nonetheless, some of these techniques are morphology-based, dependent on the operator sensitivity/training to differentiate lesions or/and the measurement is too burdensome [13].

Raman spectroscopy (RS) is an optical spectroscopic technique that can non-invasively and non-destructively assess the biochemical composition of a sample. It has increasingly been used in the medical field to complement the diagnosis since it provides objective information about tissues [14]. Due to its non-invasiveness and ability to be used *in vivo*, it is an excellent candidate technique to assist melanoma diagnosis. Concerning this, Raman instruments have already proved to be suitable to diagnose melanoma with high accuracy, meaning that the distinction between non-melanoma lesions, *nevi* and melanoma can be improved, leading to high diagnostic specificity and sensitivity (some studies report sensitivities of 100%) [13], [15].

However, RS has a main challenge when applied to pigmented tissues, which is laser-induced tissue autofluorescence, that is orders of magnitude more intense than Raman signal, and consequently able to superimpose to the Raman signal [16]–[19]. Several strategies have been implemented, nonetheless, the more prone to avoid this issue is shifting the excitation wavelength to the near-infrared region (NIR), combined with analysing the high wavenumber (HWVN) region of the spectrum, instead of the most used fingerprint

region [16]. This approach has been used before in the differentiation between melanoma (including in situ) and BML clinically suspected for melanoma, with good results [20], [21].

Typically, Raman spectrometers are combined with Charge Coupled Devices (CCD) or Indium-Gallium-Arsenide (InGaAs) detectors. However, these detectors have some problems: CCDs only detect until 1100 nm, which is inefficient for analysing the high wavenumber region of NIR-spectrometers, and InGaAs detectors are very noisy or expensive, which will lead to longer acquisition times [18], [22], [23]. Although some of the problems have been solved, currently used Raman spectrometers have other limitations that make them still non-compatible with the clinical setting: need of a detector-cooling system, expensive instrumentation, and large acquisition times, due to analysis of the entire Raman spectrum [18], [22], [24].

Therefore, there is an emerging pressing need for fast, accessible, without need for a cooling system and more efficient Raman instruments, that provide the much-needed objectivity to clinical diagnosis for biomedical and clinical applications, namely *in vivo* and *ex vivo* diagnosis of (pre)-malignant lesions in various types of (pigmented) tissues.

Compressive sensing (CS) is a methodology that allows signal reconstruction using a restricted subset of samples, *i.e.,* for RS applications, it can be implemented to select the region of the spectrum with more significance to the analysis, eliminating the need to analyse the full spectrum range [24]. One of the CS applications is single-pixel imaging [25]. Therefore, single-pixel compressive sensing is very interesting for Raman imaging due to being inexpensive and having short computational reconstruction times, and consequently, enabling real-time applications [24].

1.2. Goals

The conditions presented above confirm the considerable impact that melanoma has on patients' mortality, prognosis and quality of life, as well as dermatologists' difficulties to diagnose the disease at an early, *i.e.,* curable, stage.

Our proposal is to build an easy to operate, more affordable and faster Raman instrument tailored for melanoma diagnosis. This will give dermatologists an answer to their needs: an add-on tool that helps to differentiate melanoma from suspicious melanocytic lesions based on disease-prompted biochemical changes, rather than technologies based on

subjective morphological criteria. Additionally, we expect that this tool will also be suitable for diagnoses in a routine check-up with general practitioners.

This proposal, based on the spectrometer developed in the RASKIN project by the University of Rotterdam [15], [20], [26], aims at the initial development of a NIR-Raman spectrometer operating in the HWVN region of the spectrum, applying CS based on spectral multiplexing by spatial light modulators (as a Digital Micromirror Device - DMD) and on single-element detection (photodiode).

The detector element used in the RASKIN project will be substituted by a compressive element, *i.e.*, a single-pixel detector coupled with a light modulator for sparse sampling. This will allow a signal reconstruction using only a subset of specific wavelengths (1300 to 1550 nm, using a 976 nm excitation wavelength laser). In this way, in contrast with other detector systems, there will be no spatial scanning and the acquisition time will be shorter, hence, suitable for clinical applications. In addition, the DMD is a modulator with a fast and low-cost programmable spatial light modulator, which will be less expensive and discard the need for a cooling system.

In line with the final objective of this project, the main objective of this dissertation is developing an initial Raman spectrometer, without the compressive element, operating in the HWVN region of the spectrum, the establishment of alignment and calibration protocols so that in the future, it can be updated and improved to a compressive Raman spectrometer. Such a simplified device would considerably promote a routine implementation of the spectroscopic technique in the clinical arena, as in the early-cancer diagnosis of melanocytic lesions, MIS.

1.3. Dissertation Structure

The dissertation presented is subdivided into five chapters:

- **Chapter 1: Introduction –** description of the motivation for the development of this work, as well as the objectives and the description of the research units involved.
- **Chapter 2: State of the art –** contextualization of the problem of melanoma disease and presentation of some non-invasive techniques ongoing investigation. Then, the challenges and the strategies to solve RS issues are discussed, in particular, the fluorescence problem in biological tissues. In addition, Raman spectrometers developed in the past for melanoma applications and studies are presented. Finally, the usage of Raman compressive sensing and its advantages are addressed.

- **Chapter 3: Material and Methods –** presentation of the requirements for melanoma applications. The mathematical approach of the technique is also presented. Presentation of the components used to develop the NIR-Raman Spectrometer, as well as the 3D parts developed to allow low tolerance variations. Finally, presentation of the alignment and calibration protocols.
- **Chapter 4: Results and Discussion –** presentation and discussion of the simulation results and the experimental results of the assembled physical setup (prototype) and calibration of the spectrum. Finally, presentation and discussion of the experimental test with a Raman standard sample (cyclohexane).
- **Chapter 5**: **Conclusions and Future Work –** report of the final remarks and conclusions to be drawn from the work developed. Lastly, some improvements are proposed to be done in the continuity of this project, to overcome some of the limitations found.

1.4. Host Institutions

The development of the project is a collaboration between two research units of the University of Coimbra (UC): The Laboratory for Instrumentation, Biomedical Engineering and Radiation Physics (LIBPhys), and the Molecular Physical-Chemistry R&D Unit (QFM).

LIBPhys is a research centre where the R&D activities are integrated into the atomic, molecular, nuclear physics, and electronics instrumentation fields, with applications to analytical methods, radiation detection, and biomedical engineering. The group includes researchers from three Portuguese institutions: University of Coimbra, University of Lisbon, and Nova University of Lisbon.

QFM-UC is a research unit of the optical vibrational spectroscopy field, with laboratories for chemical preparation and characterization and for cell culture, allowing an excellent interplay between physical-chemical methods and biological approaches. The team members are researchers specialized in the study of biological/pharmaceutical systems, the development of metal-based anticancer agents and chemopreventive food products. QFM-UC network is extensive with researchers in (inter)national collaborations programs.

2. STATE OF THE ART

Chapter 2 is subdivided into two parts: the first section, in 2.1 and 2.2, both the skin structure, disease and its origin are presented, followed by the gold-standard diagnosis procedure and treatments and finally, in 2.3, some of the new non-invasive diagnostic technologies are reviewed. In the second section, in 2.4, the technique proposed to diagnose melanoma, Raman Spectroscopy (RS), is thoroughly exposed. Then, the basic concepts, conventional configuration and the challenges of the RS concerning tissue fluorescence are addressed. At last, the state of the art of RS applied to melanoma diagnoses is reviewed. Lastly, in 2.5, compressive sensing and its advantages are briefly introduced regarding RS applications.

2.1. Human Skin: Anatomical Structure

The skin is the most external organ of the human body. It acts as a physical barrier with a multitude of functions, such as regulating temperature, preventing the internal structure of contact with pathogens, toxins, and microorganisms from the surrounding environment, or protecting from injuries, trauma and ultraviolet (UV) radiation. The skin is divided into 3 layers: an internal layer, called subcutaneous tissue or hypodermis, a middle layer, named dermis, and a superficial layer, the epidermis, as depicted in Figure 2.1. The thickness of the skin varies depending on the body area: epidermis can be 50 μm (eyelids), reaching up to 1.5 mm on the feet soles and hand palms, and dermis can vary between 1 mm (eyelids) to 5 mm (back skin) [27], [28].

The hypodermis consists of fat and connective tissue, and it is highly connected to the dermis by a rich vascular and lymphatic system. The dermis is the epidermis' permeable supporting matrix, constituted of polysaccharides and protein fibres, such as elastin, which ensures the elasticity, and collagen, which adds great tensile strength to the skin and constitutes up to 30% of its volume (with 15% of Type I collagen) [28], [29]; dermis also contains fibroblasts, mast cells, histiocytes, hair follicles, and sweat glands [28]. The dermis is subdivided into two sections: a first thinner layer, the papillary dermis, above a thicker one, the reticular dermis. The two layers are composed, respectively, of loose and dense connective tissue, and are interconnected by blood and lymphatic vertical vessels.

The epidermis is a waterproof barrier and has a substantial contribution to skin tone [29]. The epidermis is a non-vascularized stratified squamous epithelium, composed of

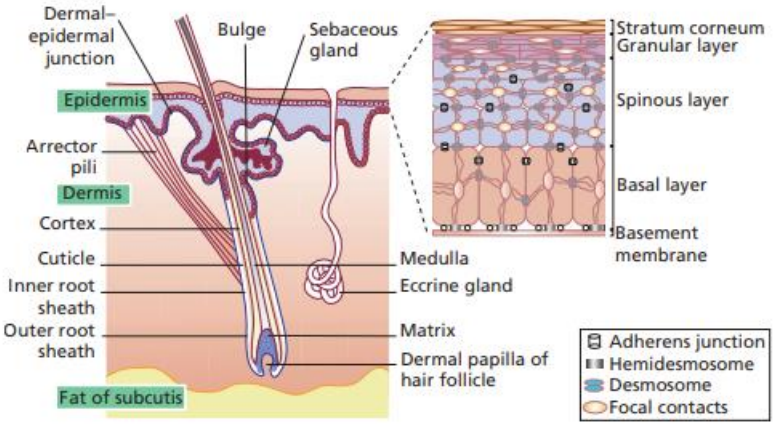

Figure 2.1 - Skin structure. The three main layers, in descending order, are the epidermis (separated by the dermal-epidermal junction from the next layer), the dermis and the hypodermis layer. The inset shows the different types of layers within the epidermis: *stratum corneum*, granular layer, spinous layer, basal layer and finally, basement membrane [28].

four types of cells: (i) keratinocytes, the most numerous epidermis' organelle, responsible for the regeneration of the skin; (ii) melanocytes, pigment-producing cells that determine skin tone, typically located at the basal layer; (iii) Langerhans cells, antigen-presenting cells with immunological functions; and (iv) Merkel cells, receptors of epidermal pressure changes [28]–[30]. The epidermis is characterized by the predominance of keratinocytes cells in a portion of 30 to 50 for each unit of melanocytes [2], [30]. The keratinocytes are responsible for the synthesis of keratin and the active regeneration and replacement of epidermis components, which lasts approximately 30 days. This is a consequence of keratinocytes' recurrent process of production, migration (to upper layers) and desquamation, which also contributes to distinguishing four epidermic layers: *stratum basale* (basal layer), *stratum spinosum* (spinous layer), *stratum granulosum* (granular layer), and *stratum corneum* (Figure 2.1) [28]. In some areas, such as hand palms or feet soles, the epidermis has one more layer called *stratum lucidum*, characteristic of thick skin [29], [30].

2.1.1. Melanin Production

Melanin is a polymer produced by melanocytes that absorbs light and, hence, is directly related to the photoprotection of skin [2], [30].

Melanocytes have the ability to elongate their dendrites to surrounding keratinocytes to transfer melanosomes, organelles responsible for producing and transferring melanin [28], [29]. Once in the keratinocytes, melanosomes from supranuclear layers protect their nucleus from exposure to UV rays, since melanin can absorb light of wide wavelength

spectrum, from (i) long-wavelength UV (designated UVA), responsible for skin-induced pigmentation/tanning and for actinic, *i.e.*, ageing skin, to (ii) short wavelengths UV with higher energy (named UVB), which can cause damage in tissues, such as sunburns or mutations [29], [30].

Considering that DNA has the propensity to absorb UV radiation, melanin assumes a relevant role in the protection of the cells' nuclear content. DNA mutations constitute a risk factor for the occurrence of skin cancer, in particular melanoma, if the alteration occurs in the melanocyte [2], [31].

2.2. Melanocytic Lesions: *nevi* and melanoma

There are several types of skin cancer depending on the type of cells that became malignant. Melanoma is the type of skin cancer originating from melanocytes and is characterized by an abnormal growth of these cells, as depicted in Figure 2.2. This unexpected process of melanocytes mitosis can form nests in the epidermis (starting near the dermo-epidermal junction) and reach the dermis [2].

In the case where nests are composed of benign melanocytes, is called benign melanocytic nevocites or simply melanocytic *nevi*. A common nevus, also known as a mole, is uniformly pigmented, with a diameter of less than 6 mm, and flat or narrowly heightened [30]. However, if severe cell dysplasia happens in these nests, the tumour can become malignant, with invasive ability, and is called melanoma [2]. However, melanoma lesions and benign melanocytic lesions (BML) are difficult to discriminate due to their similar appearance.

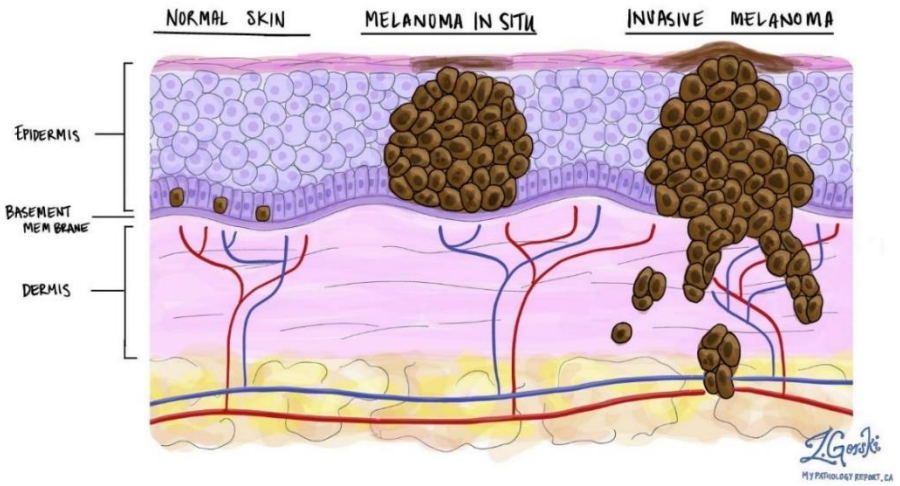

Figure 2.2 – Melanoma progression stages. In early-stages, malignant melanocytes proliferate horizontally and vertically within the epidermis (MIS). In a later stage, malignant melanocytes transpose the basal layer and invade the dermis, exhibiting metastatic ability (invasive melanoma) [32].

Concerning melanoma lesions, as the malignant melanocytes are still confined to the epidermis, as represented in Figure 2.2, the lesions are known as melanoma *in situ* (MIS) and are considered early-stage melanomas. When left untreated, MIS can evolve to more advanced stages, exhibiting metastatic ability, *i.e.*, invasive melanomas, which are characterized by malignant melanocytes penetrating the basal layer into the dermis (and other distant organs), as shown in Figure 2.2.

The prognosis of melanoma is influenced by some tumour parameters: ulceration, dermal mitosis, and Breslow thickness [33]. The Breslow thickness is the vertical depth of growth (in μm) and is associated with the metastatic propensity and aggressiveness of melanomas (Figure 2.3) [8]. Other parameters also used are Clack's levels, as also represented in Figure 2.3.

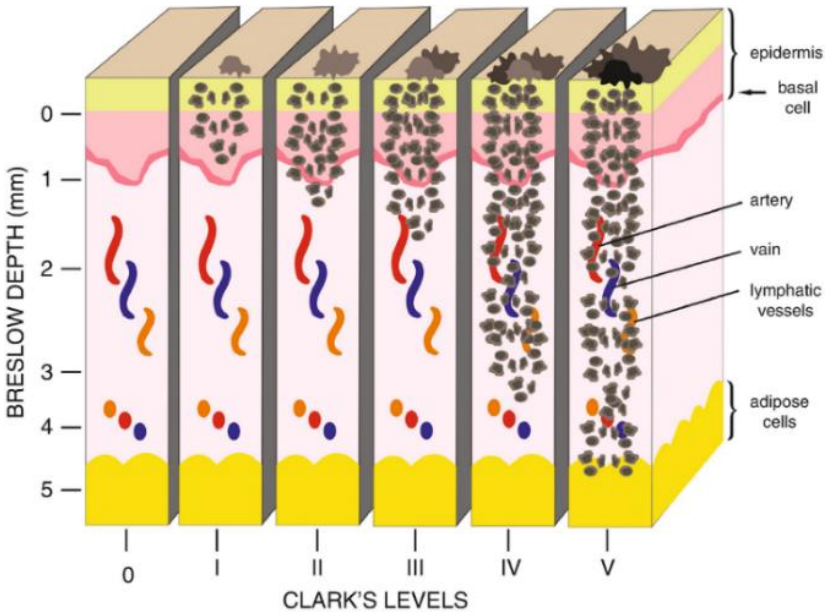

Figure 2.3 – Schematic figure of Breslow thickness. Increments in Breslow thickness are associated with more advanced stages of melanoma and, consequently, to poorer prognosis [34].

Melanoma is the most aggressive and lethal form of skin cancer with a progressive incidence in the last decades [1]. In 2020, the estimated number of new melanoma cases was 324 635 and 57 043 people have died from the disease worldwide [1]. The outgrowth of the number of cases in the last decades is controversial since is not proved to be caused by the upgrade of diagnosis tools, that allow the discovery of more malignant lesions, or due to the more thorough surveillance made to patients with higher risk, such as melanoma patients relatives [35]. Furthermore, patients with MIS have a 97% of 5-year

survival rate [4]. In contrast, patients with melanomas with Breslow thickness larger than 0.8 mm have a reduced 5-year survival rate of only 30% [8], [36].

2.2.1. Risk Factors

The major risks factors to develop melanoma are the density of benign *nevi* and the presence of dysplastic *nevi* [6], [31]. Also, patients with family members who had a melanoma may be at a higher risk, since mutations in CDKN2A or CDK4 genes could be inherited [6]. Another gene mutation that exceeds 50% of the melanoma cases is the activated BRAF gene, which causes deregulation of the proliferation, differentiation and survival of cells [37]. Furthermore, patients who had a primary melanoma have a higher risk of developing a second tumour in more advanced stages [4].

Also, individuals with melanocortin-1 receptor (MC1R) gene variants, *i.e.*, people that have lighter skin tones, and so, with lower levels of melanin, have more propensity than individuals with darker skin, with higher levels of melanin [30], [31]. Moreover, the incidence of melanoma is from 3% to 7% higher in the caucasian population, compared with the remaining population, and the tendency is to increase the percentage in the next decades [33].

Ultimately, prolonged and unprotected exposure to intense UV light may increase the risk of developing melanoma for two reasons: (i) sun exposure increases the rate of production of melanocytes and (ii) UVB rays are a trigger to mutations in DNA [2], [6]. Hazard UV light exposure can develop a large number of reactive species of oxygen, resulting in a cellular lesion and leading to the beginning of the carcinogen process [2]. The most frequent lesion site seems to confirm the influence of the hazard effect of UV light since melanomas are more common in men's back, and in lower extremities in women (42%) [6]. These factors could be the reason for higher disease frequency in regions with sun-exposure practices within the population activities, such as the use of solariums and unprotected exposer to the sun [2].

2.2.2. Conventional Melanoma Diagnosis and Treatment

The diagnosis of melanoma is usually done by direct observation of the lesion by a dermatologist or general practitioner. The clinician naked-eye observation of the lesions can be assisted by a dermoscope and some algorithms, which are tools based only on

morphological features [5]. The dermoscope can also be supported by automated systems, called digital dermoscope, such as the commercialized instrument SolarScan (Polartechnics Ltd, Sydney, Australia) [38]. There are some algorithms, such as routine self-skin examination or the ABCDE rule, which summarized some of the most common features of a melanoma: "A" for the asymmetry of the shape; "B" for the irregular borders; "C" for the pigmentation colour variegation of the lesion; "D" for the dimension larger than 6 mm, and, finally, "E" for the time evolution of the lesion [6], [8]. Other algorithms that are not so commonly used, such as CUBED algorithm, also rely only on the features of melanoma: "C"olor different from skin tone, "U"ncertain diagnosis, "B"leeding lesions, "E"nlarging lesions regardless of therapy, "D"elay in cicatrisation farther than 2 months [8].

If the clinician suspects that the lesion presented is malignant, complete surgical excision is performed. The clinical diagnosis is only confirmed when the histopathology analysis of the surgical excision is positive (2011 AAD CPG[1] entity recommends for MIS and invasive lesions, permanent formalin-fixed paraffin-embedded sections, being the current gold-standard procedure for histopathological diagnosis) [4], [5], [8]. The histopathology also confirms if the peripheral margin (dependent on the stage of the disease, usually between 1 and 3 mm around the lesion) was accomplished [5]. Furthermore, based on the fact that melanoma lesions are difficult to distinguish from BML, this diagnosis procedure leads to unnecessary removal of several non-malignant lesions for histopathological examination and moreover, malignant lesions can be missed [5], [8]. Furthermore, this process is invasive, time-consuming and also a financial burden for patients and health services [7].

The detection of early-stage melanomas (MIS) is crucial to increase the survival rate of these patients, due to the high rates of mortality and morbidity of melanoma [1]. Compared to more advanced stages, MIS diagnosis can improve the life expectancy and quality of life of patients, as the diagnose can be done earlier than the appearance of symptoms, while the tumour is not invasive and can be treated locally in the clinical setting, since MIS are considered curable after complete surgical resection [5]. In contrast, advanced forms of melanoma may need aggressive and invasive strategies to treat metastasis, such as, definitive surgery removal, immunotherapy, novel targeted therapies, chemotherapy and/or radiation therapy, which can be avoided by early detection of malignant lesions [5], [35].

[1] American Academy of Dermatology Clinical practice guidance

Several terms are related to the performance of a diagnostic test (as is the clinical diagnosis of melanoma): sensitivity, specificity and predictive values (negative and positive) [11]. Sensitivity and specificity increase when more diagnostic tools are used or criteria are followed [8].

Sensitivity measures the ability to correctly detect people with the disease, *i.e.*, it is given by the ratio of correctly diagnosed melanomas (confirmed by histopathology) over the total number of melanoma lesions that were excised. The sensitivity for clinical observation diagnosis of melanoma varies on the skills of the clinician. Hence, Chen *et al.*, in 2001, compared the performance of clinicians in diagnosing melanoma and reported that experienced dermatologists achieve a higher sensitivity for melanoma diagnosis (81% to 100%) than primary care physicians (42% to 100%) [10].

Specificity is the ability to exclude people who do not have the disease and is determined as the ratio of correctly classified non-melanoma cases (confirmed by histopathology) out of the total number of non-melanoma lesions.

The predictive values indicate the probability of the diagnostic result to be correct, *i.e.*, the predictive positive value is the percentage of times that the operator correctly identifies the disease as true positive cases out of the total number of lesions analysed. Similarly, the negative predictive value is the opposite. It indicates the probability that the person, whose result to the test is negative, does not have the disease.

Nevertheless, due to melanoma difficult distinction from other pigmented lesions, a more recent study concluded that the experienced dermatologists' sensitivity to detect cutaneous melanoma, even with teledermoscopy tools, is only 69-96% and specificity is as low as 3.7-66% [9].

2.3. New Non-invasive Add-on Tools for Melanoma Diagnosis

Dermoscopy, as presented before, continues to be the gold standard add-on tool to assist dermatologists and general practitioners in the clinical diagnosis of melanoma. However, the tool only magnifies the lesion and reduces light reflection on the skin surface, adding little insight into the depth of lesions [39]. The investigation in this field is ongoing and some of the non-invasive techniques explored for melanoma diagnosis are presented in Table 1. The existing technologies under investigation for melanoma diagnosis can be

divided into: electrical, thermal, optical, genomic and computational. The optical techniques can be also subdivided into optical imaging and optical spectroscopy techniques [40].

Table 1 – New non-invasive diagnostic tools for melanoma. Some of which are already approved by the FDA[2]. Adapted from [5]

Optical	Optical Imaging	• Reflectance Confocal Microscopy (RCM) [41] • Multiphoton imaging (MI)[42] • Optical Coherence Tomography (OCT) [43]
	Optical Spectroscopy	• Fluorescence Spectroscopy (FS) [44] • Raman Spectroscopy (RS) [26] • Fourier Transform Raman (FT-Raman) [45] • Diffuse Reflectance Spectroscopy (DRS) [44], [46] • Diffuse Optical Spectroscopy (DOS) [47]
Electrical	• Electrical Impedance Spectroscopy (EIS) [48], [49] • EIS combined with digital dermoscopy [50]	
Genomic	• Adhesive patch ‘‘biopsy’’ [51]	
Thermal	• Thermal imaging cameras [52]	
Computational	• Artificial Intelligence-based deep learning algorithms [53], [54] • Smartphone-aided diagnosis [55]	

Electrical technologies measure the skin electrical properties, and an example is Electrical Impedance Spectroscopy (EIS) [48], [49]. Although EIS’s high sensitivity, this technique has low specificity. Also, the electrodes limit the examination for difficult access body sites (e.g., ears) and do not cover entirely the lesion, consequently, several measurements are required [40]. Then, the time used in the examination is extended, making electrical technologies not suitable for clinical use [40]. Nonetheless, some investigations have been working to combine EIS with digital dermoscopy in order to improve the diagnose performance, especially EIS’s specificity [50]. However, the value is still low, as reported by Rocha et. al, 69.5% for melanoma diagnose [50].

Genomic technologies analyse the mRNA of melanocytic lesions cells, particularly using adhesive patches to collect cells from the surface of those lesions. After the cells’ extraction, an mRNA molecular signature analysis is needed to evaluate the malignancy of the lesion, making this procedure time-consuming. Although this practice can achieve high sensitivity and specificity (97.6% and 72.7%) [51], without the need to cut the

[2] FDA - Food and Drug Administration

lesion (resection), it is not a real-time procedure. Furthermore, it is still not applicable to diagnose MIS lesions, since molecular differences between MIS and invasive lesions have not been validated. However, a pilot test during the COVID-19 pandemic for telemedicine dermatologist appointments used the adhesive patches method, so patients could self-sample the suspected lesions with guidance from their clinician and the authors reported reduced patient anxiety with a negative predictive value of more than 99% [56].

Another method is thermal technologies. Those rely on tissue metabolic activity characteristics, e.g., pixel temperature profiles, which can differentiate benign and melanoma lesions using thermal imaging cameras [52]. Although this technology, has short acquisition times (total examination time of 5 min) and without skin contact, it requires the patient to be extremely still during the exam in order to eliminate artefacts. Consequently, a data-processing pipeline is vital [40].

Another technology with application to melanoma is smartphone-aided diagnosis [55]. However, it still needs further evaluation since no rigorous proof of concept exists in the literature [57]. Also, in the last years, studies based on deep-learning algorithms [53], [54] have been increasing in number with promising performances. Nonetheless, clinical validation of their use is missing.

Concerning optical methods, some have been used for melanoma imaging diagnoses, such as Multiphoton imaging (MI) [42], Optical Coherence Tomography (OCT) [58] or Reflectance Confocal Microscopy (RCM) [41]. Furthermore, these techniques have some clinical constraints, such as requiring long acquisition times or being costly [40], [59], [60]. Moreover, OCT and RCM are user dependent and have no functional imaging [59], [60]. Also, RCM has a limited detection depth and area of lesions, MI is highly affected by artefacts of movement, and OCT has poor image quality and relatively low resolution, owing to the small field of view of its devices, which implies the need of merging several images to fully examine the lesion [40], [59], [60].

Finally, optical spectroscopy techniques, compared to other non-invasive technologies, have been showing promising performances. These techniques have been based on reflectance, fluorescence and/or Raman scattering [60]. However, they have some issues, regarding *in vivo* tissue applications: FT-Raman [45], [61] has a large integration time (more than 5 min) due to being a multiplexing single-channel technique, which is constraining for *in vivo* applications [22]. Concerning laser-induced Fluorescence

Spectroscopy, or short LIFS, [44] since different fluorophores spectra are broad, consequently, signals will be overlapped leading to difficult intensity quantification [60]. Moreover, due to the problem of autofluorescence of pigmented lesions, FS is suboptimal to diagnose melanoma, so it is not implemented alone, but coupled with other spectroscopic techniques, e.g., Diffuse Reflectance Spectroscopy (DRS) [62] and/or with Raman Spectroscopy (RS), which are known as multimodal devices [63]. Although these devices can collect complementary information about lesions, since they implement different techniques in one device and consequently improve sensitivity and specificity, they also lead to more complex configurations. Also, DRS [46] depends on scatters and absorbers and is less biochemically informative, when compared to RS [60].

Additionally, compared to other non-invasive technologies, optical spectroscopy techniques have high sensitivity and specificity. Indeed, in 2020, Blundo *et al.* [40], compared several diagnostic techniques for melanoma detection in clinical settings, which included: RCM, OCT, MI, DRS, RS, FS, EIS and thermal measurements. In this study, the team concluded that optical spectroscopy techniques had the best sensitivity (93%, 95% Confidence Interval (95% CI) 92.8–93.2%) and specificity 85.2% (95% CI 84.9–85.5%). Moreover, the authors concluded that RCM alone achieved only a sensitivity of 88.2%, (CI 80.3-93.1%) and a specificity of 65.2%, (CI 55-74.2%), but combined with dermoscopy the sensitivity raised to 98% (CI 92-99%) and specificity to 92% (CI 87-96%).

Concluding, considering that some of the available non-invasive *in vivo* diagnostic techniques are subjective, since they are based only on morphological aspects, and/or are not suitable for clinical setting usage, the implementation of a more efficient technique based on chemical and physiological features is needed for biomedical and clinical applications, namely *in vivo* and *ex vivo* diagnosis of (pre)-malignant lesions in various types of tissues, also with a perfect sensitivity and high specificity.RS, being a molecular-specific technology, can be the answer to this request.

2.4. Raman Spectroscopy

Optical Vibrational Spectroscopy: IR *versus* Raman

Vibrational spectroscopy (VS) is a spectroscopic method that measures the vibrational energy in a compound, enabling the identification and analysis of samples in real-

time [64]. The molecular vibrations are specific to the structure of molecules, and therefore, enable the characterization of the spectroscopic identity ("fingerprint") of the analysed material (sample) [23]. Furthermore, VS techniques allow the identification of potential structure alterations, since each vibrational mode contributes to a different spectrum of vibrational energies [23].

Due to their structure, molecules can have different vibrational modes, as seen in Figure 2.4. Molecules can modify the arrangement of atomic bonds by changing the vibrations of bond angles, *i.e.*, bending, and/or changing the bond length, *i.e.*, stretching vibrations [23]. Stretching vibrations can be symmetric or asymmetric, and bending vibrations can be in-plane (rocking and scissoring) and/or out-of-plane (twisting and wagging), as seen in Figure 2.4.

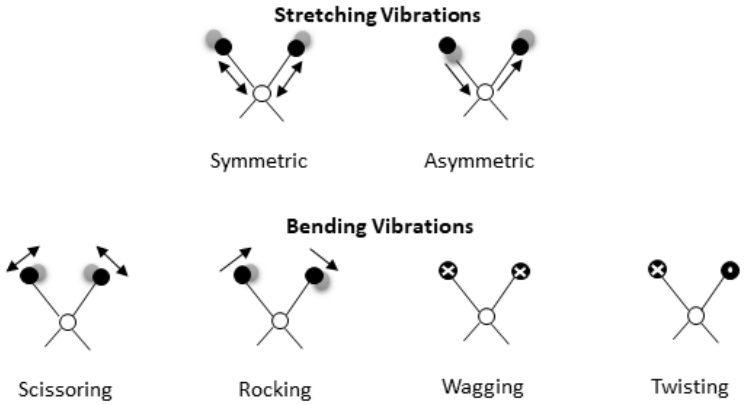

Figure 2.4 – Schematic representation of molecular vibrational modes: stretching (symmetric and asymmetric) and bending in-plane (scissoring, rocking) and out-of-plane (wagging, twisting). The notations used in the wagging and twisting vibrations indicate that the vector is going into (represented by an 'x') or coming out of (represented by a '.') the page, representing the orientation of the molecule's rotation, while the arrows indicate the direction of the movement [23].

There are two types of optical VS: infrared (IR) and Raman. Although the two optical VS techniques are complementary to the identification of molecular structure, Raman and infrared spectroscopies can be distinguished through the process of energy transfer by the photon to the molecule, causing a change in the vibrational state of molecules [64]. Whereas IR Spectroscopy demands a change in the dipole of the molecule, RS implies a change in the molecule polarizability [23].

This dissertation will focus on RS, which is a non-destructive, non-invasive optical technique, widely used to characterize biological tissues through detection of the inelastic molecular changes due to pathological processes [23], [65], [66]. RS has been able

to monitorize substrates, biomass and quantify product parameters in a cost-effective, sensitive, and specific manner, with low or no preparation of samples [64], [66].

Many applications of RS have been proved to be successful, e.g., detection of chemical compounds in airports [67], characterization of samples in the forensic context [68], and quality control in the pharmaceutical industry [69]. More recently, RS was applied to the biomedical and clinical fields, especially in oncology, with higher sensitivity compared to the nowadays diagnostic methods. Some examples for cancer diagnosis RS applications are head and neck [70], breast [71], lung [72], stomach [73] and brain metastases [74]. Other applications of RS in the medical field are Alzheimer's disease diagnosis [75], detection of circulating tumour cells in the blood [76], prevention of allograft rejection in transplanted patients [77] and biomarkers to identify, e.g., bronchial inflammation with asthma [78].

2.4.1. Principle of Raman Scattering

In 1928, the physicist C. V. Raman and his colleague K. S. Krishnan witnessed a phenomenon similar to the Compton scattering light in X-rays, years later named: the *Raman scattered light*, *i.e.*, that a portion of the light scattered in a liquid medium changed in wavelength [79]. This discovery was rewarded in 1930 with a Nobel Prize of Physics, and the optical technique, RS, was named after this rewarded physician.

When light interacts with matter, the incident photon can be absorbed, scattered, and/or pass throughout the material without causing an interaction with surrounding molecules [80]. If the photon is absorbed by the molecule, a light scattering effect occurs, as represented in Figure 2.5.

Light scattering is the effect of the interaction of light with matter, *i.e.*, collisions of light photons with surrounding molecules will polarize the molecule's electron cloud, and raise the vibrational energy of the molecule to a 'virtual energy state' [81], as represented in Figure 2.5 (a). The molecule, after a few picoseconds, can release the energy and drop back to its ‘vibrational ground state’. While releasing the energy, two types of scattering can occur, elastic or inelastic scattering, with a ratio of 10^6 - 10^8 photons to 1 photon, respectively [80], [82], [83].

Hence, the most likely to happen, an elastic scattering - or Rayleigh scattering – is characterized by the returning of the molecule to its original ground state with the emission

of a photon with the same energy as the incident photon, as depicted in Figure 2.5 (a) (in yellow) [80], [82].

An inelastic scattering, - also known as Raman scattering - is a rare phenomenon that takes place when the molecule returns to a different energy state from the original one, with consequent emission of a photon with different energy [82]. The Raman scattering, as seen in Figure 2.5 (a), can be differentiated in:

(i) Stokes shift (in blue), if the molecule is initially in a fundamental state, it absorbs the incident photon's energy, transitioning to a virtual energy state. Then, after the subsequent energy release, the molecule's vibrational state is more energetic than the original state, with consequent photon's energy loss [80], [81], [84].

(ii) anti-Stokes shift (in red), if the molecule, already in an excited state, absorbs the energy of an incident photon, transitioning to a virtual energy level. Then, after releasing the energy, it relaxes to the ground state, and so, the final energy state is lower than the original, with photon's energy gain [80], [81], [84].

The difference between the energy of the incident and emitted photons will be translated into the energy of specific molecular bond types vibrations, or vibrational modes [84]. Each spectral Raman band will occur at a characteristic vibrational frequency that is particular to a specific molecular vibrational mode, as schematically represented in Figure 2.5 (b) [81]. Since energy and frequency are directly related, Raman scattered photons are frequency-shifted when compared with the incident photon frequency, as seen in Figure 2.5 (b) [82]. Furthermore, as illustrated in Figure 2.5 (b), as energy and wavelength are inversely proportional, photons are emitted at a shorter wavelength when they gain energy (Anti-Stokes Scattering), and at longer wavelengths, when they lose energy (Stokes Scattering) [65], [81].

Additionally, the intensity of each single spectral band is directly proportional to the quantity of those vibrations [60]. For that reason, and since the majority of molecules at room temperature are in the fundamental state, the probability of occurrence of Stokes scattering will be higher than anti-Stokes scattering. Therefore, the Stokes signal has a higher intensity than the anti-Stokes shift, as illustrated in Figure 2.5 (b). Hence, the Raman Stokes shift region is the most analysed in biomedical applications. [65], [82], [84].

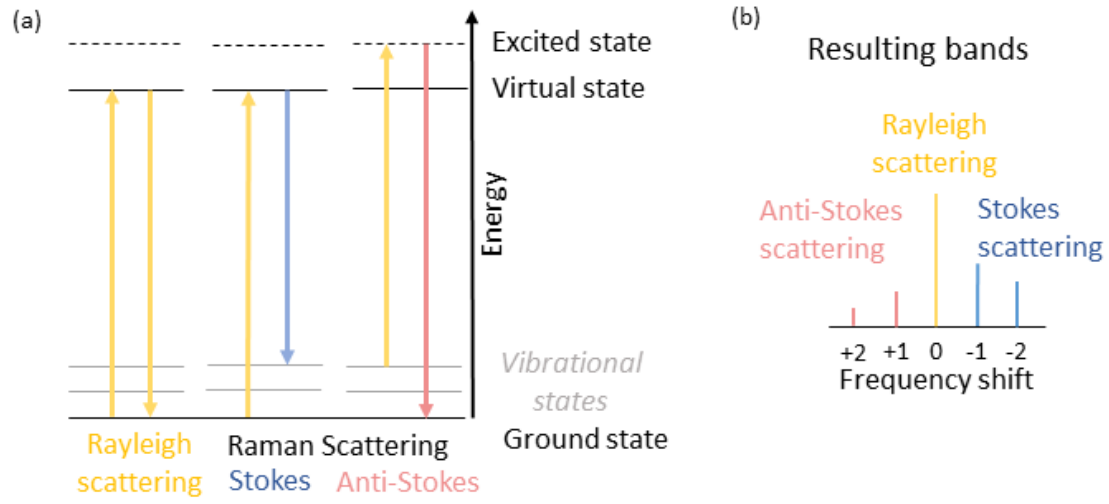

Figure 2.5 – (a) Molecule energy levels diagram of scattered light with the three types of scattering: Rayleigh (yellow), Stokes (blue) and anti-Stokes (red). **(b)** Illustration of the frequency-shifted distribution and the relative intensity of the different scattering bands. Adapted from [84].

A Raman spectrum is expressed in terms of wavenumbers, *i.e.*, a unit of measurement for Raman shift independent of the excitation wavelength used, given as equation 2.1, where, $\tilde{\nu}$, is the Raman shift in wavenumbers (cm^{-1}), λ is the wavelength of the Raman signal in nanometres (nm) and, λ_0 is the laser's excitation wavelength, also in nanometres [60].

$$\tilde{\nu}\,[cm^{-1}] = 10^7 \left(\frac{1}{\lambda_0} - \frac{1}{\lambda}\right)\,[nm] \tag{2.1}$$

In the vast majority of Raman applications, the spectral region detected is the fingerprint region (400 – 1800 cm^{-1}), since it is particularly rich in spectral biochemical signatures associated with nucleic acids, lipids, proteins and carbohydrates [60], [85]. Another spectral region, the high wavenumber region (HWVN), is located between 2500 – 3800 cm^{-1}, and consists mainly of Raman bands associated with CH^-, OH^- and NH-stretching vibrations, of lipids, proteins and water [60], [85].

As previously stated, melanoma lesions, especially MIS, are difficult to distinguish from several types of BML, such as the ones named in Figure 2.6 (a), which have been misdiagnosed by dermatologists as lesions suspected of being melanoma [26].

Concerning a comparison study between melanoma and BML analysing their respective Raman spectral fingerprint region, Feng *et al.* [86], concluded that the two major biomarkers to distinguish these lesions were collagen and triolein. Moreover, they reported that the adjacent tissue of BML had a substantially higher quantity of collagen when compared to the adjacent tissue of melanoma lesions. The authors claimed that this

difference is due to melanoma metastatic propensity that changes the stroma microenvironment, responsible for supporting melanoma metastasis, consequently reducing the quantity of collagen. However, this region of the spectrum has issues concerning tissue autofluorescence that will be addressed further.

In addition, the HWVN region of the Raman spectrum of melanoma and BML also gives important insights to segregate those lesions, as seen in Figure 2.6 (particularly evident in (b)). Santos *et al.* [26] elaborated a study to investigate the differences of the Raman spectra of melanoma and BML suspected of being melanoma in the HWVN region, particularly at the 2820−3040 cm^{-1} range, as seen in Figure 2.6 (b). The authors concluded that melanoma lesions present higher spectral intensities, between 2840 and 2930 cm^{-1}, for instance: at (i) 2854, (ii) 2876, (iii) 2896 cm^{-1} and (iv) a band at 2922−2930 cm^{-1}. The predominant peaks at 2854 cm^{-1} of the melanoma spectrum were assigned to lipids symmetric CH_2 stretching vibrations. Following, the peaks at 2876 cm^{-1} and 2896 cm^{-1} regions were allocated to lipids asymmetric CH_2 stretching vibrations. And finally, the band at 2922−2930 cm^{-1} was appointed with the symmetric CH_3 stretching vibration of proteins and lipids.

Moreover, in the same study [26], the authors reported lower intensity peaks between 2930 and 3000 cm^{-1} in the spectrum of melanomas, when compared with the different types of BML analysed, in particular, a less intense peak at 2950 cm^{-1}, which was appointed to proteins CH_3 stretching vibration.

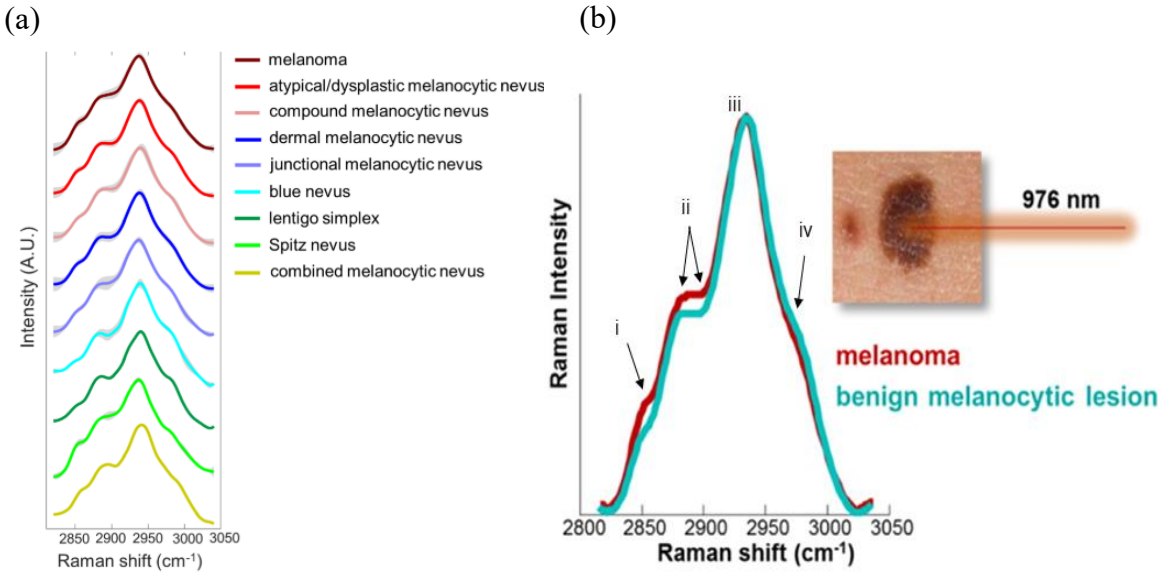

Figure 2.6 – (a) Raman Spectrum in the HWVN region of melanoma and several types of BML, suspected of being melanoma. **(b)** Typical Raman spectrum of melanoma (red) and BML (blue). Adapted from [26].

Concluding, Raman spectral bands in the HWVN can differentiate early melanoma from BML, mostly due to symmetric stretching vibration of CH_2-CH_3, correlated with the higher lipid−protein ratio in melanomas compared to BML. Therefore, making use of a 976 nm excitation laser, this region will be located between 1300 and 1550 nm.

2.4.2. Conventional Raman Spectrometers

Conventional Raman spectrometers are composed of four principal components: (1) a light source; (2) a sampling stage; (3) a spectrograph and a detection system, as seen in Figure 2.7. As is represented in Figure 2.7, the most used geometry in *in vivo* biomedical Raman applications is the 90º configuration, where the light scattered by the sample will be collected on the same optical path of the incident light.

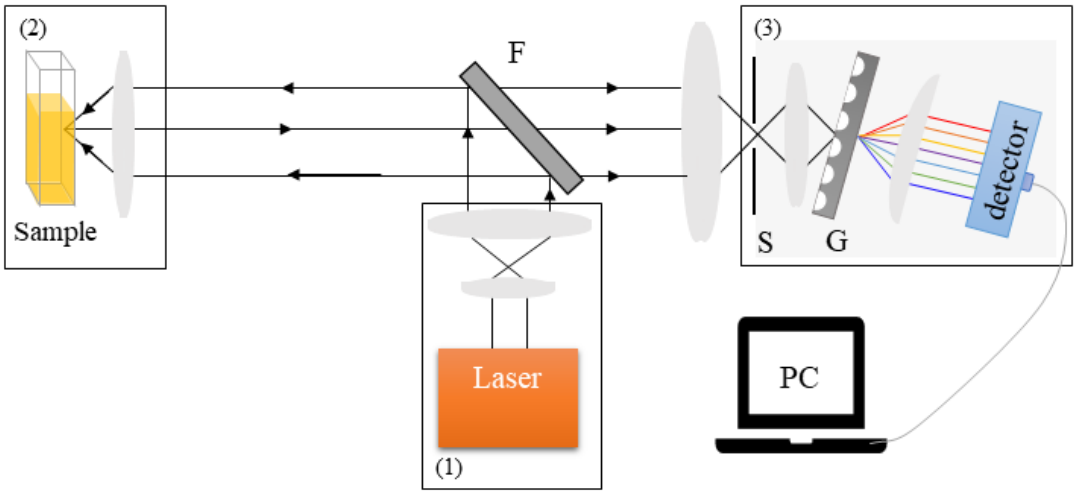

Figure 2.7- Conventional 90º Raman spectrometer configuration. The four major components are: **(1)** light source; **(2)** sample stage; **(3)** the spectrograph and the detector. (F) – filtering element; (S) – entrance slit; (G) – diffraction grating; (PC) – computer.

The light source (1) of a Raman spectrometer is a monochromatic intense radiation, usually a laser due to its properties, which are stability and narrow line and collimated output beam. Then, the light is directed to the sample stage (2) by a set of optical lenses, which are responsible for focusing/collecting the light beam into and onto the sampling stage. A 90º configuration can be much simpler since the backscattered photons will be collected by the same optical lenses that focus the laser light on the sample and direct them to the spectrograph (3). Between the sample stage and the spectrograph, a filtering element (F), such as dichroic filter, edge filters or notch filters, is placed in the optical path to suppress Rayleigh scattered light and select the inelastically scattered photons with

wavelengths above the laser line (Stokes Raman scattering) [65]. Then, after an additional optical lens, the light will be directed onto the first element of the spectrograph. The spectrograph (3) is composed of an aperture element, a dispersive element, and focus/collimate optical lenses. The first element of this unit is the aperture element, an entrance slit (S), which collects the backscattered signals to enter the spectrograph. Next, the dispersive element, a diffraction grating (G), will spatially separate the scattered photons reflected by the sample based on their wavelength [23]. Finally, the Raman bands are collected by the detection system controlled by an external device, such as a computer (PC), which will store and analyse the data acquired.

The spectrograph resolution is dependent on multiple factors: the groove density of the diffraction grating, the wavelengths analysed, and the spectrograph length (distance from the grating to the detector) [23]. Higher resolutions of spectrometers are obtained with higher wavelengths and larger spectrograph lengths [23].

The Raman spectrum can be detected and recorded in two manners: sequentially by a single photomultiplier used with a scanning monochromator; or simultaneously by a multichannel detector, like Charge-Coupled Devices (CCD) or Indium-Gallium-Arsenide (InGaAs) detectors arrays.

2.4.3. Challenges and Solutions of Raman Signal

RS has some limitations to overcome. One of those is the intensity of the Raman scattering being extremely weak compared to the Rayleigh scattering intensity [65]. Therefore, to obtain a good quality Raman signal, the interference of the Rayleigh effect must be eliminated, and a high quantum-efficient detector must be used. Usually, the solution is cutting off the spectral range near to the laser line wavelength, since the majority of stray light is close to the wavelength of the laser [87].

Another limitation of photodetectors used in RS is their inherent thermally generated noise, therefore, with the temperature increment, some Raman lines would become more diffuse or not perceptible [66]. For that reason, some detectors are cooled with liquid nitrogen or with a Peltier.

Additionally, other factors to consider are the periodic calibration and routine maintenance of the equipment [88]. However, this is a general limitation of instruments that can be easily overcome with the establishment of protocols.

Also, fused silica, which is the main element of optical components, such as fibre optics and lenses, used in the instrumentation of RS, has a strong background signal in the fingerprint region [18], [22], [89]. Hence, its signal will overlap with the Raman low-intensity signal. A solution is to detect and analyse the HWVN spectral region because fused silica does not have Raman bands in this spectral range [20], [21], [90].

Regarding biological tissue applications, especially melanin-rich tissue such as melanoma and BML, RS has an added major obstacle, which is laser-induced tissue autofluorescence. Autofluorescence (AF) can be caused by the interaction of light with the epidermis extracellular matrix, especially collagen, elastin and melanin, which absorb light and then reemit it in the 300-700 nm region of the spectrum [91], [92]. Consequently, for visible excitation wavelengths, when the RS laser interacts with highly pigmented biological samples, the induced tissue AF will be located in the fingerprint region of the Raman spectrum, particularly, below 1000 nm [17]–[19]. Since fluorescence can be several orders of magnitude stronger than Raman signal, it will be superimposed to the signal which often compromises the quality of the Raman Spectra [16]–[18]. In order to solve this problem several strategies were implemented and are presented below.

2.4.3.1. Alternatives to Avoid Laser-induced Autofluorescence

Some instrumental and computational methods to reject autofluorescence background in Raman measurements have been developed [16], [19].

Some examples of computational methods to subtract fluorescence background are algorithm-based baseline correction methods – such as polynomial fitting [93], [94], wavelets transform [95], [96], extended multiplicative scatter correction (EMSC) [19], Fourier transform, first and second derivatives or shifted-spectral technique [97], penalized least squares method [98], and Savitzky-Golay-method-based fluorescence subtraction algorithm [99]. Although computational methods, such as polynomial fitting, are the most used in RS biomedical applications due to their simple implementation, they cannot subtract the fluorescence shot noise, only the fluorescence background, which is a limitation.

Another category of fluorescence background removal strategies used in RS is instrumental methods. Instrumental methods can be divided into several categories [16], e.g.,: (i) time-domain methods – such as Kerr gated method [100], [101]; (ii) frequency-domain methods, such as phase-nulling method [102]; surface-enhanced Raman Spectroscopy (SERS) [103]; resonance Raman spectroscopy - such as coherent anti-Stokes

Raman spectroscopy (CARS) [104] or stimulated Raman scattering (SRS) [105]; and (iii) other methods, like photobleaching [106]. However, these methods prove to be inefficient to RS in biomedical applications, as some lead to complex, expensive setups, and/or are not suitable to apply in *in vivo* measurements [22].

A different method type that proved to be very promising regarding autofluorescence background removal is wavelength-domain methods - such as shifted excitation Raman difference spectroscopy (SERDS) [19], [107], [108]. Shift excitation wavelength methods rely on the fact that the fluorescence signal is not spectrally affected by changing the excitation wavelength of the light source, but the Raman signal is shifted spectrally depending on this value [19]. Furthermore, with this method, not only fluorescence, but also ambient light, etaloning, or other non-varying sources of noise can be removed from the region of interest (ROI) of the spectrum [19]. Cordero *et al.* [19] compared SERDS to the EMSC method and found that SERDS is most promising when backgrounds are too complex to estimate. However, this study also reports that SERDS reduces the overall signal-to-noise ratio (SNR).

Therefore, in order to solve the fluorescence problem in pigmented tissues in RS, the best option is to implement an excitation wavelength outside the visible range: below 250 to 300 nm, in the UV region; or above 700 nm, in the near-infrared region (NIR) since in these regions the energy of photons is lower and so, excitation of molecules that induce fluorescence is less probable [18], [22], [89]. Since UV light penetration depth is only some microns and moreover, it may cause DNA or cell irreversible damages, it is not suitable for *in vivo* biological samples application [20], [65], [107]. For that reason, the NIR region is preferred as a light-source wavelength to decrease scattering interference, fluorescence, and photodegradation of the sample [22], [23].

Also, another solution is to detect the HWVN region of the Raman spectrum (2500 – 3800 cm^{-1}) because: (i) fused silica does not have Raman signal in this region, which simplifies the signal filtering needed [90], [109]; and (ii) the intensity of the Raman signal in HWVN is higher than in the fingerprint region [90]. Besides, for this particular application, the HWVN region of the spectrum has proved to successfully differentiate malignant from healthy tissue in the past, particularly in skin pathologies [21], [26];

Additionally, analysing the HWVN region combined with the usage of a NIR laser will deviate this region to even longer wavelengths, less prone to fluorescence, which is a crucial feature to *in vivo* applications, such as the one discussed in this dissertation.

However, the usage of a NIR laser causes a new challenge: CCDs are inefficient for the application due to the fact that the Raman signal is shifted above 1100 nm. Silicon-based CCDs, although having low dark noise, low dark current, and high quantum efficiency in the visible and short-wavelength near-infrared (SWIR) region (from 400 nm to 1000 nm), are not sensitive above 1100 nm [17], [22], [23]. Consequently, InGaAs detectors have been the alternative used in RS, for their high quantum efficiency and extended detection range (up to 2500 nm). Nonetheless, their characteristic high dark and readout noise compromise the detection of weak signals, such as the object of this project, Raman [22]. Nevertheless, these detectors are expensive, should be cooled with liquid nitrogen to reduce noise, and have a higher dark and readout noise, which are orders of magnitude higher compared to CCDs [20]. Thus, SNR can be strongly reduced [20].

Concluding, the solution for biomedical application of RS is analysing the HWVN of the spectrum and using a laser above 700 nm to reduce tissue autofluorescence. Hence, the market is pushing companies to improve InGaAs detectors, by solving their inherent poor noise characteristics (Andor^{Tm}, Anton Paar^{TM}, Horiba^{TM}, B&W Tek^{TM}). Some developments have already been accomplished to overcome the fluorescence problem, the definition of the detector and the low SNR issues, as presented below.

Patil *et al.* [22] used a dispersive spectrometer with an InGaAs array detector combined with a 1064 nm laser to distinguish kidney and liver malignant and healthy tissues. The authors reported a reduction in laser-induced autofluorescence in heavily pigmented tissues while reducing the total integration time to 30s. However, SNR was limited due to the InGaAs detector inherent high noise.

Santos *et al.* [20] were able to solve the fluorescence problems of pigmented skin, due to shifting the laser light above 970 nm and using a high-end InGaAs detector developed by Xenics (Leuven, Belgium), with a lower dark current. These advances have made biomedical applications in the HWVN region possible since the SNR of the spectrometer was enough for the Raman signal to be collected from early melanoma lesions and BML. The sensitivity achieved was 100% for MIS diagnosis, however, the technology cost, the LN_2-cooling system required, and the high acquisition time needed in order to

obtain Raman spectra of skin lesions (less than 1 cm^2), are yet inefficient for use in clinical setting.

2.4.4. RS for Melanoma Diagnosis

Regardless of these limitations, some instruments using this technique have been developed in the past and accomplished good results, proving that RS is a promising technology to diagnose melanoma with high (sometimes perfect) sensitivities and specificities. A perfect sensitivity will mean that all melanoma lesions could be diagnosed with the technology. Moreover, a high specificity will mean that the number of unnecessary surgical resections required by physicians would be minimized since the excisions would be only of malignant lesions.

Most publications are based on RS *ex vivo* approaches, however, analysis based on *in vivo* lesions are needed in order to apply it in clinical settings. Zhang *et al.* [88], in a meta-study, analysed 12 studies[3] regarding the distinction of different skin cancer: basal cell skin cancer; squamous cell skin cancer and melanoma, from normal healthy tissue. They concluded that sensitivity/specificity for melanoma lesions compared to healthy skin was 100/98% (95% CI) for *ex vivo* samples, and, 93/96% (95% CI) for *in vivo* cases, concluding that performance of RS is better in *ex vivo* lesions than *in vivo* lesions. The authors attribute this difference to the limited acquisition time to collect Raman spectra from *in vivo* samples compared to the *ex vivo* studies, which consequently influenced the amount of information extracted from the *in vivo* samples.

Although some studies carried out in the last decade compare melanoma lesions to normal skin, the most crucial analysis is differentiating melanoma lesions from BML since their mischaracterization is a dermatologists' common difficulty [110]. Hence, some *in vivo* and *ex vivo* studies have been developed in order to analyse the accuracy of RS technology to classify these two types of lesions.

Zhao *et al.* [111], in 2008, upgraded a previous developed rapid NIR-RS system [112], using a 785 nm diode laser (300 mW), a homemade Raman probe, and a spectrometer with a CCD array cooled with liquid nitrogen. The spectral resolution was $8cm^{-1}$, spot size 3.5 mm and 40º incident angle and spectral range of 800 to 1800 cm^{-1}. Lui *et al.* [113], in 2012, using this device, reported that they could discriminate *in vivo* samples of melanoma

[3] In which only 3/12 studies were regarding melanoma (1 *in vivo* and 2 *ex vivo*)

(44 lesions) from BML (286 lesions) with a sensitivity of 99% (95% CI: 96-100%) and very low specificity of only 15% (95% CI: 11-19%) with principal component with generalized discriminant analysis (PC-GDA) classification and specificity of 14% (95% CI: 10-18%) with partial least-squares (PLS) classification. A constraint of this study was that not all lesions were biopsied and confirmed by histopathology, as well as the low specific obtained. Also, the "training" and "testing" lesions were the same, so classification could be biased.

Zhao *et al.* [39], in 2015, enlarged the analysis to a bigger dataset of different types of skin cancer lesions and benign skin lesions, (645 lesions from 409 patients, in which 53 lesions were melanomas and 336 were BML). They obtained a sensitivity of 99%, although specificity was only 24% using a PLS classification method. Similar results were obtained with PC-GDA classification. However, although they had used different training and testing groups of lesions, the analysis done was accomplished by comparing cancerous skin lesions *versus* BML, which is reflected in the results: they missed 3 melanoma lesions when the device's sensitivity was 99% and when it decreased to 95%, specificity was 54%, leading to misdiagnose of 7 melanomas as BML. Later, this device was commercialized as a clinical skin cancer RS device, called Verisante Aura™, in Canada, but due to its low specificity, it produces a significant percentage of false positives.

In 2014, Sharma *et al.* [92] improved the multimodal optical spectrometer device (DRS, LIFS, RS) and the multimodal optical fibre probe developed by Motz *et al.* and Rajaram *et al.* years before [47], [114], [115]. A pulsed xenon flash lamp (range 375-700nm) (DRS), a pulsed nitrogen laser (LIFS) and an 830 nm diode laser (56 mW output power controlled by software) (RS) were used for each system. The camera used was a 1024x1024 camera cooled to -30 ºC controlled by software (MATLAB and LabVIEW). The spectral dispersion obtained was 1.79 cm^{-1} per pixel and the spectral resolution was of 13 cm^{-1}. They analysed the fingerprint region of the spectrum.

Lim *et al.* [62], in 2014, using a very narrow dataset (including 12 melanoma lesions and 17 BML), the multimodal spectral approach developed by Sharma *et al.* and a multiple highest varying principal components (PC) analysis, developed a leave-one-out logistic regression classification to distinguish *in vivo* melanoma from nonmelanoma skin lesions, including melanoma *vs.* BML. In this study, they proved that RS alone could differentiate melanoma from BML with perfect sensitivity and specificity (100%). They also reported that the results obtained with the other two modalities integrated into this device,

which are Diffuse Optical Spectroscopy (DOS) and Laser-induced Fluorescence Spectroscopy (LIFS) - although both separately could distinguish the group composed of melanoma and BML lesions from healthy skin, with sensitivities higher than 93% - the two modalities could not differentiate between melanoma and BML lesions leading to sensitivity/specificity of 17/59% for DOS, and 67/18% for LIFS. This suggests that RS is a much more specific technology to distinguish melanoma from BML compared to DOS and LIFS. Moreover, this device has a more complex configuration inherent to the number of modalities used. Additionally, they used a small dataset of melanoma and *nevi* lesions, and the classification was considered positive if any of the DOS, LIFS or RS analysis was positive, which leads to a very high sensitivity when using the combination of the three modalities. However, the specificity could be biased, leading to a large number of false-positive results, such as the case of melanomas *vs.* BML or melanoma and BML *vs.* healthy skin.

Schleusener *et al.* [116], in 2014, built a Raman spectrometer using a 785 nm laser (40 Wm) as a light source, a monochromator and a grating of 600 lines/mm. As a detector, they used a back-illuminated deep depletion CCD cooled to -70 ºC. With this spectrometer, Schleusener *et al.* analysed the fingerprint region (300 - 1700 cm^{-1}) with an acquisition time of 10 s and obtained a spectral resolution of 11 cm^{-1} for a slit of 200 µm. Schleusener *et al.* [117], in 2015, used the fibre probe-based RS built on the prior year to an *in vivo* dataset that included 36 melanoma lesions and 67 BML. They obtained sensitivity and specificity of 87% and 94% for discriminating clinically suspected melanoma (confirmed by histopathological analysis as being melanoma) from BML, 63% and 85% for clinically suspected melanoma (later confirmed by histopathological analysis as being benign) from BML and 52% a 67% for discriminating clinically diagnosed melanoma confirmed as malignant (by histopathology) and clinically diagnosed melanoma confirmed as benign lesions (by histopathology), with partial least squares discriminant analysis (PLS-DA). With a sensitivity so low, this device could lead to misdiagnosing melanoma lesions (false negatives).

Santos *et al.* [15], in 2018, conducted a study based on *ex vivo* RS with a SWIR spectrometer, described previously [20], using 174 freshly excised melanocytic lesions that are suspected of being melanoma. From those, 96 lesions were later diagnosed by histopathologists as BML. In this study, Santos *et al.* proved that thin melanomas, such as

MIS, can be differentiated from benign lesions. They concluded that the multichannel RS instrument technology could improve the diagnosis of melanoma, reducing the number of lesions needed to treat from 6.0 to 2.7 with a sensitivity of 100% and a specificity of 43.8%. This study added also the goal of proving that the equipment was highly efficient regardless of histopathological heterogeneity appearance of the lesions since it was in accordance with a dataset analysed previously by the same author with only homogeneous lesions [26]. However, as referred before, this device is not yet efficient for use in clinical setting.

Khristoforova et.al. [63] built a NIR multimodal spectrometer (RS and AF) using a 785 nm laser module (150 mW), cooled to -15 ºC, an optical Raman probe to collect the data from *in vivo* skin lesions, and a spectrometer with an Andor CCD digital camera cooled down to -65 ºC. They analysed a large spectral area, from 803-914 nm due to the autofluorescence in pigmented tissue: Fluorescence Spectroscopy (FS) (300-1200 cm^{-1}) and RS (1200-1800 cm^{-1}). AF and RS give complementary information, however, due to the large region under analysis, acquisition times were must longer than with a dedicated RS device. Furthermore, the RS independent analysis was more efficient than using AF. Regarding the analysis of a dataset composed of 19 melanoma lesions and 19 BML, using PLS-DA classifiers, the sensitivity/specificity of the device using AF and RS together were 73.7/97.4% but when the two methods were separated, the AF method alone decreased efficiency (68.4/84.2%) and RS alone obtained the best performance with 79.0/ 94.6%, respectively. Also, they compared this analysis with the direct diagnosis of experienced dermatologists and found that the equipment was more efficient since dermatologists' sensitivity to distinguish melanoma from suspicious lesions was higher (89.5%), despite specificity as low as 77.8%. This can be justified by (i) the clinicians were specialists in oncology and (ii) they perform unnecessary resections to lower the number of misdiagnosed cases of melanoma. Hence, compromising the specificity of the diagnose, *i.e.,* a considerable amount of lesions after histopathological diagnosis are confirmed to be benign.

In 2021, Bratchenko *et al.* [118] conducted a larger study of *in vivo* samples using the multimodal device built by the same group. The dataset was composed of 617 lesions from 615 patients, which included 70 melanomas and 283 BML, and other skin malignant and benign lesions. Using only RS (1200-1800 cm^{-1}), only AF (300-1200 cm^{-1}), RS+AF, and full spectral (300-1800 cm^{-1}) analysis to discriminate melanoma and BML they

obtained sensitivities ranging between 90-99% (95% CI) and specificities lower than 30% (1-30% 95% CI), which leads to a large number of false positives cases.

To determine the number of resections of BML avoided when RS technology is used in melanoma diagnosis, Zhang *et al.* [7] elaborated a study, composed of 53 BML and 7 melanomas from 52 patients. The authors concluded that the number of resections done could be reduced from 8.6 (60/7) to 4.1 (29/7) if RS technology was implemented as an add-on tool in the clinical setting. This means that the number of resections done to BML could be reduced by 58.5% without compromising the detection of all the melanoma lesions (100% sensitivity, specificity of 58.5%). Although the dataset was limited, this study shows the potential of the implementation of RS technology in the clinical diagnosis of melanoma. However, further analysis with a bigger dataset will increase the confidence of dermatologists in the technology and, hence, reduce the number of resections prescribed by physicians.

2.5. SWIR Compressive Raman for Measurements on Biological Samples

Compressive *sensing (CS)* is a technique that allows signal reconstruction using a restricted subset of samples. The theory of CS is possible under certain conditions: sparsity and incoherence.

The main application of CS is single-pixel imaging (SPI) [25]. Single-pixel compressive sensing is very interesting for Raman imaging due to: being inexpensive and having short computational reconstruction times, and consequently, enabling real-time applications [24]. Hence, CS has already been applied to RS [119], [120]. Compressive microspectroscopy is based on spectral or spatio-spectral multiplexing, using a spatial light modulator (SLM) such as Digital Micromirror Devices (DMD) operating at 10 kHz [24]. The use of this technique allows for the substitution of the detection system used by DMDs coupled with a single sensor element, improving the SNR, reducing costs, and removing the need for advanced cooling systems.

DMDs are arrays of microscopic mirrors, with electronically programmable control of the reflection direction of each micromirror, which is the pixel unit. Each mirror has a tilt angle of ± 12º, corresponding to each pixel being programmed as “on” and “off”. These amplitude modulators are fast programmable spatial light devices and allow shorter

acquisition times or better spatial resolutions since they only record wavelengths of interest [121]. DMDs have been used in RS instruments to replace CCDs [122], for spatially-offset RS [123] and software configurable multi-slit patterns [124].

Compressive RS uses an SLM detector combined with one or two single-channel detectors. These detectors can be photon counting amplified photodiodes or single-channel photomultiplier tube (PMT) detectors [125]. Scotté *et al.* [126], proved that a DMD/PMT-based compressive Raman system was 10 to 100 times faster in acquiring signals for breast tissue diagnosis applications compared to two conventional instruments, one with a CCD and the other with an electron-multiplying CCD.

Another approach of Compressive RS is using two detectors to record the full spectrum. This approach increases efficiency because it eliminates the waiting time of changing the geometry of the programable mirrors. With this strategy, Rehrauer *et al.* [127] detected all Raman photons in a reduced amount of time per measurement.

Sturm *et al.* [24] built a single-pixel compressive RS device to tackle the problems of the existing compressive spectrometer. Sturm *et al.* focus the light from the dispersive element (grating) into the DMD, using a parabolic mirror. The DMD was able to select the detection wavelengths, and, through the usage of achromatic lenses, the signal was detected by a single-photon avalanche diode.

Applications to skin cancer have been ongoing investigation such as the spectrometer built by Sinjab *et al.* [124], which combined a multifocal instrument (RS and FS) with holographic optical trapping to skin cancer diagnosis, using a liquid-crystal SLM to create a power-shared excitation pattern and DMD to speed collection of the signal.

As seen by the previous applications, it can be concluded that SLM devices, especially DMDs, are very suitable for RS biological applications, since they can reduce the acquisition time, which is crucial in clinical settings applications, such as melanoma diagnosis discussed in this project.

Concluding, the main future goal of this project is to develop a low tolerance compressed Raman spectrometer. Therefore, the detection system will be replaced by a compressive element - DMD – combined with a single element detector – InGaAs photodiode. This compressive configuration will (i) provide a much faster acquisition time, due to the subsampling of the dataset, *i.e.*, only the specific Raman wavenumbers of interest,

from 2820−3040 cm^{-1} range, will be acquired; and (ii) problems of background noise will be reduced with consequent higher SNR and no cooling system needed.

3. MATERIALS AND METHODS

In this chapter, the instrument requirements are presented, in 3.1. Then, the mechanical and optical parts used in the prototype's instrument assembly will be presented and described, in 3.2 and 3.3, where the designed mechanical 3D parts developed for low tolerance alignment are also presented. Afterwards, in 3.4, the methods and mathematical approaches that were followed towards the execution of this project are described. Lastly, in 3.5, three alignment protocols, which must be followed to replicate the alignment obtained in this project and, then in 3.6, the calibration protocols are discussed.

3.1. Instrument Requirements

Currently, melanoma diagnosis and its adequate treatment have two major application needs: (i) a biopsy guidance diagnostic tool for early-detection of MIS lesions and (ii) a surgical margins assessment tool to be used intraoperatively to identify positive margins. In this dissertation, a Raman spectrometer operating in the HWVN spectral region, for future use in MIS detection was developed, in order to accomplish goal (i).

The envisaged Raman spectrometer must answer different requirements related directly to its application needs, *i.e.*, to diagnose early-stage melanoma lesions, as well as claims that must be satisfied so the Raman instrument achieves practical usability, as described below.

(1) **Objective:** based on biochemical composition of tissue.

(2) **Real-time tool**: enables *in vivo* measurements and real-time analysis, providing extra biochemical information to the clinician in the clinical setting and potentially decreasing the number of unnecessary excisions.

(3) **Non-invasive:** able to acquire Raman measurements directly on patients without tissue excision.

(4) **Detection depth of 300 µm:** Melanoma is desirably diagnosed at an early-stage, while the lesion is still not invasive, not metastasized, (MIS). MIS, as referred before, can be surgically removed with a good prognosis. This is translated by a Breslow thickness of less than 300 µm (vertical growth of lesions).

(5) **Accuracy classification model:** A high sensitivity model will enable all lesions to be detected at an early-stage and so, reduce the incidence of invasive cases. Moreover, a high specificity will allow to lower the number of lesions that need treatment, *i.e.*, reduce the number of unnecessary excisions.

(6) **Device spectral resolution lower than 5 nm:** A low spectral resolution is mandatory to identify the biochemical features of melanoma.

(7) **Laser excitation wavelength in the NIR and analysing the HWVN spectral region**: This will significantly reduce laser-induced tissue autofluorescence, as well as Raman signal from optical components (fused silica).

(8) **Laser radiation dose lower than the MPE value,** according to European health, safety, and environmental protection standards for safe laser skin irradiation. The Maximum Permissible Exposure (MPE) is dependent on the laser used and the time of acquisitions.

(9) **Detector range between 1300 to 1550 nm with high quantum efficiency and low noise:** Raman signal is weak and so, detectors must have low noise characteristics in this spectral range to not hinder Raman signal detection.

(10) **Laser linewidth (<1 cm^{-1}):** To enable high spectral resolution, the laser should be characterized by a narrow and highly stable laser line.

As additional requirements, some claims should be satisfied so that these devices can be ideally translated into a clinical setting. These requirements are:

(1) No need for a liquid nitrogen cooling system.

(2) User-friendly – minimal disruption of the clinical workflow, minimal operator training needed, and result provided by simple metrics.

(3) Should be hand-held, portable and enable Raman measurements on difficult targeting body areas, such as ears.

(4) Reduced instrument development cost.

3.2. Optical Instrument Design

The design and establishment of the instrument general optical configuration are presented in Figure 3.1. The transmission, or 0º, configuration spectrometer was designed as a first step for the fulfilment of the project goals. The Raman spectrometer assembly is composed of three parts: the **excitation branch**, from the laser to the sample, the **transmission branch**, from sample to the entrance slit and, finally, the **spectrograph**, from the entrance slit to the detector.

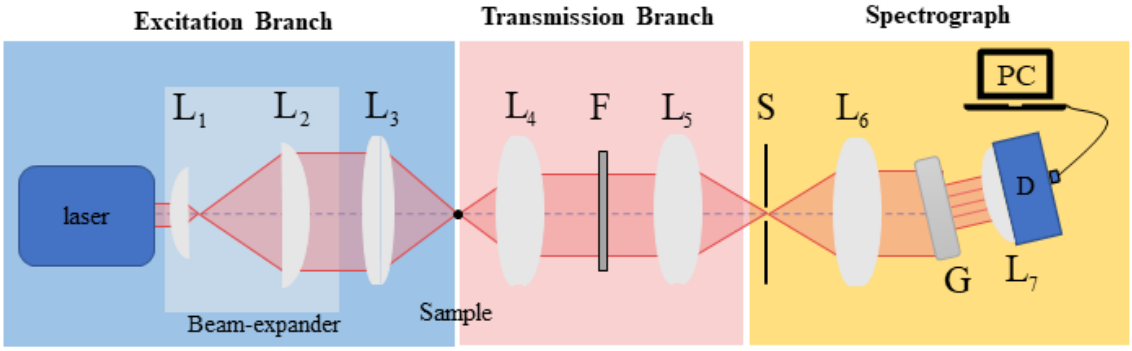

Figure 3.1 - Optical Path of the Raman spectrometer setup. Beam-expander: lens 1 (L_1) + lens 2 (L_2); lens 3 (L_3); sample; lens 4 (L_4); dichroic filter (F); lens 5 (L_5); entrance slit (S); lens 6 (L_6); transmission grating (G); Detector (D) and focal system lens (L_7) and host computer (PC).

Excitation branch: The laser's beam was expanded by two plano-convex lenses (L_1 and L_2), which compose a Keplerian beam expander, as seen in Figure 3.1. Afterwards, an achromatic lens (L_3) was used to focus the light into the sample. The sample is placed in a sample holder (named Universal Sample Cage -USC- system**)**, presented in subsection 3.3.1, which was specially designed to fit different sample's formats and alignment elements (such as lamps, alignment disk, optical fibre and other adapters).

Transmission Branch: After the sample, an achromatic lens (L_4) is used to collect the scattered light and to collimate it. Then, a dichroic filter (F) is used to reject the Rayleigh light. After the filter, a similar achromatic lens ($L_4 = L_5$) collects and focuses the light onto the entrance slit.

Spectrograph: The spectrograph is composed of the entrance slit (S), an achromatic lens (L_6), the transmission grating (G) and the detection system (in this case, imaging sensor + L_7) with the computer acquisition system (PC). The light that is collected by the slit is then collimated by an achromatic lens ($L_5 = L_6$), which is responsible for directing it to the transmission grating. Then, the detector system: a two-dimensional photodetector with a lens is placed to collect the signal of interest.

3.3. Setup Components Description

Table 2 details the components used in the assembly of the built-in Raman spectrometer, from now on called prototype. Also, in the next subsections, materials will be described in detail.

Table 2 –Components used in the prototype setup

Component		Description	Part Number
Lasers	IR laser	Single-mode continuous-wave diode laser with a 976 nm.Output power of 450 mW, TEM_{00} beam profile (M^2=1).	IPS I0976SR0450B
	Red laser 632.8 nm	Helium-neon gas laser. Excitation wavelength of 632.8 nm. Output power 4mW. Beam quality (M^2) is 1.	JDS Uniphase 1507 Number: 1309810
	Red laser 640 nm	Excitation wavelength 640 nm. Output power 40 mW. M^2 <1.5	Coherent PN:1264218
Optical Lenses	L_1	Plano-Convex Lens. Diameter 5.0 mm. Focal length 5.0 mm	EO67453
	L_2	Plano-Convex Lens. Diameter of 25.0mm. Focal length 150.0 mm.	EO67552
	L_3	Achromatic Lens. Diameter of 25.0 mm. Focal length 150.0 mm	EO45804
	L_4, L_5, L_6	Achromatic Lens. Diameter of 25.0 mm. Focal length 35.0 mm	EO45800
Optical Slit (S)		Slit size 20±2 µm	S20RD
Transmission Grating (G)		NIR Transmission Grating, 300 Grooves/mm, 31.7° Groove Angle. Size 25 mm x 25 mm	Thorlabs GTI25-03A
Detector sensor (D)		CMOS Camera (1024x1280 pixels). Monochromatic. Resolution 1.3 M pixels. Pixel size of 6.7 µm x 6.7 µm	Pixelink PL-B741EU
Detector lens (L_7)		Fixed Focal Length Lens. Focal length 50 mm.	EO59873 (R500045524-13038)
Linear Polarizers		Rotating linear polarizer	PRO32-30.5
Filters	769/41 nm filter	Bandpass filter. Central wavelength 769nm. Bandwidth of 41 nm, with OD> 6 Blocking	EO84105
	750/50 nm filter	Bandpass filter. Central wavelength 750nm. Bandwidth of 50 nm, with OD > 4 Blocking	EO84788
	980 nm filter	RazorEdge ultrasteep long-pass edge filter of 980 nm. OD > 6	Semrock LP02-980RE-25

In this project, different lasers, IR and red, were used. The main laser, IR laser, used in this project (Innovative Photonic Solutions I0976SR0450B) provides a circularized and collimated Gaussian profile with a diameter of 0.6 mm and a low divergence angle (2 mrad). However, the detection system available to use at the time of the elaboration of the project had a limited detection above 1100 nm, which made this laser not suitable to the main goal which is Raman measurements in the HWVN region of the spectrum, which will be above 1300 nm. Thus, two different red lasers were used as light sources in order to develop the spectrometer, since their HWVN region, according to equation 2.1, will be just above 700 nm. The first red laser, (JDS Uniphase) had a diameter of 0.48 mm and a divergence of 1.7 mrad. This laser's base integrates a 1''-32 threaded bezel which was used to create a post system, presented in Appendix A. Finally, a second red laser was used (Bioray Coherent laser diode) with an elliptical dot beam output with adjustable focus with a divergence of <3mrad. This laser power was adjustable and controlled by an external voltage source from 0.5V to -5V.

To focus and collimate the light beam, several lenses, plano-convex or achromatic, were used throughout the assembly. In the excitation branch, two plano-convex lenses L_1 and L_2 were used to build a Keplerian beam-expander. Their asymmetric surfaces minimize spherical aberration when the light is not irradiated at the same distance of the lenses, such as an optical beam.

In the transmission branch and spectrograph, achromatic lenses (L_3, L_4, L_5 and L_6) were used. These lenses are designed to correct the spherical aberration for polychromatic imaging applications, enabling focusing light rays of different wavelengths at the same point. Therefore, they are ideal for imaging applications, such as focusing and expanding NIR lasers' beams and focusing/collimating beams for fibre optics. Thus, before the sample, L_3 was used since achromatic lenses also enable the smallest spot sizes possible and, after it, L_4, L_5 and L_6 were used since the sample emits polychromatic light and so they allow to focus the polychromatic beam into the entrance slit.

Also, all the lenses are NIR-II Coated (wavelength in the 750-1550 nm range), which means that the reflectivity is less than 1.5% for wavelengths between this range, improving the transmission of light in the ROI of the spectrum, minimizing light loss.

In this dissertation, three different filters were used in the calibration of the prototype spectrum: two bandpass filters from Edmund Optics™ and a high-pass from

Semrock™. The 769/41 nm filter has a transmission of the signal superior to 93% and is hard sputtered coated on a single fused silica substrate with less than 3% from the edge of bandwidth. The 750/50 nm filter has also a high transmission (minimum of 90%) and is a deep blocking bandpass filter with broad bandwidths. The LP02-980RE-25 (986 nm filter) is a razor edge ultrasteep long-pass filter with an Optical Density (OD) > 6 and high transmission of more than 93% between 986.4 and 2000 nm. The sharp edges of the filters used were particularly important to the calibration done using the halogen lamp. Also, since RS applications require blocking the excitation wavelength of the lasers used, as well as stray light background noise, these filters' inherent high and steady OD makes them very efficient in eliminating unwanted background noise.

After the calibration, the 980 nm filter was used to discard laser light and select only the Stokes shift region of the Raman signal after the sample, while using the main laser (976 nm). Although this filter has a high OD and sharp edges at an angle of incidence of 0º, the same is not verified at an angle of 45º, where the cut-off edge wavelength drops to 926nm, not rejecting the laser beam. Consequently, the setup assembled has a transmission configuration, which is not suitable for *in vivo* biomedical applications. So, a new high edge filter with the same high-performance characteristics, but with a higher cut-off wavelength when place under 45° should be purchased. However, all the other components are suitable for the application and so the testing of the sensitivity of the prototype and calibration protocols are still valid.

The spectrograph was composed of an optical slit, a collimating lens, and a transmission grating. The used slit has a width of 20 ± 2 µm and a length of 3 mm. The grating used was a 25 mm^2 squared NIR-transmission grating of 300 grooves/mm and with a groove angle of 31.7º.

The used detection system was an imaging camera from Pixelink™ coupled with a lens of 50 mm focal length optic system, with low chromatic aberration. The imaging sensor is a 1.3-Megapixel monochromatic Complementary Metal Oxide Semiconductor (CMOS) with improved performance for the NIR region (from 750 nm to 1 µm). The camera provides video and image mode. A manufacture Application Programming Interface (API) or other (in this case MATLAB) can be interfaced with the imaging sensor and with a host computer by a standard USB of 2.0, to image camera features and save the acquired data.

The most important features that can be manipulated are ROI, gain, gamma, brightness, exposure time (manual and auto mode), number of frames and frame rate.

MATLAB R2020b software was used to interface with the detection system as well as to process data, and then, provide interpretable information to analyse.

Several camera features and capabilities can be controlled by software. To do so, the MATLAB *Image Processing Toolbox* was used, which allows to interface and control camera settings, as well as saving data (captures in .jpg and video in .avi format) to further process.

Data processing enables the acquired data to be transformed into readable information, which is easier to interpret by the user. Hence, data processing was done using MATLAB to convert the images snapshots into spectra. Furthermore, the real-time data processing implemented using this software was a very interesting feature to improve the calibration of the setup.

3.3.1. Universal Sample Cage (USC) System

The prototype was developed with the purpose of allowing low tolerance to components' position variations. Undertaking this movement variation is of extreme importance in Raman application since these signals are of low intensity, and changes in the alignment of the optical components may induce background noise, which can be superimposed to Raman signals, or loss of collected signal altogether. Thus, only an aligned, stable and with low tolerance assembly will achieve high-quality signals and replicate them over time.

With the purpose of making a low tolerance mechanical assembly, several mechanical parts were developed, such as a sample holder and also other mechanical parts, as depicted in Appendix A (*e.g.*, laser and lamp supports, and a detector position fixation system, DFS). All the 3D objects were designed in *Autodesk Inventor Professional 2021* software and edited in the *Ultimaker Cura 4.8.0* software, associated with the *3D printer Ultimaker 2+*, where they were printed in Polylactic acid (PLA) material.

A versatile sample holder was necessary to be able to exchange samples with different formats, for alignment calibration and analysis, without the need for replacing mechanical components in the setup. This would allow to maintain the optical alignment and

consequently, achieve quality and well-defined signal spectra, *i.e.*, with good resolution. Therefore, the Universal Sample Cage, or short USC, (Figure 3.2 – grey part) was designed.

The USC is a mechanical sample holder of 47x47x14 mm^3 with a centric hole of Ø 30 mm and an additional square top entrance of 13.5 mm^2, and it was created to adapt different types of components in the sample position, such as:

(i) An alignment disk placed in a Ø 30 mm mount (EO 85678);

(ii) An optical fibre coupled with an FC connector;

(iii) A mercury lamp (Hg lamp);

(iv) A cuvette for liquid samples.

In addition, a bottom thread of 6 mm was included to allow the USC system to be fixed in an optical table with a post/post holder system. Also, four parallel holes of 6 mm were added for coupling the cage system rods. Furthermore, one thread of 4 mm in each diagonal connects the vertices of the printed cage to the rods and secure its position to minimize oscillation of the cage.

3.3.1.1. Fibre Optic Adapter

When the IR laser is used, it is not possible to see the light beam with the naked eye. Therefore, it makes the alignment of the optical components of the prototype very difficult to execute after the sample. Thus, an Optical Fibre System (OFS) composed of a fibre optic coupled with a red laser (described in Appendix C) was used to simulate the light emitted by the sample after excitation, in a visible way, facilitating the alignment of the optical components from the transmission branch and the spectrometer.

Both endings of the fibre used have FC/CT connectors, which are additionally connected to a metallic Ø 11 mm adapter. However, adapters from the metallic part (Ø11mm) to the USC dimensions were needed to place the optical fibre in the centre of the cage and obtain a perfect alignment of the systems' centres. Hence, a cylindrical adapter from Ø 11 mm (internal diameter) to Ø 30 mm (external diameter) was created to connect the fibre's metallic adapter to the USC system, as seen in Figure 3.2.

Similarly, another cylindrical adapter was also imprinted, with internal and external diameters of Ø 11 mm and Ø 24.5 mm, respectively, where the other ending of the fibre is attached to the cage of the OFS with the red laser (presented in Appendix C).

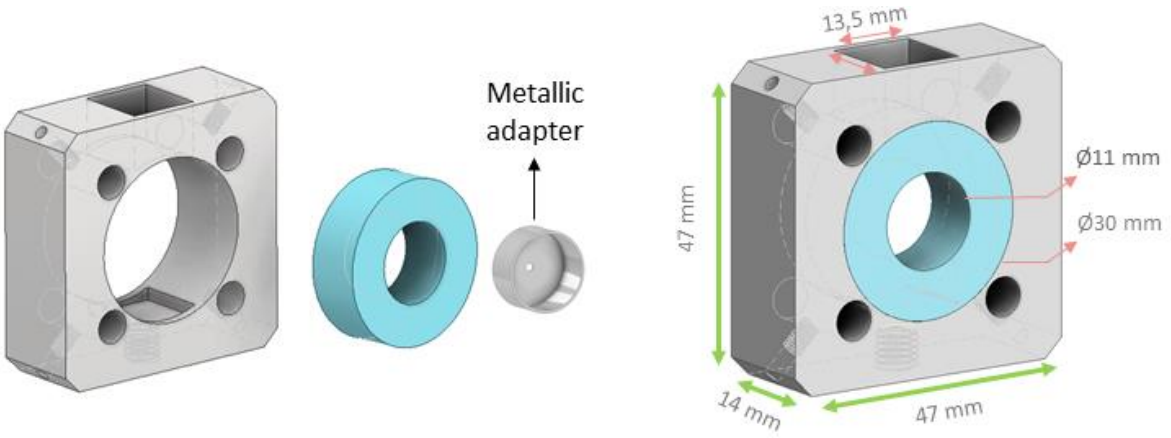

Figure 3.2 - Adapter for the use of an optical fibre (blue object), inserted in the USC part (grey). The metallic part which couples with the FC/PC connector of the fibre is also represented.

3.3.1.2. Mercury Lamp Adapter

A mercury lamp was used to simulate a light sample in the process of calibration of the prototype. Therefore, an additional part to place the mercury lamp in a fixed position during data acquisition was also designed. To do so, a parallelepiped of 13.5x13.5x40 mm^3, with a hole to allow the emitted light of the Hg lamp to pass (blue object in Figure 3.3) was drawn. The lamp (also represented in Figure 3.3) was inserted throughout the upper squared hole of the adapter and an additional bottom cavity stabilizes the lamp, to extra support.

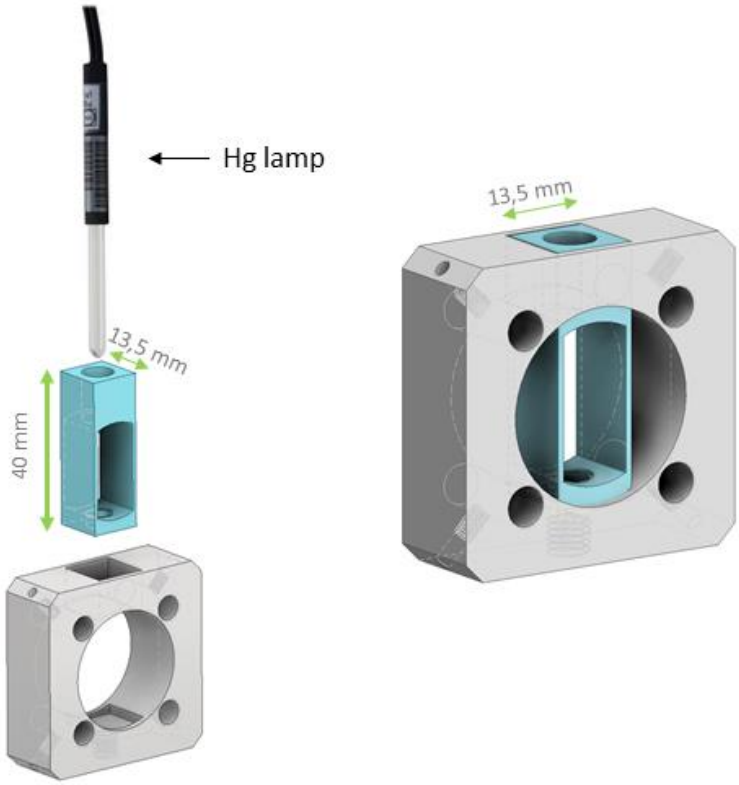

Figure 3.3 - A Hg lamp can be inserted vertically inside the lamp mount (in blue), which can be inserted inside the USC part (in grey).

3.4. Optical System Analysis

Paraxial Optics methods were used to estimate the sample excitation spot size. In this manner, it was possible to verify whether the predefined requirements were fulfilled by the chosen optical components.

3.4.1. Excitation Branch

In the excitation branch, the output beam of the laser is maximized by a Keplerian beam expander (Figure 3.4) composed of two lenses, L_1 and L_2. The distance between them equals the sum of their back focal lengths, $F=f_1+f_2=151.7$ mm. L_1 is made of N-LASSF44 substrate (n_1), has a curvature radius of 4.02 mm (R_1) and 1.87 mm thickness (d_1) while L_2 is made of N-BK7 substrate (n_2), has a curvature radius of -77.55 mm (R_4) and 3.5 mm thickness (d_2).

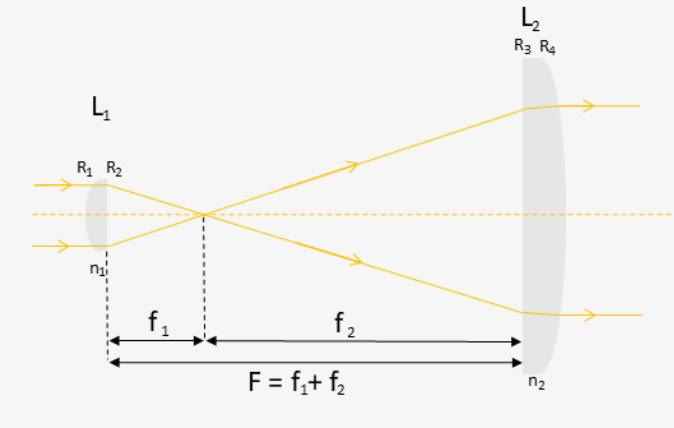

Figure 3.4 – Keplerian Beam Expander

In order to calculate the dimensions of the expanded beam, the matrixial method of paraxial optics was used. The transmitted light ray, r_1, immediately outside the second lens, L_2, can be calculated based on the transformation of the incident light ray, r_0, given by equation 3.1. This equation is the mathematical computation of the beam expander's system matrix, A_{BE}, and the transfer-matrix T_{01}.

The transfer-matrix T_{01} describes the transmission of the laser's beam ray into the first lens, L_1, where the two components are separated by 5 mm, d_{01}.

The beam expander system matrix, A_{BE}, is given by $A_{lens2}\, T_{lens2-lens1} A_{lens1}$, in which (i) A_{lens1} and A_{lens2} are the system matrix of lens L_1 and L_2, respectively - which describes the transformation of the ray light that passes through each lens - and (ii)

$T_{lens2-lens1}$ is the transfer matrix that describes the transmission of light after L_1 and before entering in L_2, separated by the distance $d_{21} = 151.77\ mm$.

The divergence angle of lasers, α_o, was approximated to zero, due to two reasons: (i) the laser beam is collimated, stable and with a low divergence angle (less than 2mrad) and (ii) the laser and L_1 are separated by a short distance (~5 mm). Also, after being expanded, the beam will continue to be collimated. Therefore, the beam dimensions will be constant from immediately after L_2, not being relevant to the transmission from the beam expander to the air.

$$r_I \equiv \mathrm{A}_{BE} T_{01} r_o \Leftrightarrow \begin{bmatrix} n_i \cdot \alpha_I \\ y_I \end{bmatrix} = \mathrm{A}_{lens2}\, T_{lens2-lens1} \mathrm{A}_{lens1} T_{01} \begin{bmatrix} n_o \cdot \alpha_o \\ y_o \end{bmatrix} \tag{3.1}$$

Where,

- α_o and α_I are the divergence angle of the incident light (object) and transmitted rays (image), respectively. α_o, is approximately zero since the laser light is collimated.
- $y_o$and y_I are the height of the object and image, respectively (y_o is half the laser's output beam diameter (d), and y_I is half of the beam expanded height).
- material's refraction index, n, in which the exterior medium is air, $n_i = n_o = 1$.
- T_{01} is the transfer-matrix between the laser and L_1, which are separated approximately by 5 mm distance, d_{01}.

Using equation 3.2, with the respective values of curvature radii in which the light travels and the distance between the dioptrics, we can obtain a general system matrix, in which the refraction index values and the dimensions of the beam are dependent incognitos, subject of the laser used. And so, the final expression to compute the height of the light ray outside the beam expander system, y_I, is given by equation 3.2:

$$\begin{bmatrix} \alpha_I \\ y_I \end{bmatrix} = \mathcal{R}_4 T_{43}\, T_{len2-len1} T_{21} \mathcal{R}_1 \cdot T_{01} \begin{bmatrix} 0 \\ d/2 \end{bmatrix} \Leftrightarrow$$

$$\begin{bmatrix} \alpha_I \\ y_I \end{bmatrix} = \begin{bmatrix} 1 & \dfrac{-(1-n_2)}{\mathrm{R}_4} \\ 0 & 1 \end{bmatrix} \begin{bmatrix} 1 & 0 \\ d_2/n_2 & 1 \end{bmatrix} \begin{bmatrix} 1 & 0 \\ d_{21} & 1 \end{bmatrix} \begin{bmatrix} 1 & 0 \\ d_1/n_1 & 1 \end{bmatrix} \cdot \tag{3.2}$$

$$\begin{bmatrix} 1 & \dfrac{-(n_1-1)}{\mathrm{R}_1} \\ 0 & 1 \end{bmatrix} \begin{bmatrix} 1 & 0 \\ d_{01} & 1 \end{bmatrix} \begin{bmatrix} 0 \\ \dfrac{d}{2} \end{bmatrix}$$

Then, L_3, with a focal length of 35.00 mm, was used to focus the expanded beam on the sample. Finally, the sample spot diameter can be calculated with equation 3.3. It is dependent on the excitation laser wavelength, λ, and the beam quality parameter M^2 (which

is 1 for a perfect Gaussian shape beam), the characteristic focal length of the focus lens (L_3) and the previously calculated beam expanded diameter, $D=2*y_I$.

$$spotsize = \frac{M^2 * 4 * \lambda}{\pi} * \frac{f}{D} \tag{3.3}$$

In this dissertation different lasers were used as excitation sources: an IR laser of 976 nm, which is the one that will be used for melanoma applications in the HWVN, in which ROI will be above 1300 nm; and red lasers, to test the prototype in HWVN (which will be around 700-800 nm), since the detection system available was not sensitive above 1100 nm. Changing lasers would mean that the dimensions of the beam, d, the wavelength of the incident light, λ, and therefore the materials' indexes of refraction, n, would be distinct. Consequently, beam expanded dimensions, D and sample spot size values too. The results for the IR laser and one of the red lasers (632.8 nm) are presented below in Table 3.

Table 3 – Paraxial optics results.

Laser wavelength (λ) (nm)	976	632.8
Laser beam diameter (d) (mm)	0.6	0.48
Index of refraction (n)	n_1= 1.79 [4] n_2= 1.51 [4]	n_1=1.80 n_2= 1.52
Dimensions of the expanded beam (D) (mm)	17.59	14.35
Spot size (µm)	4.2	3.4

3.4.2. Diffraction Grating

The transmission grating is the dispersive element of the spectrograph that is responsible for separating the polychromatic light into its different wavelength lines, which are characteristic of the elements.

When an incident light ray of wavelength λ, with an angle of incidence, θ_i, to the normal plane of a grating, which is characterized by a spatial period between grooves, a, the light is transmitted, in the order of principal maxima, m, with a deflection angle, θ_m, (related to the surface normal) given by equation 3.4,

$$a[\sin\theta_m - \sin\theta_i] = -m\lambda \tag{3.4}$$

[4] Datasheets' closest value to the 976 nm was n (1014 nm)

The dispersion is repeated in the consecutive diffraction orders, m. The grating used in the prototype has a characteristic spatial period of $a = \frac{1}{300}\ mm$ while the detector was placed in the first order of diffraction, m=1, as seen in Figure 3.5. Assuming that the ray light incident angle is θ_i=0 rad and using equation 3.4, the angle, θ_m, for each of the limit wavelengths that get through the detector, λ_1 and λ_2, will be:

$$\lambda_1 = 1300\ nm\ , \theta_1 = \ 22.95°$$
$$\lambda_2 = 1550\ nm\ , \theta_2 = 27.71°$$

The wavelength range used is the spectral ROI for melanoma detection using the main laser of this project (IR laser), *i.e.*, [1300 – 1550] nm.

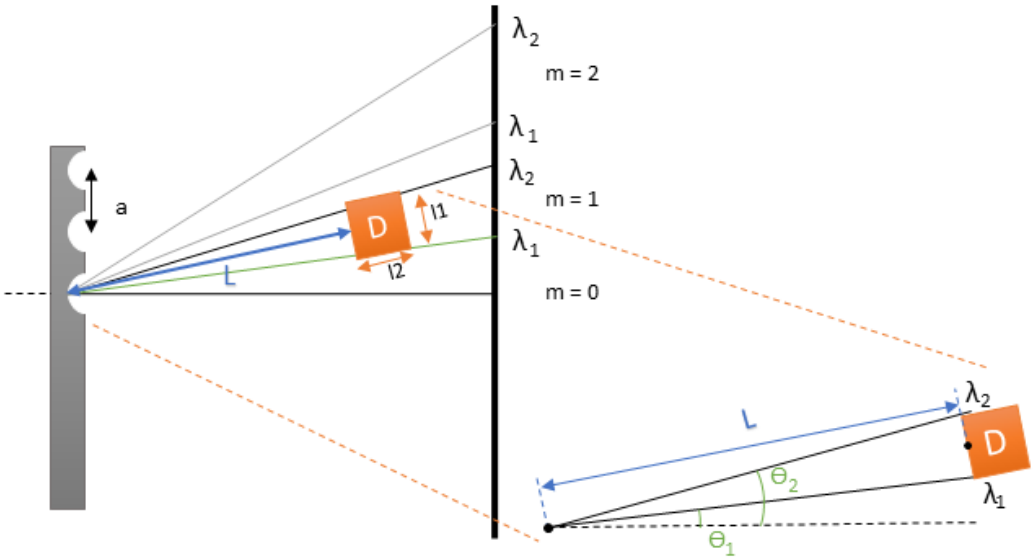

Figure 3.5 – Diffraction grating with a characteristic distance between the grating grooves, a, (at left), with the detector system (D) of dimensions l_1 x l_2 mm^2, distanced by the length, L. In the inset figure, it is shown the detector system with wavelength limits, λ_1 and λ_2, which corresponds to transmission angles of Θ_1 and Θ_2, respectively.

Keeping in mind the main objective of this project, which is building a compressive Raman spectrometer, a detector with dimensions 14.5 x 8.2 mm^2 and pixel size of 7.56 µm (Texas Instruments DPL6500) was considered. Applying trigonometric functions, it is possible to calculate the necessary distance between the grating and the detector, L, to ensure that the wavelength range of interest covers the detector active area, as seen in equation 3.5.

$$L = \frac{l_1/2}{\sin\frac{\theta_2 - \theta_1}{2}} = \ 174.6\ \text{mm} \tag{3.5}$$

Spectrometer's resolution is the capability of separating bands of different wavelengths. It can be calculated theoretically by the product between the number of pixels in the detection system and the slit width, in microns, divided by the pixel dimensions and the bandpass wavelengths, as depicted in equation 3.6 [128]:

$$Resolution = dispersion\ per\ pixel\ \times pixel\ slit\ projection = \frac{\Delta\lambda}{N.pixels} \times \frac{slit\ width}{pixel\ width} \tag{3.6}$$

In this case, the resolution will be 0.34 nm. Using a slit width of 20 µm, the number of pixels is 1920 with pixel length of 7.56 µm, and the bandpass wavelength is 250nm (1300 to 1550 nm).

However, this theoretical calculation of the resolution assumes that the ray light incident into the detector is perfectly aligned with the detector pixels, *i.e.*, perpendicular to the pixels' surface, which is difficult to attain. Nevertheless, the experimental determination of the spectrometer resolution is achieved by determining the Full Width at Half-Maximum (FWHM) of a reference signal.

3.5. Alignment Protocols

The alignment protocols developed for this setup were divided into three distinct parts. The first refers to the alignment of the **excitation branch**, from the laser to the sample. The second concerns the placement of the **transmission branch**, from the sample to the entrance slit. And, finally, the last refers to the **spectrograph**, from the entrance slit to the detector. The separation of these three branches was done to better settle and align the optical components since their positioning is crucial to the success of the output signal.

The optical components of the prototype (L_1, L_2, L_3, L_4, L_5, L_6) were mounted in rigid metal cages with connecting rods to keep them aligned in x and y directions. Additionally, excluding the excitation branch, all post holders were connected to BE1 Thorlabs Adapter rings and CF175 Thorlabs table clamping fork for extra lateral movement of the system.

Furthermore, the prototype was covered with a light shield (black card box revested with rugous textile) to minimize the collection of room light.

To facilitate the alignment and minimize power losses, a power meter system developed and presented in Appendix B was used to measure the laser power. Also, an

Optical Fibre System (OFS) was assembled and is described in Appendix C, to assist the alignment procedure.

3.5.1. Excitation Branch

Step 1.1: Assemble a system of two posts/post holders and Ø 30 mm cages connected by rods. The cages support must be distanced by 130 cm. Then, insert an alignment disk in the first cage, in order to act as a target (the alignment disk has a perforation at its mechanical centre). Add a third cage with an alignment disk at a distance of at least 2 meters. This system will be used to verify the alignment of the output beam laser.

- *Additional cages with alignment disks can be added between the system (connected by rods) to assist the alignment by moving these cages along the rods.*

Step 1.2: Collimation of the output laser beam

First, place the cages at the height of the laser beam output. If necessary, adjust the laser output angle, for the light beam to be perpendicular to the optical table. To do so, use Kapton sheets with 0.1 mm thickness.

Next, connect the laser beam and align it with the centre of the first target. Then, remove the first target and align the laser beam with the centre of the second target. Finally, reposition the first target and check if the alignment is correct. Afterwards, fix the laser to the optical table using table clamping forks. This process should be iterative until necessary.

- *It is expected that the final beam has a constant diameter and fixed height throughout the optical system.*
- *The additional cages immediately after the first two cages should be removed, however, the cage distance of 2 meters should be kept in order to use in the rest of the alignment.*

Step 1.3: Beam expander alignment

Use the system assembled in the previous step and add an empty cage without a post/post holder after the second cage, using rods to support and connect it to the system of the two initial cages.

Insert L_1 in the first cage. To align the beam expander, L_2 must have a translation degree of freedom. Therefore, this lens should not have an integrated post. Hence, insert L_2 in the third cage, in which the third dioptric surface is the infinite radius surface of L_2, as

represented in Figure 3.4. Then, moving L_2, space the two lenses at an initial distance of the sum of the focal lengths of the two lenses.

Then, add a fourth cage after L_2. Insert a target in the new cage with a connected post/post holder, fixing its height and lateral position equal to the optical system.

Afterwards, verify the collimation of the beam in the target, by adjusting the horizontal position of L_2, using the rods. Move the new cage further from L_2 to verify that the beam is constant until a length of 2 meters, using the system previously assembled in step 1.1. If the collimation is correct, fix the L_2 cage by tightening the rods' crews.

- *The output signal is collimated when the dimensions of the light beam are constant (diameter and position) throughout the optical system.*
- *At the end of this step, all rods' crews should be tightened to conserve the alignment.*

Step 1.4: Alignment of L_3

Fix the fourth cage in the optical table after L_2. Substitute two rods of the system from L_1 to L_2 for longer rods that reach the fourth cage of the system (attention - be sure that all screws of the rods not being replaced are tightened to conserve the previous alignment). Then, replace the other two rods. Remove the target and insert L_3 into the fourth cage.

Afterwards, connect the sample holder (USC), presented in subsection 3.3.1, to a post/post holder and place it onto the optical table after L_3 using a clamping fork system. Then, insert an alignment disk in a compatible Ø 30 mm mount in the USC. Finally, move the USC until the centre of the target is aligned with the focal point of L_3. When the optimal alignment is achieved, fix the USC in the optical table using a clamping fork.

- *At the end of this protocol, the rods' screws should be tightened, and the position of the elements should be conserved.*
- *Additional rods from USC to L_3 can be added to improve support to the system.*

3.5.2. Transmission Branch

Step 2.1: Replacement of the optical fibre system to simulate a visible sample

Substitute the target inserted in the USC by the optical fibre adapter, previously connected to the metallic adapter, both presented in Figure 3.2. Assemble the OFS presented in Appendix C, which is used to simulate the light emitted by the sample after excitation. Then, attach the FC/CT connecter of the fibre of the OFS to the metallic adapter.

Step 2.2: Positioning of L_4. Verification of the collimated beam.

Make use of another system of three Ø 30 mm cages and connect them with rods. Finally, distance the cages at least 35 mm from each other. Connect the system metal cage to the optical table with a post and post holder. Set the height of the system as the same as the previous system (attention – rods from the USC system could be connected to the rods of this system for added support).

Then, in the first cage insert L_4 using a compatible mount. Place the sample in the focal point of this lens by moving the lens and not the sample. To do so, test the collimation of the output beam up to 2 meters using an alignment target. Reposition the lens if necessary. Fix L_4 position tightening the rods' crews when a collimated beam is achieved.

Step 2.3: Positioning of L_5.

Place L_5 into the third cage of this system at a distance of a few centimetres from L_4.

- *Take into consideration the space needed to introduce the filter with a compatible mount between the lenses L_4 and L_5.*

3.5.3. Spectrograph

Step 3.1: Fixation of the slit in the focal point of L_5.

Attach a Ø 30 mm cage with a post, a post holder, a ring and a clamping fork system. Then insert the slit in a compatible mount in the cage system, with the slit vertically oriented. Place the centre of the slit in the light focal point of L_5, by moving its position. Verify if the output beam is a well-defined line, with minimal width possible using a white paper board or a new cage with an alignment disk placed in front of the slit.

If the beam is not a vertical line, move the slit in a lateral direction or adjust the post height. If the line is not vertically aligned with the slit, rotate the mount's slit. After the verification of the correct positioning angle and height of the slit, tighten the rods of the slit mount in the cage, and fix position of L_5's by tightening the rods' crews.

Step 3.2: Placement of L_6.

Place a new cage after the slit using connecting rods. Insert L_6 in the new cage, using a compatible mount. Distance the slit from L_6 by a dimension equal to the lens focal length. Verify the collimation of the reflected light using a target or whiteboard at a distance

of at least 300 mm. Correct the lens position to obtain a collimated beam. Finally, fix the lens position in the cage system.

Step 3.3: Adjustments using the excitation laser

Afterwards, remove the optical fibre adapter of the USC. Turn on the excitation laser and verify the collimation of the intermediate beams and focal points. Rectify positioning if needed by small adjustments of the lenses' positions.

Step 3.4: Placement of the transmission grating element and the detection system.

Place the transmission grating in front of the collimated beam and ensure that the slit image falls inside the grating.

Then, place the detection system (imaging sensor detector + L_7) in the signal's first order of diffraction, using the designed Detector Fixation System, DFS, presented in Appendix A. Connect the PC to the camera and initiate MATLAB Image acquisition App from *Image Processing Toolbox*.

Step 3.5: Insert a neon lamp in the UCS.

Step 3.6: Verify the collimation of the neon lamp emission bands and repeat steps 3.2 and 3.3 to optimize the alignment obtained.

- *By the end of this protocol, the spectrometer is covered with a black card box, and the image viewed in the interface software should be continuous, stable, and have well-defined spectral bands.*

3.6. Calibration Samples

Several components were used for the calibration of the spectrometer: alignment disk and various spectral lamps of different elements: halogen, neon and mercury.

The main laser excitation wavelength is 976 nm, and so, invisible to the human eye. For this reason, fluorescing laser viewing disks (with absorption bands in the NIR region and emission in the green region, added with visible target marks) were needed to see the laser beam. Moreover, the 1.5 mm hole in the disk centre helps the alignment of the laser's output beam into the first lens's optical centre. Furthermore, after the beam expander, the spot size enlarges significantly, and so, a metric target helped to increase the alignment precision.

3.6.1. Spectral Lamps

Two types of lamps were used to calibrate the prototype spectrum: continuous emission spectrum lamp (halogen lamp) and discontinuous emission lamp (mercury lamp or simply Hg lamp).

The halogen lamp was employed in the coarse calibration to define the ROI of the prototype's field of view since the halogen emission spectrum is continuous. (This lamp's adapter post is described in Appendix A).

In contrast, the emission spectrums of neon and mercury are discontinuous, *i.e.*, it is possible to see several characteristic atomic emission bands according to the different ions of the elements present in the lamps. In this way, the neon lamp was used to improve the alignment of the optical components and the mercury lamp is utilized in the fine calibration since the spectrum bands are more intense and reduced in number compared to the neon lamp's spectrum.

3.6.2. Raman Standard Sample

The ultimate goal of this project was to develop a Raman spectrometer. Accordingly, to test the its sensitivity to Raman signals, a Raman shift standard material was used, cyclohexane.

Cyclohexane, C_6H_{12}, is well established in the literature as a Raman shift standard material, approved by the ASTM[5] subcommittee on RS. Therefore, with well-known band wavenumbers, it is often used by spectroscopists to calibrate the Raman shift x-axis of the devices developed. A standard spectrum of this substance is presented in Figure3.6. On the right side, is possible to see that cyclohexane's HWVN spectral region has well defined bands, making this substance ideal to calibrate SWIR-Raman spectrometers. In this application, the cyclohexane sample was loaded in a quartz cuvette mount.

After assembling the entire setup, it is necessary to process and calibrate the data acquired by the detection system. This was divided into two parts: the **non-spectral axis transformation**, *i.e.*, convert the y-axis from pixels lines into relative intensity (counts), and the **spectral axis calibration**, *i.e.*, convert the x-axis from pixels columns to wavelength units.

[5] ASTM - American Society for Testing and Materials

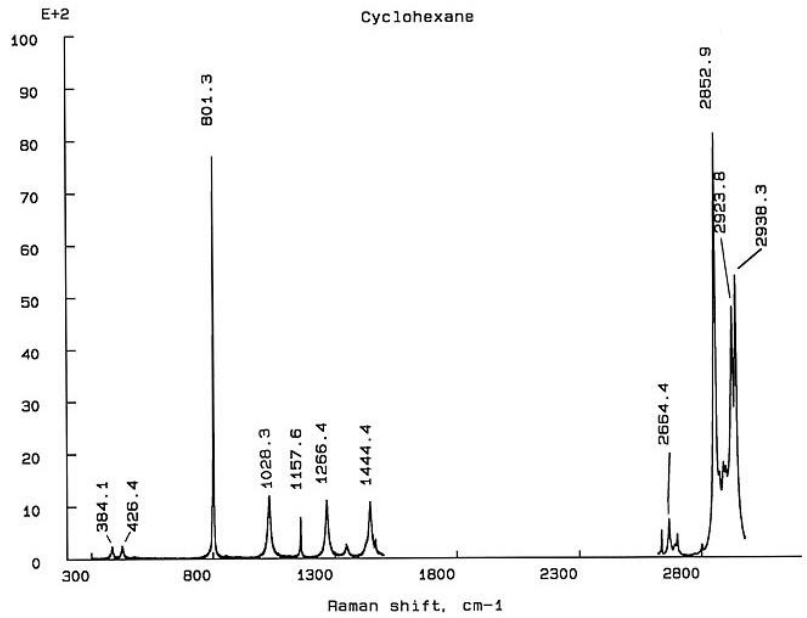

Figure 3.6 – Cyclohexane Raman standard spectrum (average of FT-Raman and Scanning (SPEX 1403) Data Sets) [6].

These two operations were performed throughout computational transformations of the two-dimensional (2D) signal if it is an image, or three-dimensional (3D) signal if is a video, acquired by the detector image sensor, using *MATLAB R2020b*, resulting in a spectra.

3.6.3. Non-spectral Axis Transformation: Binning and Stacking

The y-axis transformation had the function of changing the signal acquired with the detector system into a spectrum, *i.e.*, converting the y-axis from pixel lines into relative intensity (cumulated pixel counts).

Each video is composed of different images, also called frames. Each frame is represented by a matrix, called the intensity matrix, with the dimensions of the sensor used. In this case, the sensor dimensions are 1024 lines and 1280 columns of pixels, creating a matrix of 1024x1280 pixels for each frame.

Hence, in acquisitions with only one frame, *i.e.*, a single image, the transformation of the y-axis was done by a computational process called **vertical binning** or simply binning. On the other hand, if the acquisition was of more than one frame, *i.e.*, a video, immediately after the binning process of each frame, a new computational operation, called **stacking**, was also performed.

[6] McCreery Research Group 2014 , (http://www.chem.ualberta.ca/~mccreery/ramanmaterials.html) ASTM E 1840.

3.6.3.1. Binning

The binning consists of obtaining the computational addition of the adjacent pixels' values in each column that compose the intensity matrix of a frame (m), represented by each red rectangle in Figure 3.7. Hence, the result was a 1x1280 array, which represents the summed elements of the 1024 pixel's lines, j = {1, …, 1024}, of the 1280 pixels' columns, i = {1, …, 1280}, of a frame, m=1. The units of the binning are arbitrary (A.U.) since it measures the counts of the relative intensity of each column of the spectrum of a frame, represented by a green rectangle in Figure 3.7.

This computational operation was performed in real-time, allowing to adjust minimal differences in setup elements positioning, in order to obtain the smallest band width and ultimately, improve the resolution of the final spectrum. Therefore, binning in real-time allowed the improvement of the alignment of the prototype achieved with the protocols.

3.6.3.2. Stacking

The stacking consists of the computational conversion of a video into a spectrum. Therefore, first the binning of each frame of the acquired video, m = {1, …, k}, (represented by green rectangles in Figure 3.7) is done, resulting in one array for each frame. Then, the elements of the arrays obtained are summed, originating a new 1x1280 array of accumulated intensity, as seen in Figure 3.7.

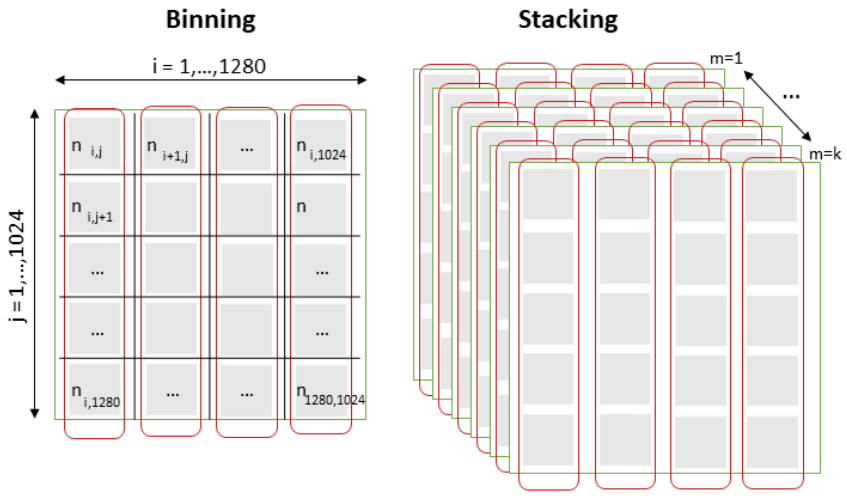

Figure 3.7 – Non-spectral axis transformation. Binning (left) and stacking (right) processes, which convert the y-axis from individual pixel counts into signal intensity counts. Each frame (represented by "m") is a matrix (represented by a green rectangle) of dimensions equal to the number of pixels in the sensor imaging used, in this case: 1024 x 1280, in which "j" is the number of lines and "i" is the number of columns. The red rectangles represent the columns that, after those column elements are summed, will result in the array (binning). If the number of frames is more than one, after binning of each frame, it will be performed the addition of the elements in an array of frames 1 to k (stacking).

In this manner, it is expected that, after stacking, spectral bands with low number of counts will be differentiated from the spectrum baseline, when compared to the spectrum obtained with only one frame [129].

In this dissertation, the stacking process was used to increase the counts of the bands in the Raman signal of cyclohexane.

3.6.4. Spectral Axis Calibration: Coarse and Fine Calibrations

The x-axis calibration (from pixel numbers to wavelength units) was divided into two parts: a more general adjustment first, hereafter designated as **coarse calibration**, and a more refined one, hereafter designated **fine calibration**.

3.6.4.1. Coarse Calibration

The coarse calibration consists of the definition of the field of view of the prototype, converting the x-axis from pixels to wavelength units. Therefore, images from the halogen lamp, combined with several filters, were acquired in order to establish a correlation between spectrum pixels of the halogen lamp and the theoretical edges of the filters used. This was possible due to two facts: (i) the halogen's emission spectrum is continuous, and (ii) the transmission filters used have an OD greater than 4. This means that the images resulting from the combination of the filters and the continuous spectrum of the halogen lamp will provide a well-defined delimitation in the filters cut-off wavelength.

Thus, the coarse calibration was performed using a halogen lamp combined with three different transmission filters: a 769/41 nm bandpass filter (EO84089), a second bandpass filter of 750/50nm (EO84089) and a 980 nm high-pass filter (980-LP02-980RE-28).

Then, the halogen lamp was positioned in the post holder of the sample using the designed post in Appendix A, and the filters were introduced in the intended mount between L_4 and L_5 to acquire the respective spectra.

Therefore, the first step of the coarse calibration was to acquire snapshots of the different combinations of the halogen lamp and the filters: (i) without filters, (ii) with 769/41nm filter, (iii) with 750/50 nm filter and finally (iv) with 980 nm filter, while real-time binning was performed using MATLAB as an interface.

After acquiring and saving this 2D data, a linear regression was performed using the following values: the theoretical cut-off wavelengths of the filters used and their

correspondent spectral values in the acquired data of halogen lamp images, thereafter called pixel numbers.

The filters' cut-off wavelengths are the theoretical wavelengths values corresponding to 50% of the transmitted signal and were obtained using each filter's datasheet. Afterwards, those values were listed in a table.

The pixel numbers of each spectrum of the halogen lamp correspond to the pixel columns where 50% of the signal is transmitted. Since the points where the first derivative of a function is null indicate that the tangent of the function is zero, those points can be either local maximum or minimum of the original function. Hence, a zero of the first derivative of halogen's spectrum corresponds to a pixel value with maximum local intensity, meaning that, in that column, the signal transmission is maximum. Thus, 50% of the transmission signal is given by the pixel column with half the maximum local intensity of the derivative.

Consequently, as illustrated in Figure 3.8, several steps were conducted: (i) the first derivative, y'(x), of each spectrum was calculated. Then, (ii) the respective zeros were found (or the derivatives' local maximum/ minimum values, when the function did not reach the zero value) - y'(x) = 0 -, which (iii) corresponded to the pixels' values with maximum local intensity in the spectrum of the lamp – y(a)=max(y(x)). Subsequently, (iv) the value of the pixel referring to half the maximum intensity of the derivative - $max\ (y(x))/_2 = y(b)$ - is registered as pixel numbers (value b).

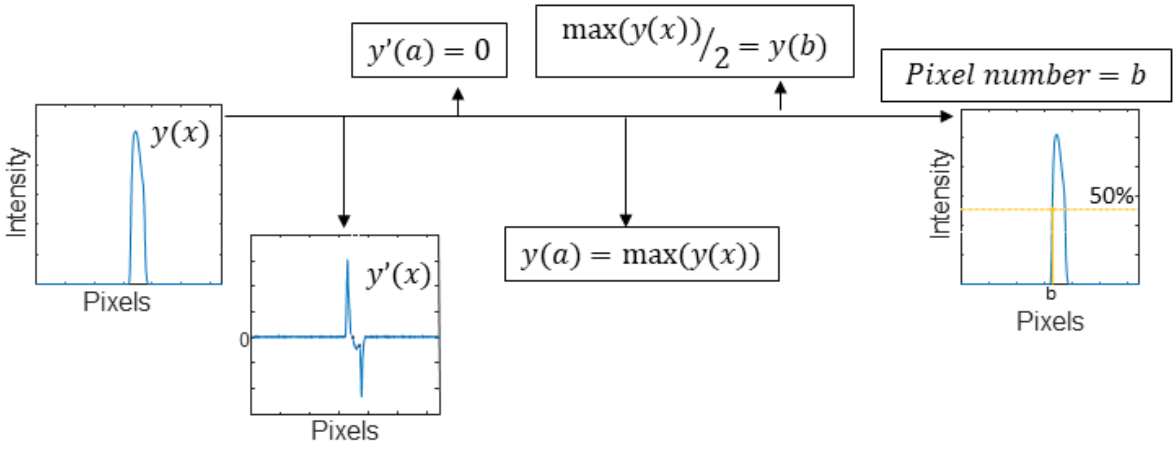

Figure 3.8 – Pixel number calculation.

Additionally, to evaluate the calibration, the determination coefficient (R^2) was obtained. A value closer to 1, indicates a good calibration result.

3.6.4.2. Fine Calibration

The fine calibration consists of a correlation between the spectrum of the Hg lamp acquired by a calibrated spectrometer - in this case, SPEX 1403 by *Spex Inc.*- and the prototype.

By making use of the same lamp, it will be expected that the same bands would be seen in the two spectrometers since it is certain that the element ions are present in the lamp, and, furthermore, the spectrum, would be equal. Therefore, a calibrated spectrometer will give the exact wavenumber of the spectral bands of the lamp, and so a new regression can be performed using the well-defined and resolved spectral bands in which the correlation is unequivocal between the two spectrometers' acquisitions. Thus, this regression is performed to correct possible lateral shift in the prototype spectrum and subsequently, the overlap of the two spectrometers data, the SPEX calibrated spectrum and the prototype final spectrum after regression, is expected as the result of this calibration.

The SPEX 1403 has a resolution of 0.005 nm and 0.3 nm/mm of dispersion[7]. The excitation source used with this spectrometer was a 514.5 nm laser. Also, all the spectra acquired in the SPEX 1403, were fixated at a range of [18, 6103] cm^{-1}, which applying the equation 2.1 correspond to [515, 750] nm. This upper limit of the analysed region, 750 nm, was imposed by the limitation of this spectrometer. The integration time was set at 1 s with an increment of 0.5 cm^{-1}. Upon some tests to improve the resolution of the spectrum bands, the entrance and end slits sizes were set at 50 µm each. To reject stray light, the medium slits were set at 700 µm.

The chosen lamp was a mercury one, due to the intense, well-defined bands of its emission spectrum in the ROI, which comprises a wavelength range between 500 and 750nm.

Hence, in this last calibration procedure, the halogen lamp is substituted by the sample holder, which should not be removed further, and so, rods in this cage should be placed and immobilized. Thereafter, this calibration protocol should be done after any change in the setup alignment and, upon that, repeated periodically.

Then, comparably to the data obtained with the halogen lamp, four snapshots of the combination between the Hg lamp and the transmission filters were obtained. However,

[7] https://www.horiba.com/en_en/products/scientific/custom-spectroscopy-solutions/spectrometers-and-monochromators/legacy-monochromators/

since the SPEX 1403 spectrometer has a limitation in the range of the wavelength above 750nm, only the spectrum without filters was used to determine the correlation spectral points of the Hg lamp spectrum obtained in the prototype. Nonetheless, the 750/50 nm filter spectrum was used to verify the final calibration of the prototype since this filter transmits the signal from 725 nm, which is still in the ROI of this calibration.

Afterwards, to reduce the influence of the background noise, the 2D images were cut vertically using the function of MATLAB *imcroop()* to only select the region in which the bands are observed.

Then, unequivocal bands of the SPEX's and prototype's spectra are matched and registered, followed by a new regression. Finally, similarly to the procedure in the coarse calibration, the determination coefficient (R^2) was obtained to evaluate the fine calibration.

4. RESULTS AND DISCUSSION

In chapter 4, the results of the simulation and the physical assembly of the prototype are presented, in 4.1 and 4.2, respectively. Then, in 4.3, the mechanical parts designed to build a low tolerance setup are shown, and, in 4.4, the results of the calibration procedures are demonstrated and discussed. Finally, in 4.5, the cyclohexane Raman acquisitions results are also shown, using the two red lasers and the stacking process.

4.1. Simulations

The simulation of the assembly setup was made in *3DOptix* online software, an optical simulation software. In the simulation setup, represented in Figure 4.1, the lenses (L_1 to L_6), the dichroic filter (F), and the transmission grating (G) are the same references as those later implemented on the physical setup. The laser used in the simulation is the most similar to the one necessary for the final application (976 nm from *Innovative Photonic Solutions)*, having an excitation wavelength of 940 nm (Thorlabs M940L3 - 940 nm). However, the beam dimensions are equal to the one presented in Table 2, *i.e.*, 0.6 mm. Finally, the detector is represented by a screen (D).

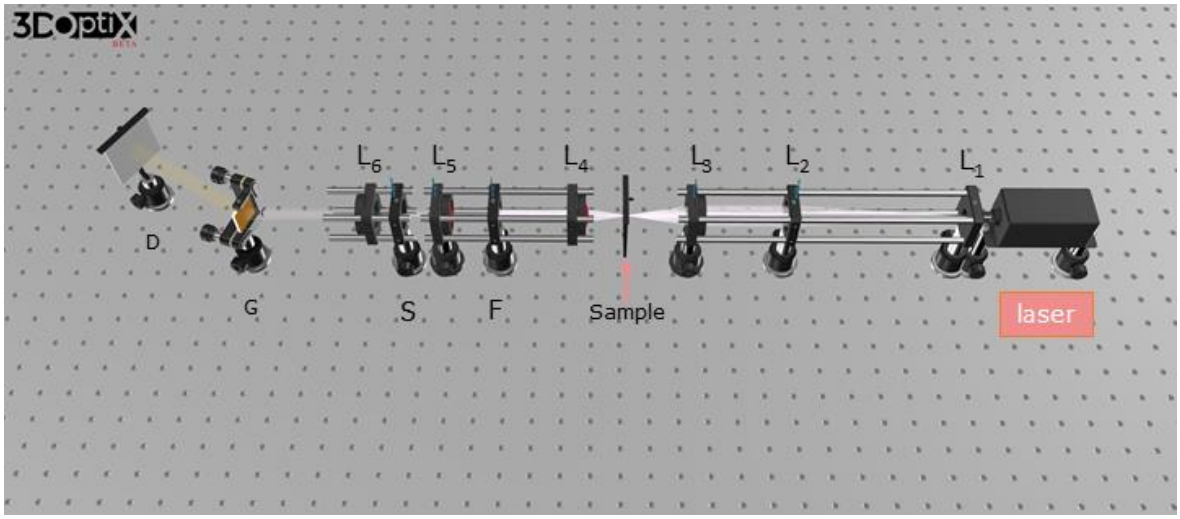

Figure 4.1 – Setup simulation in *3Doptix* software. It is composed of the laser, lenses from 1 to 6 (L_1 to L_6), Sample, Filter (F), Entrance Slit (S), Transmission Grating (G), and Detector (D)

Due to the novelty of the software, the entrance slit element (S) is not available in the setup. Nonetheless, the position of this element is preserved and labelled in the simulation by an empty mount.

Hence, with this simulation, it is possible to verify the expanded beam dimensions as well as the spot size in the sample plane detector (Sample). The first is less than 18 mm (Ø 17.56 mm) and the second is 0.34 mm x 0.33 mm, as seen in Figure 4.2.

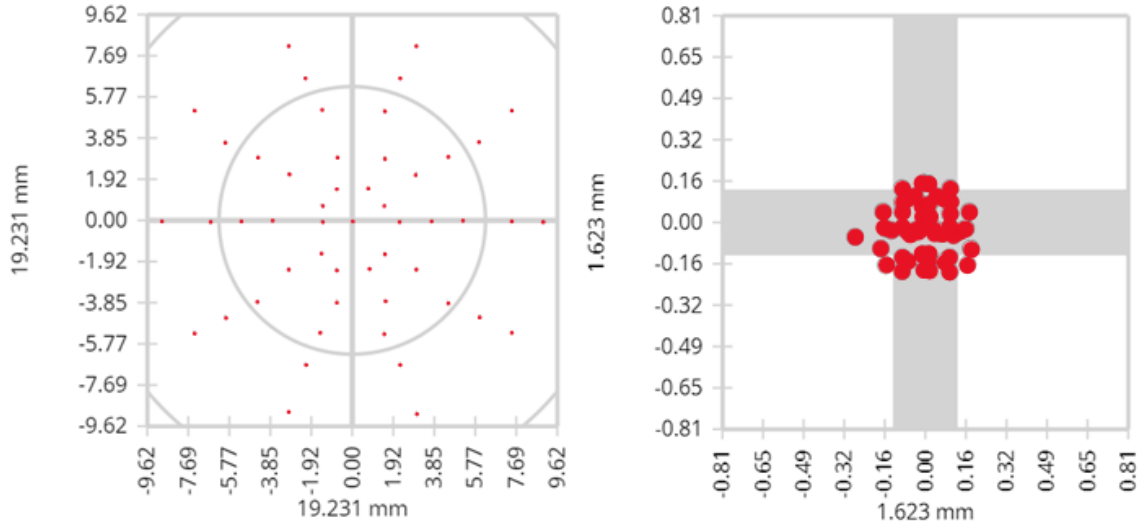

Figure 4.2 - Simulation of the beam expander (left) and sample spot size (right) dimensions.

The expanded beam value of simulation (Ø 17.56 mm) is according to the theoretical value obtained with the paraxial optics method, presented in Table 3 (Ø17.59mm). However, the same is not verified when comparing the simulated and the theoretical sample spot sizes, where the latter is also presented in Table 3. The simulated value is two orders of magnitude higher than the theoretical value (340 – 4.2 µm). This could be due to the laser used in the simulation being in fact a LED, which has a broad emission curve, with 37 nm of bandwidth (FWHM). Therefore, several wavelengths will be emitted and cause chromatic aberrations in the optical elements, even though this effect may be minimized by the use of an achromatic lens (L_3). Consequently, the sample focal point is enlarged. Moreover, due to the software characteristic discrete variations of 0.01 mm, the smallest spot size detected may not be the exact localization of the sample focal point.

4.2. Setup Assembly

The assembled prototype is shown in Figure 4.3. The black card boxes reduce the ambient light interference, as well as decoupling the excitation and transmission branches from the prototype entrance slit, which reduces the interferences from stray light. Nevertheless, all data acquisitions were obtained with no ambient lights, to minimize ambient noise.

Figure 4.3 – Prototype assembled in the optical table, including the host computer, the acquisition branch-box, the transmission and excitation branches-box, and finally, the laser.

On the left side of Figure 4.4, the excitation and transmission branches are represented, and on the right side, the acquisition branch is shown. The black-painted boxes that cover the setup are coated by thick and rough felt to avoid specular reflections on the walls of the boxes, minimizing the background noise. This material was also used to cover the optical table floor, to prevent light reflection in the polished surfaces. In addition, due to the dispersion verified while using the visible wavelength lasers, the beam expander's emitted light is blocked before the sample by a barrier made of the same black material.

All the optical components are visualized in Figure 4.4: lenses (L_1, L_2, L_3, L_4, L_5, L_6 and L_7), filter (F), entrance slit (S), transmission grating (G), detection system (D) Furthermore, it is also possible to see some of the design mechanical parts: USC system (Sample) mounted in the transmission branch (left side) and, the Detector Fixation System, DFS, (in D) -description in Appendix A-, held by a clamp (right side).

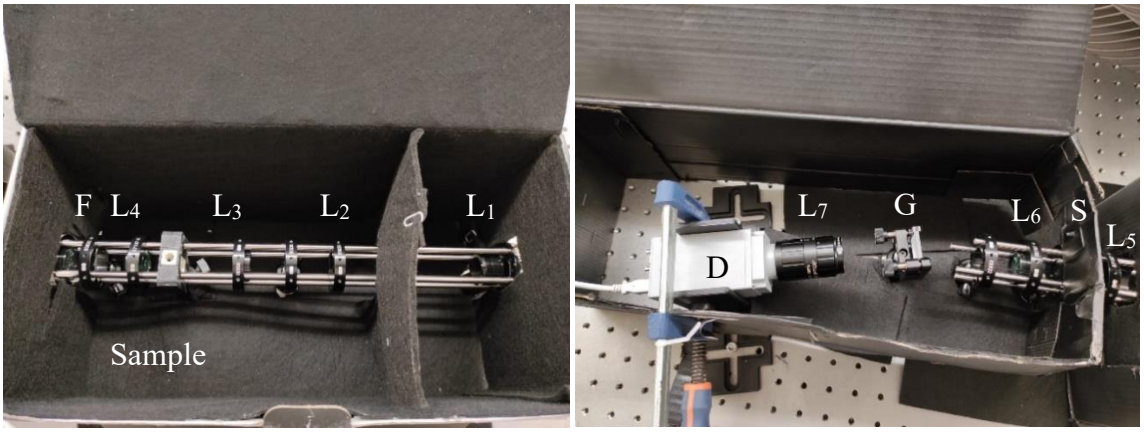

Figure 4.4 – Excitation and transmission branches (left) and acquisition branch (right). Lenses (L_1, L_2, L_3, L_4, L_5, L_6 and L_7), Sample (with the designed USC system), entrance slit (S), transmission grating (G), detection system (D) with the designed fixation system DFS.

The experimental beam expander dimension, using the 976 nm laser, is approximately 19 mm, as seen in Figure 4.5, which is in accordance with the simulation and theoretical values. On the other hand, with the red laser, the dispersion of the beam after L_1 is significant, therefore, the beam is limited to the clear aperture of L_2, (Ø 24.5 mm), which is significantly larger than the theoretically obtained (14.35 mm).

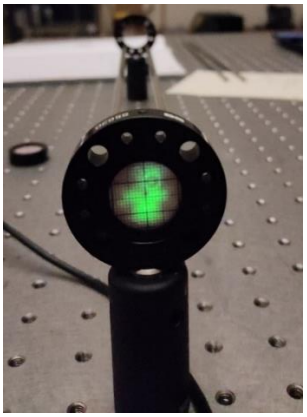

Figure 4.5 –Light beam expanded using infrared 976 nm laser.

Concerning the experimental sample spot sizes with both lasers, the red and infrared, are less than Ø 1.5 mm since the light passes entirely through the alignment disk's central aperture.

Also, the experimental optical distances between the lenses are dependent on the laser's excitation wavelengths and are resumed in Table 4. All the distances have been measured manually with a digital calliper with 0.01 mm of measurement uncertainty. Nevertheless, due to the ambiguity of each lens's central point, the measurements' error was considered as 2 mm.

Table 4 – Experimental results of separation between lenses for the different lasers used.

Laser Wavelengths (nm)	**976**	**632.8**	**640**
$\overline{\mathbf{L_2, L_1}}$ **(mm)**	151	155	148
$\overline{\mathbf{Sample, L_3}}$ **(mm)**	53	58	55
$\overline{\mathbf{L_3, Sample}}$ **(mm)**	37	35	36
$\overline{\boldsymbol{S, L_5}}$ **(mm)**	37	36	27
$\overline{\mathbf{L_6, S}}$ **(mm)**	34	36	33

The number of measurements could be increased in order to minimize the error. However, the main constrain will continue to be the localization of the lens' central point. Therefore, the estimated error will still be significative.

4.2.1. Parts Design to Allow Low Tolerance Variations

Figure 4.6 shows the part created – (a) unassembled, and (b) assembled in the setup – in order to support samples of different formats. The named Universal Sample Cage (USC) is very versatile, allowing samples to have variable dimensions: from a 13.5x13.5x40mm^3 parallelepiped to a Ø 30 mm cylindrical mount. Moreover, additional adapters were created, as depicted in Figure 4.7, to increase the versatility of the USC.

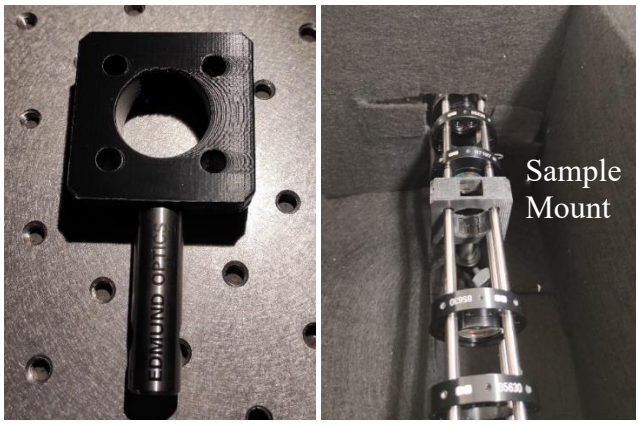

Figure 4.6 - Printed USC with the compatible post.

Figure 4.7 shows several objects integrated into the sample stage. In (a), the cyclohexane's cuvette inserted in the USC is presented. Then, (b) shows the target inserted in the mount's system. Afterwards, in (c) the 3D object designed to support the fibre optic (grey object) is shown. The cylindric part dimensions are Ø 30 mm (external diameter) and Ø 11 mm (internal diameter). This object is coupled with the metallic adapter of Ø 11 mm (cylindric metallic object) attached to the FC/CT optical fibre adapter. And, finally, in (d) the 3D object developed (white object) to support the Hg lamp is displayed. This object is a parallelepiped of 13.5x13.5x40 mm^3 where the Hg lamp is vertically inserted, as depicted in the Figure 4.7 (d).

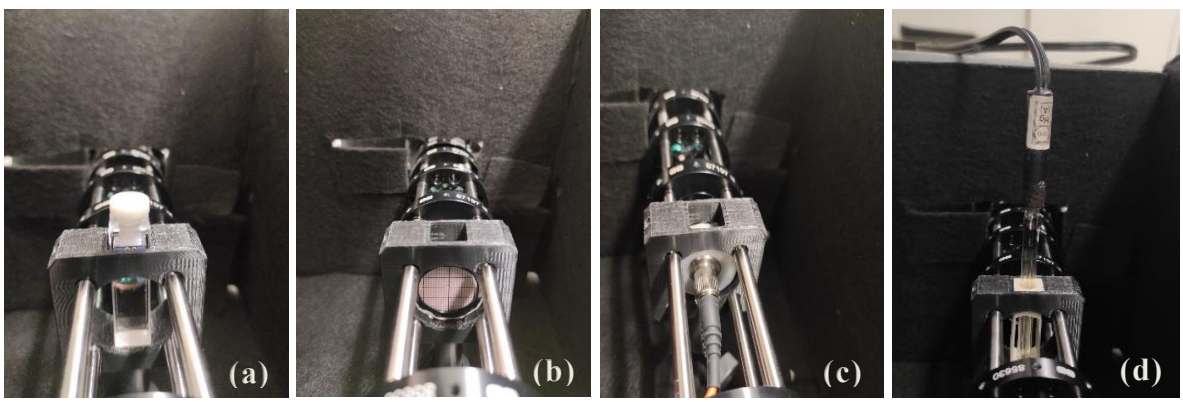

Figure 4.7- The USC is adaptable for every system required to place the sample: (a) cuvette; (b) target and (c) optical fibre and adapter, and (d) mount with the Hg lamp adapter.

4.3. Calibration

The computational calibration of the resulting images was done in *MATLAB R2020b* to obtain the x-axis conversion from pixels columns to units of wavelength, as mentioned in Chapter 3 – Materials and Methods. The calibration was divided into two parts: a more general adjustment first, called **coarse calibration**, and a more refined, called **fine calibration**.

4.3.1. Coarse Calibration

The images acquired in the coarse calibration of the different combinations of the halogen lamp and the filters are presented in Figure 4.8 (left) while the respective spectra are presented on the right side. Figure 4.8 is further divided into: halogen lamp (a) without filters; (b) with the 796/41 nm filter; (c) with the 750/50 nm filter, and finally (d) with the 980 nm filter. Observing the images in the figure, it is possible to conclude that the ROI is limited vertically from pixels' rows 245 to 790. Nevertheless, this calibration, being more general, uses the entire image, which could originate some background noise, but it was not considered significant when performing the analysis.

In all the four images of Figure 4.8, is possible to see a continuous emission spectrum. In the first image, (a), a continuous spectrum ending in pixel column 1000, showing the detected halogen spectrum without any filter. Secondly, in image (b), an emission bandwidth of approximately 100 pixels' columns, which corresponds to a 41 nm spectral band is observed. Then, in image (c), a larger bandwidth, corresponding to 50 nm is also noticed. Lastly, in image (d), an intense region of emission is observed until the 200th pixel column, with a well-defined edge, proving that the spectrum is horizontally inverted. This means that higher wavelengths are located on the left side of the snapshot, increasing horizontally from right to left. Additionally, the less intense signal emission in image (d) between pixel columns 750 and 1000 can be justified by the less efficient blocking of this filter in wavelength between 330 to 750 nm.

The coarse calibration procedure is based on the identification of the pixel column which corresponds to each filter's cut-off frequency, *i.e.*, where 50% of the signal of the halogen lamp is detected. It was determined as the pixels' values where half of the maximum local intensity of each filters' binning spectra were detected.

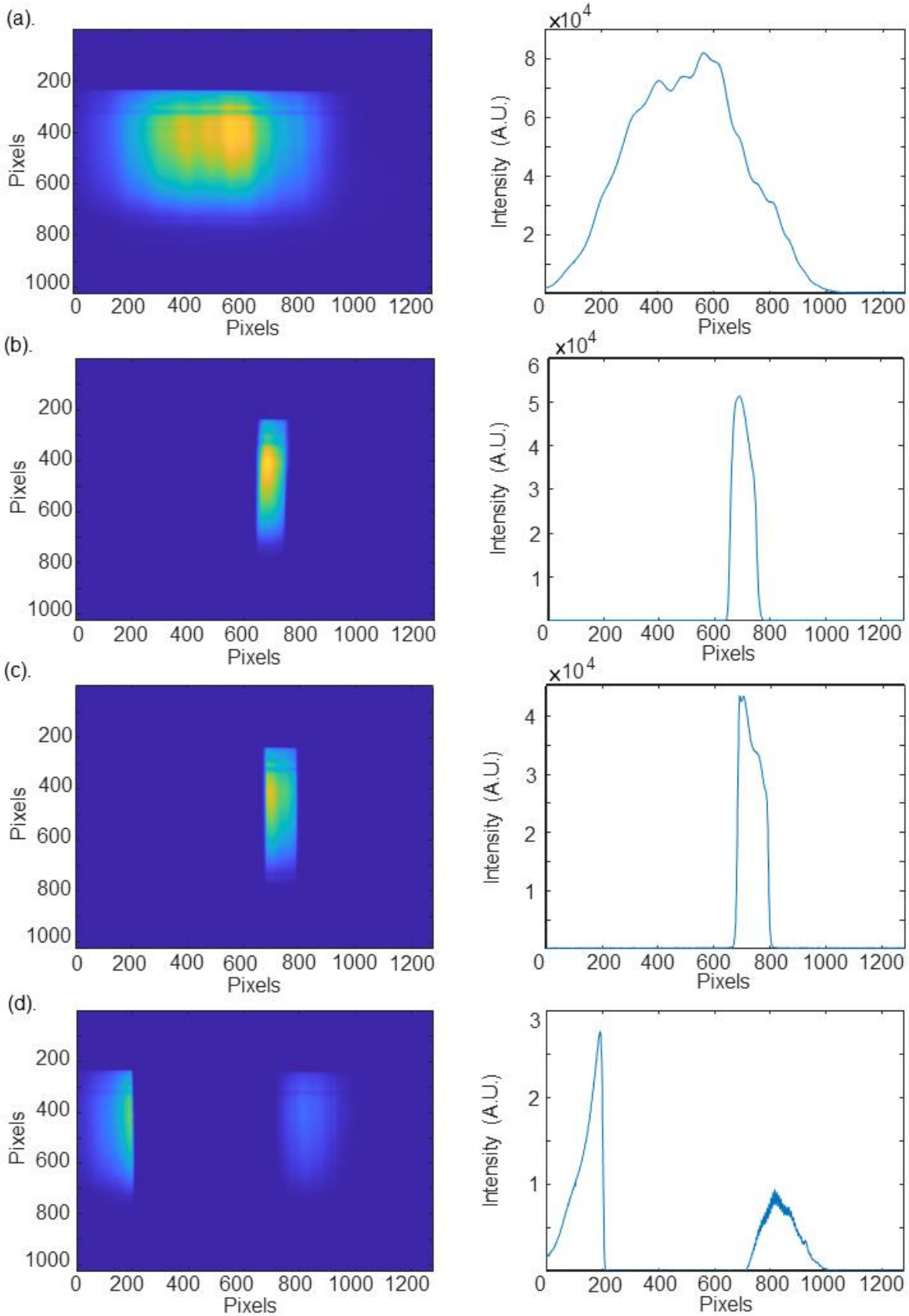

Figure 4.8 – Images of halogen lamp (left) and respective binning spectra (right) with an exposure time of 0.5 sec, and with different filters: (a) no filter, (b) 769/41 nm filter, (c) 750/50 nm filter and (d) 980 nm filter.

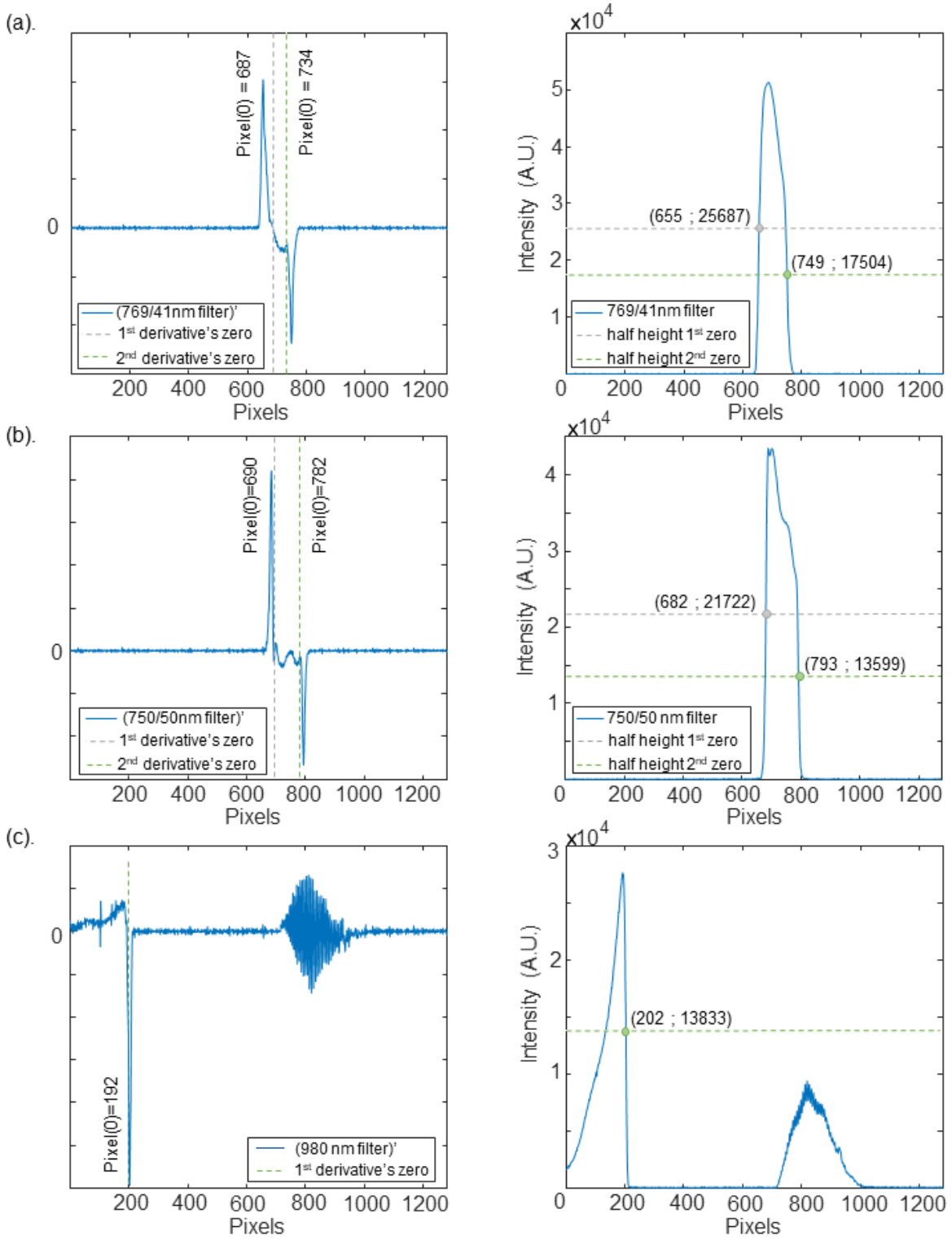

Figure 4.9 - First derivative of the halogen spectrum with various filters: (a) 769/41 nm; (b) 750/50 nm; and (c) 980 nm (left). Halogen lamp spectra and corresponding pixels of half of the height of the zeros of the derivatives (right).

The first derivatives of the spectra shown in Figure 4.9 (left) was used to identify the maximum local intensity by computing the respective derivatives' zeros. In the derivative

values where the zero is not verified, it was determined the local maximum/minimum of the region, *e.g.*, the second value of the derivative of 769/41 nm spectrum (Figure 4.9 (a)) is the maximum of the function. Subsequently, the value of the pixel column referring to half of the derivative zero's intensity was registered, as shown in Figure 4.9 (right). Those values, called pixel numbers, are also presented in Table 5.

Analysing the left side of Figure 4.9 (a), it is possible to verify that the two local maxima of the derivative of 769/41 nm filter image correspond to pixels columns 687 and 734. The relative accumulated intensity of these pixels' columns is, respectively, 5.2 x 10^4 counts and 3.5 x 10^4 counts. The pixels numbers corresponding to half of this intensity are on columns 655 and 749, respectively (Figure 4.9 (a) right). Similar analysis can be done to graphs (b) and (c), which correspond to 750/50 nm and 980 nm filters, respectively.

To compare the pixel number with a reference wavelength, the filters' theoretical transmission wavelength values corresponding to 50% of the transmitted signal are computed, through each filter's datasheet, and the results are presented in Figure 4.10 and summarized in Table 5. It is possible to see that the theoretical curves of the three filters have sharp edges, which will allow a good correlation of the data.

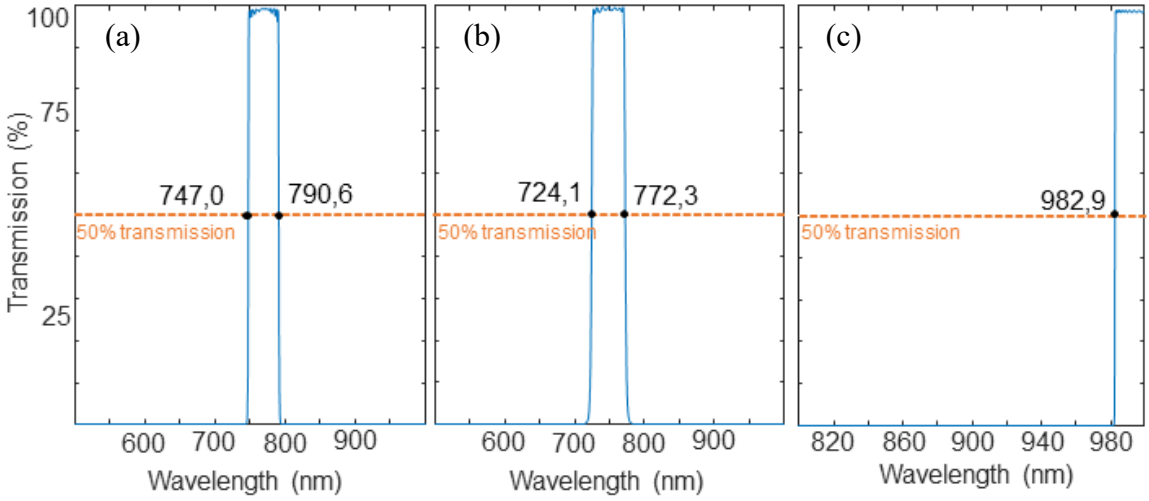

Figure 4.10 - Theoretical wavelengths values corresponding to 50% of the transmitted signal with the different filters: 769/41 nm (a), 750/50 nm (b), 980 nm (c).

Table 5 – Correspondence of pixel values and theorical wavelength of 50% of the transmitted filter signals.

Pixel number	793	749	682	655	202
Theorical Wavelength (nm)	724.08	747.00	772.32	790.57	982.89

To finish the Coarse Calibration, the linear regression done using the data resumed in Table 5 is given in Figure 4.11 (left). Consequently, the resulting adjustment of the spectrum is presented on the right side of Figure 4.11.

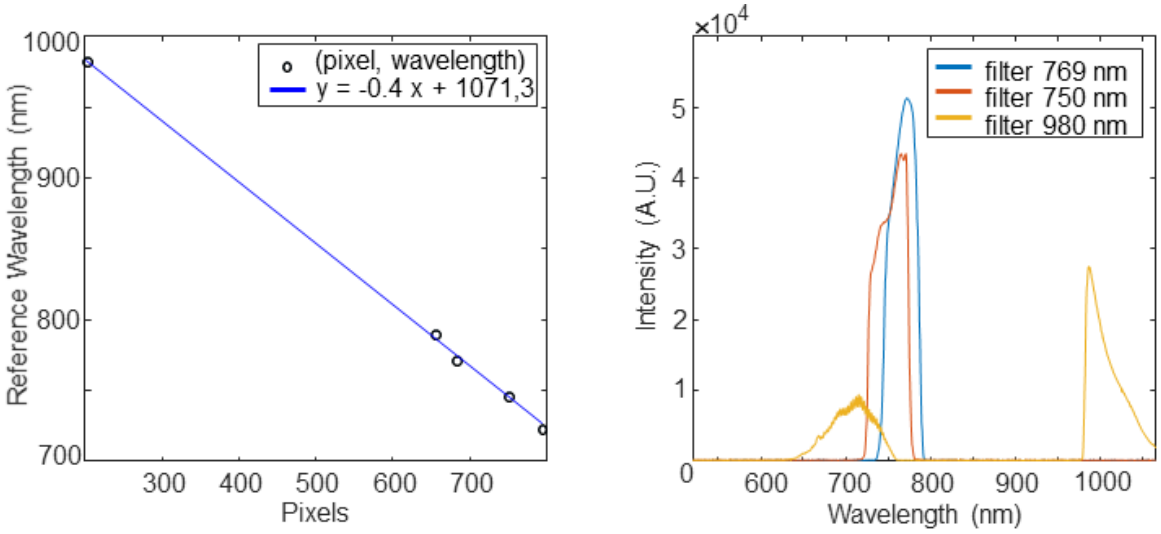

Figure 4.11 - Coarse Calibration Result (left). Linear regression using the data of Table 5 (right). The equation y=-0.4x+1071.5, where the x-axis and y-axis coordinates are the pixel numbers and the theoretical reference wavelengths.

The obtained correlation coefficient (R^2) value is 0.999, which indicates a very good correlation. The well-defined delimitation of the area visualized in the prototype's spectrum is provided by two characteristics of the filters used: their OD greater than 4, which results in an efficient blocking of the continuous emission spectrum of the halogen lamp outside the region of transmission of the signal, as well as the sharped transmission edges provided by the filters, especially the high-pass 980 nm filter (OD=6), which lets the transition be almost modulated as a step. However, the number of points used on the calibration is only five leading to possible errors in the final calibrated spectrum.

In order to improve the calibration results, an upgrade can be performed: adding more filters, in a wider wavelength range and with high OD, increasing the number of points used in the correlation. However, the purpose of this calibration is to implement a first general conversion from pixels to wavelength units, which has been successfully done.

4.3.2. Fine Calibration

A second procedure, more exhaustive, was implemented, called fine calibration. This calibration establishes a correlation between the spectrum of the same sample (Hg lamp) in a commercially calibrated spectrometer, the SPEX 1403, and the prototype.

As seen in Figure 4.12 (a), concerning the images acquired in the prototype, the spectral bands are only observed in the [245, 795] pixels vertical range. This is in accordance with the results presented in the previous section. Hence, since this is a more refined calibration, the data acquired by the prototype is cut vertically to reduce the influence of the noise from the other pixels. The cropped image is presented in Figure 4.12 (b). The direct comparison of the binning of the original and cropped images can be seen in the bottom graph (c), in which the background is reduced especially in the spectrum baseline.

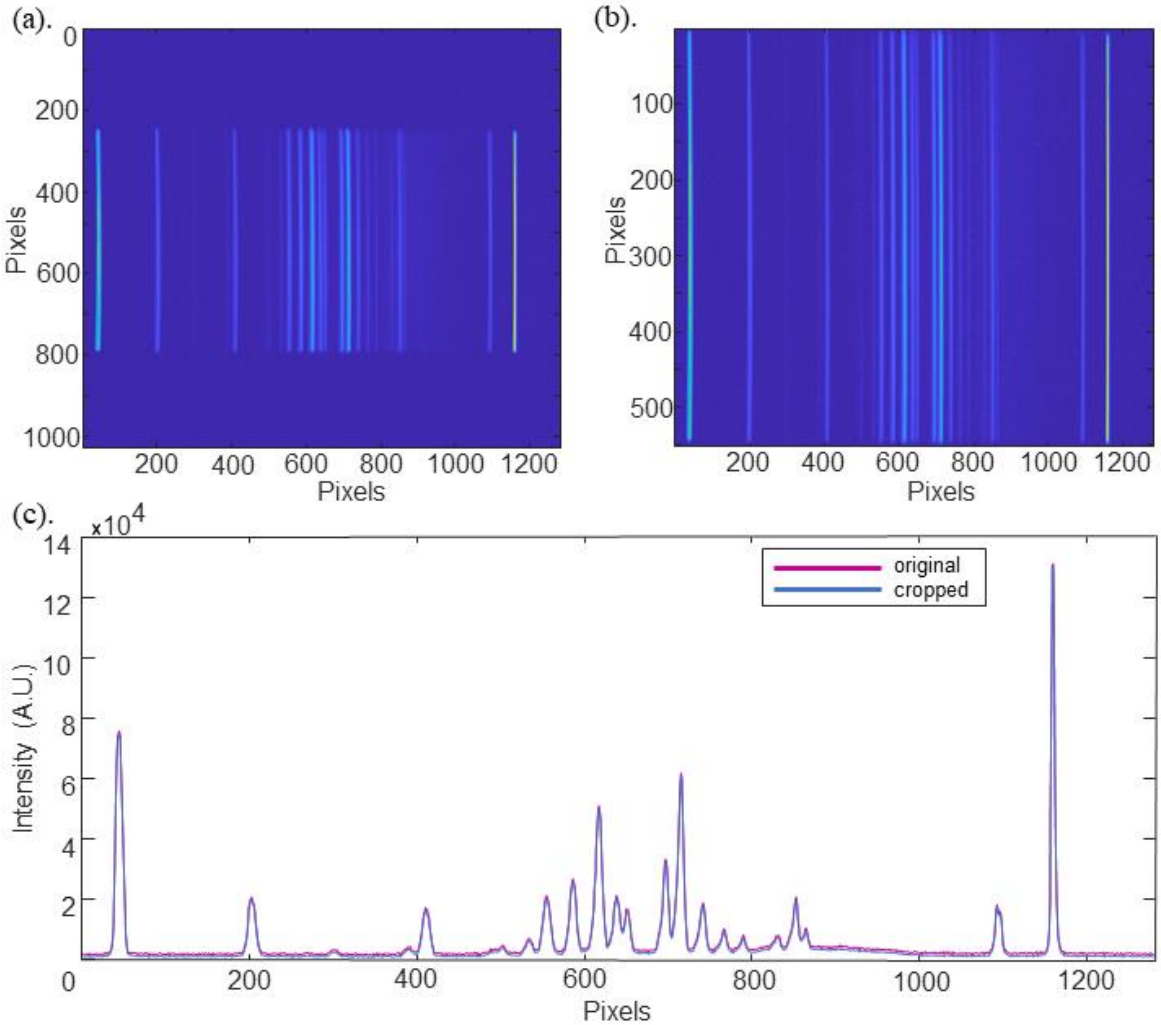

Figure 4.12 – Reduction of the background noise after image cropping. (a) Original image; (b) Cropped image; (c) spectra comparison obtained from the original and cropped images.

The data acquired with the Hg lamp using the prototype is presented in Figure 4.13. Similarly to the halogen lamp, four spectra were acquired with the combination between the lamp and the transmission filters.

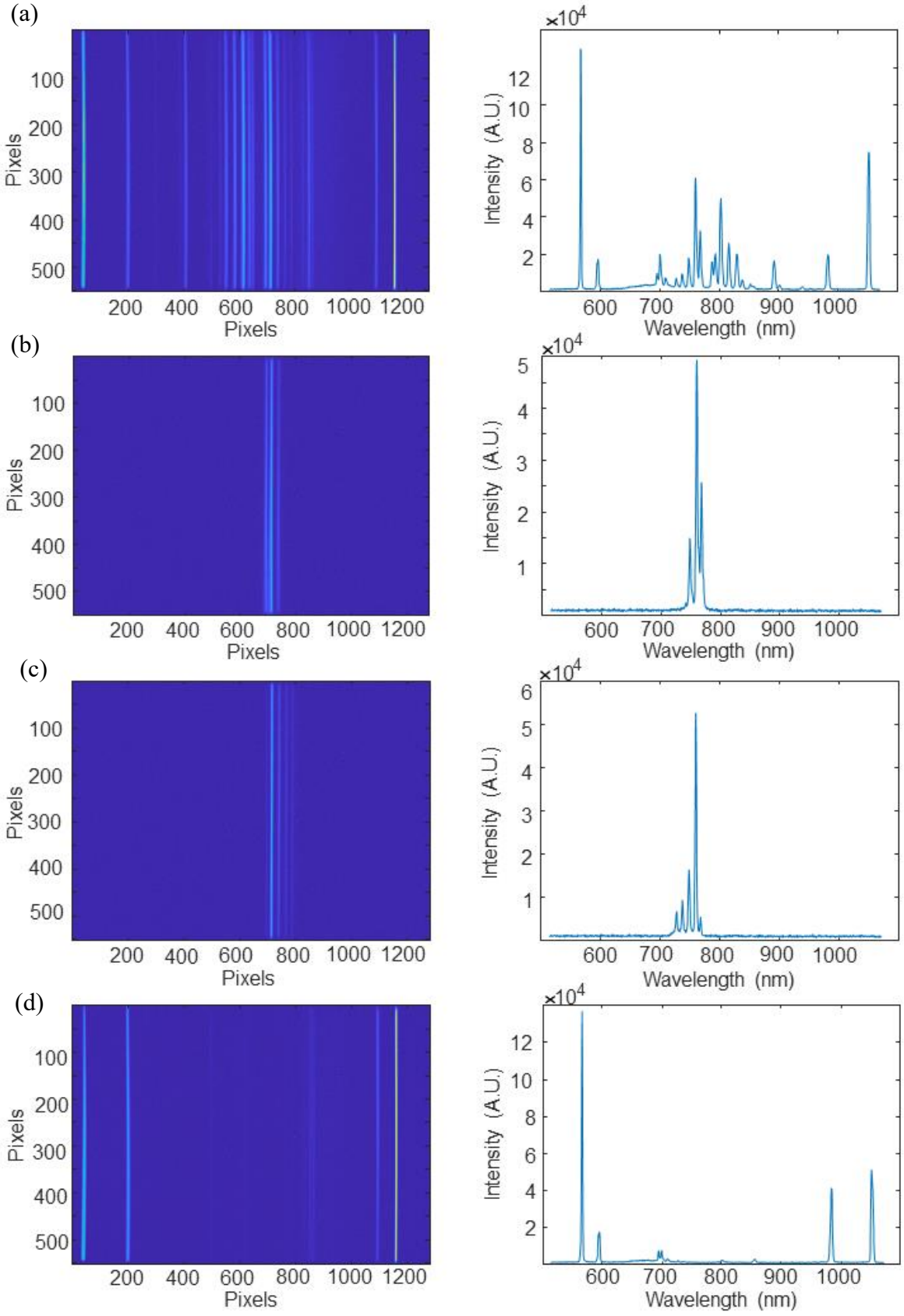

Figure 4.13- Spectra of a Hg lamp with (a) no filter, (b) 769/41 nm filter, (c) 750/50 nm filter, and (d) 980nm filter.

By analysing Figure 4.14, it is possible to see the superposition of the entire prototype's spectrum of the Hg lamp represented without filters (dark blue line), with the 769/41 nm bandpass filter (light blue line), the 750/50 nm bandpass filter (green line) and the 980 nm high pass filter (purple line). However, the SPEX 1403 upper spectral delimitation wavelength is close to 750 nm. This makes the wavelength's ROI to be only between 515 and 750 nm, as represented by dashed vertical lines in Figure 4.14.

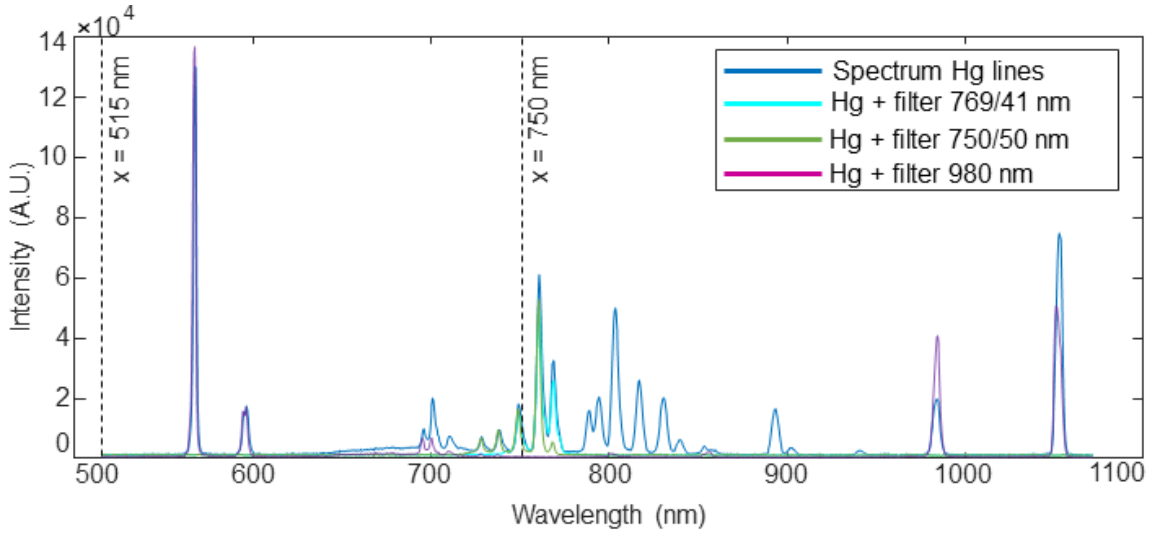

Figure 4.14 – Spectrum of Hg bands in the prototype without filter (dark blue), with 769/41 nm filter (light blue), with the 750/50 nm filter (green), and with 980 nm filter (purple). It is also represented the wavelength ROI used in this calibration [515;750] nm.

Consequently, the prototype data used to determine the correlation points in this calibration is the spectrum of the Hg lamp without filters (Figure 4.13 (a)). The spectrum of the Hg lamp with the filter of 750 nm (Figure 4.13 (c)) is used to confirm the calibration, since its transmission is from 725 nm.

Figure 4.15 presents the spectrum acquired in the SPEX 1403, in which the x-axis was converted from the acquisition unit, Raman Shift (cm^{-1}), to wavelength (nm), using equation 2.1. For this acquisition, the analysed range was set to [18, 6103] cm^{-1}, which corresponds to [515, 750] nm, with an integration time of 1 s and an increment of 0.5 cm^{-1}. The y-axis is on a logarithmic scale to better visualize the less intense Hg bands.

The overlap of the two spectra can be seen in Figure 4.16, top. In this graph, it is possible to verify that the prototype's spectrum is wavelength-shifted in reference to the SPEX's spectrum, showing that although the R^2 obtained in the coarse calibration was close to 1, the spectrum is not perfectly aligned.

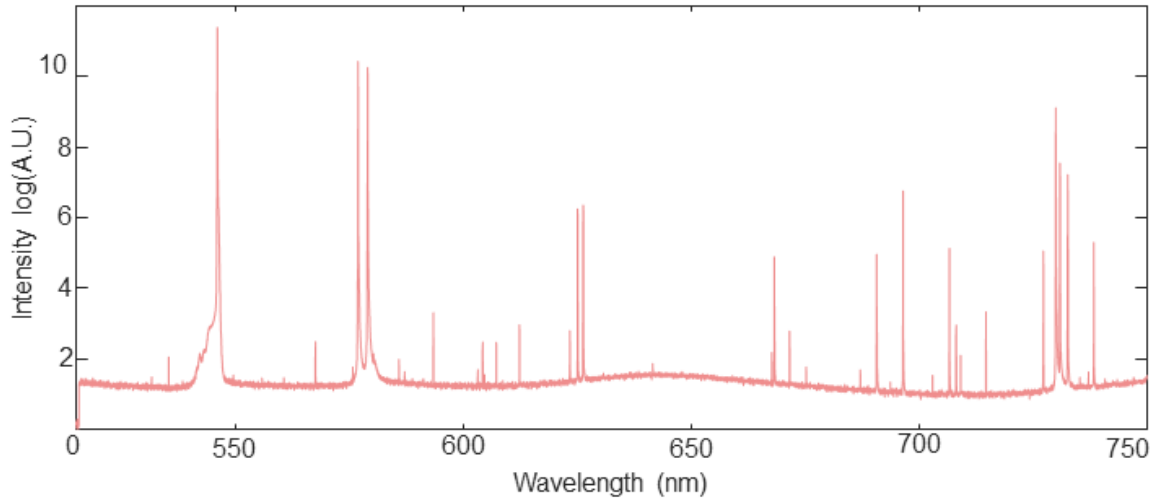

Figure 4.15 – Spectrum of Hg lamp using the SPEX 1403. The spectrum corresponds to the Raman shift converted in wavelength (nm) *vs.* the logarithmic scale of the intensity of the counts registered.

Table 6 – Linear calibration of the spectrum

Prototype (nm)	567.12	695.40	700.40
SPEX (nm)	545.98	690.62	696.41
After linear calibration (nm)	545.97	690.62	696.41
Residuals (nm)	0.0030	-0.0787	0.0758

Therefore, a new linear regression, using only unequivocal single bands in the two spectrometers was made using the values of the prototype and the reference spectra summarized in Table 6. The linear regression results in the equation $y = 1.1282x - 93.8558$. Also, point values of the prototype's spectrum, after the regression, and respective residuals of the correlation can be also found in Table 6.

The final shifted spectrum of the prototype is presented in Figure 4.16 (b), and the residuals underneath (c) The R^2 value of the linear regression is 1, connotating this recalibration with a good performance, as also proved by the minor quantities of the residual values. Additionally, the observation of the final spectrum allows us to conclude that the fine calibration is successful because the bands 545 nm, 690 nm, and 696 nm are coincident in the two spectra and the other two bands, not included in the regression, the 576 to 580 nm, match the large band in the prototype's spectrum.

However, by making use of the same lamp, it is expected that the equivalent bands would be seen in the two spectrometers. This is reasonable since it is certain that the element ions present in the lamp, and, subsequently, spectra, would be equal. Nevertheless, some bands in the prototype's spectrum, especially in the middle field of view (625 nm), are

missing. This can be justified by a misalignment between the camera and the diffraction grating. Moreover, the overlap of the bands above 725 nm isn't well defined. It was expected that a single intense band in the prototype's spectrum would be present, reflecting the four close bands that emerge on the SPEX spectrum. This lack of signal could not be justified.

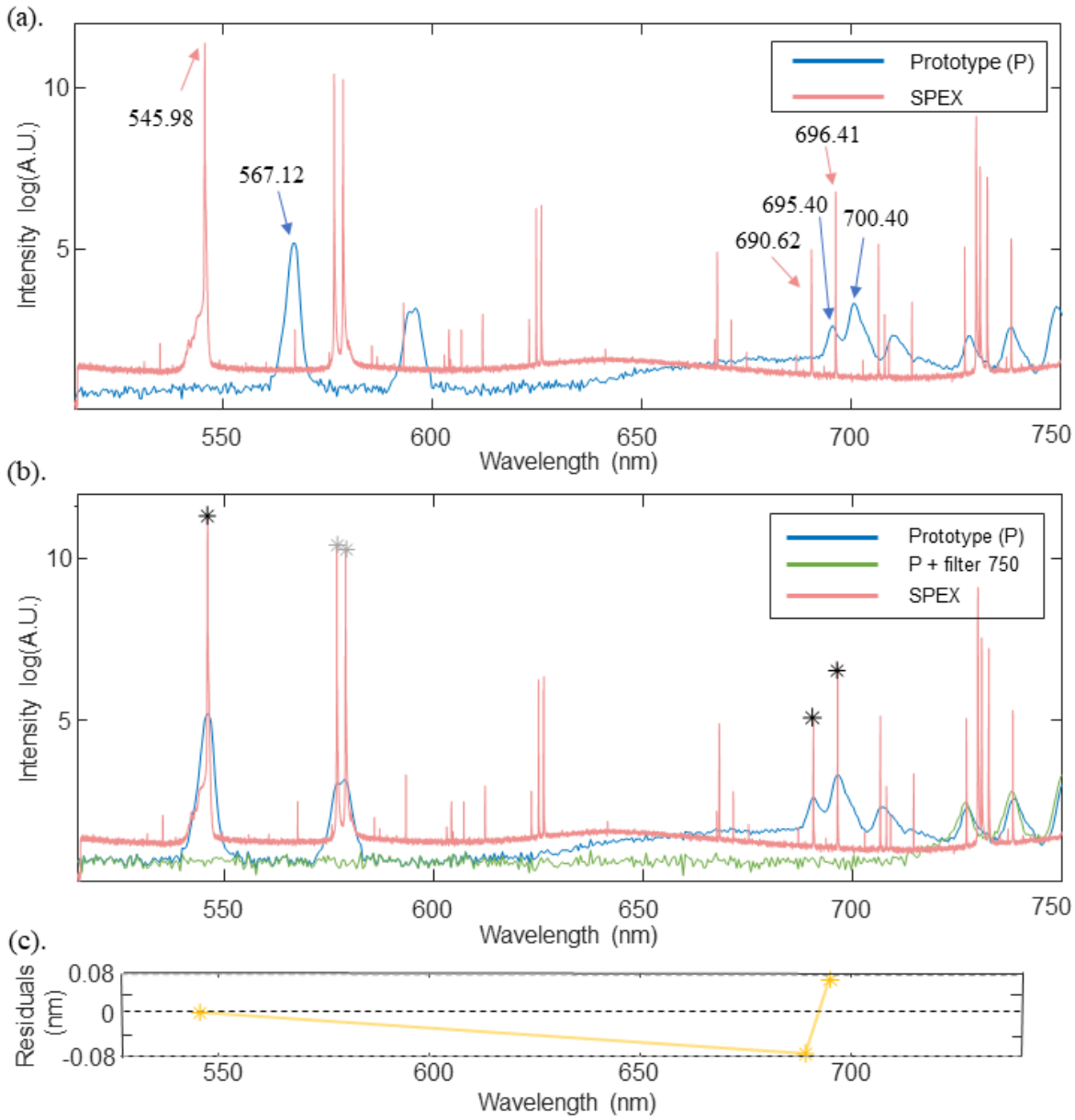

Figure 4.16 – Overlap of SPEX 1403 spectrum (red), the spectrum acquired with prototype without filters (blue) and with the 750/50 nm filter (green) of the same Hg lamp, before the fine calibration, in (a), – where the initial points of the correlation are represented - and after the fine calibration, in (b). Also, in (b), the bands with a black * are the ones used in the linear regression and, those with a grey * are the bands that confirm the correlation. A logarithmic scale is used in the y-axis of graphs (a) and (b). At the bottom, in (c), is represented the residuals of the linear regression.

In Figure 4.16 is also observed that the prototype has a resolution inferior to the SPEX 1403. This was expected and can be justified by the grating's characteristics, the

imaging sensor's sensitivity being less than the required to resolve some of the close bands, as seen for example in the 576 to 580 nm region. This could be originated by the imaging sensor's lens not having a sufficient magnification factor to allow each detector's pixel to distinguish only one spectral band. Another cause can be that the Hg bands with high intensities saturate pixels, leaking the signal to the surrounding pixels and so contributing to large bands, and ultimately, to the overlap of close bands, such as the ones discussed. Nonetheless, some improvements must be done to increase resolution, such as, (i) increasing the focal length of the focusing lens on the detector system, or (ii) setting the detector further from the grating. Also, (iii) substituting the detector system used by one with higher quantum efficiency or (iv) smaller pixel's size, consequently improving the system's spectral resolution. Also, (v) improving the prototype's alignment obtained or (vi) changing the aperture size by substituting the entrance slit used will have a major implication on the resolution of the spectrometer. Moreover, (vii) kinematic mounts could be used in order to allow more precise positioning and alignment of the optical components in the setup, and consequently, a higher resolution can be achieved.

Analysing Figure 4.17, it is possible to verify that the prototype resolution is less than 3 nm, by calculating the value of FWHM of the highest band (in the 545 nm).

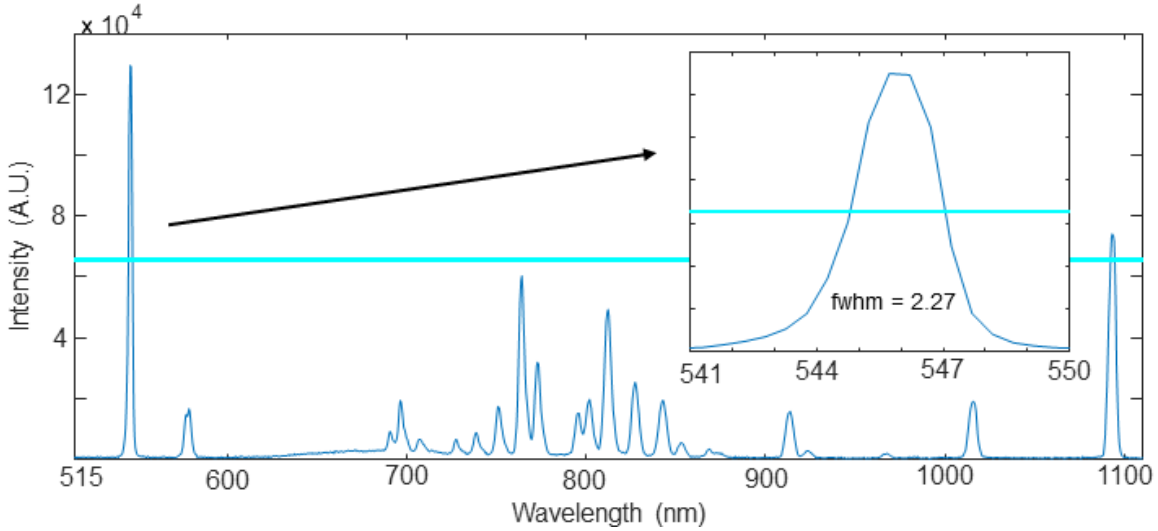

Figure 4.17 – Total Spectrum of Hg lamp after the calibration with the value of FWHM of the highest band.

This calibration is only validated to a limited spectral range (515 to 750 nm). Consequently, the resulting shift of the prototype's spectrum for longer wavelengths than 750 nm cannot be guaranteed. In order to solve this issue, a commercial reference spectrometer with a higher spectral range could be used. This strategy would allow to

increase the number of correlation points (spectral bands) and possibly, allow that the full prototype's spectrum could have correlation points.

Moreover, the prototype's field of view is large [487-1114] nm, and so, each pixel covers a 0.49 nm wavelength range, resulting in a low chromatic resolution, which means that one or more spectral bands could be detected in the same pixel, which will ultimately result in a wider band, instead of detecting narrower bands. However, adding a DMD after the grating to select a restricted region of the spectrum could solve this problem.

4.4. Complex Sample Analysis

The last test done in this project was obtaining a cyclohexane's Raman spectrum in the HWVN region. Cyclohexane has well defined bands in this region, as seen in Figure 3.8 of Chapter 3 – Materials and Methods.

Cyclohexane's significant bands in the HWVN, in wavenumbers, are [2664.4; 2852,9; 2923,8; 2938,3] cm^{-1}. Using equation 2.1, the laser's excitation wavelengths and those cyclohexane reference wavenumbers, the corresponding cyclohexane's wavelengths (nm) of interest in the HWVN are: [761.42; 772.51; 776.76; 777.64] nm for the 632.8 nm laser, [771.52; 782.96; 787.31; 788.23] nm for the laser of 640 nm, and, finally, [1317.3; 1352.6; 1365.7; 1368.4 nm] for the 976 nm laser.

To obtain this spectrum, it is important to reject light outside the HWVN region, which is in a different region for the infrared and the two red lasers. So, different filters were used: the 769/41 nm bandpass filter while using the red lasers (632.8 nm and 640 nm) and the 980 high pass filter combined with the infrared laser (976 nm).

However, since the HWVN cyclohexane Raman spectrum using the 976 nm laser is expected to be between 1317.3 nm and 1368.4 nm, and the detection system cannot detect above 1100 nm, the combination of this light source and the imaging sensor was not suitable. Hence, only the two red lasers were used.

To reduce the background noise caused by direct light reflections, two linear polarizers, with a 90º rotation relative to each other, were included in the setup, one placed after the laser and the other before the detection system. Because the sample scattered light does not have a preferable polarization direction, the second polarizer was used to reject the light directly reflected by the laser and allow the other polarization directions to pass through.

Furthermore, all the frames were collected using the previous calibration, and so, the ROI is still implemented to minimize noise. Also, this reduces the influence of "hot" pixels in the acquisitions, which is caused by the increment of the exposure time.

4.4.1. Cyclohexane

The results of the acquisitions using the 632.8 nm laser are presented below. The binning of the spectra of only 1 frame - Figure 4.18 (a) -, then, stacking using 10 frames, 1000 frames and lastly 2000 frames, to maximize the signal acquired, are shown in Figure 4.18 (b), (c) and (d) respectively. However, it is noticeable that the spectrometer cannot distinguish the weak Raman signal from noise (Figure 4.18, dark blue line).

To try to solve this issue, several strategies are used to minimize noise from the cyclohexane signal. Firstly, the dark current noise of the signal is removed (Figure 4.18 - red line). Secondly, the background noise of the signal is removed (Figure 4.18 – light blue line). The dark current noise is the inherent current that exists while no incident light is collected by the detector. Hence, it is obtained when the laser is turned off (while no sample is placed) and is the same for the two red lasers used (632.8 nm and 640 nm) (Figure 4.19 (a)). The background noise is the stray light of the system (*e.g.*, potential reflections in the optic cages, excitation laser light) and it also includes dark current noise. It is obtained by removing the sample but keeping the laser on (Figure 4.19 (b)). This noise is dependent on the laser used, but the results were not significantly different, so only the background noise obtained with the laser 632.8 nm is represented in Figure 4.19 (b).

Hence, for one frame acquisition of cyclohexane spectra (Figure 4.18 (a) and 4.20 (a)), since noise is of random nature, an average of 5 distinct frames of the respective noises is subtracted (represent in Figure 4.19 blue lines). For the remaining data with the acquisition of more frames, the final spectra result from the stacking of the cyclohexane signal subtracted by the background and dark current noises, also obtained after the stacking of the same number of frames (respectively, light blue and red lines of Figure 4.18 and 4.20 (b), (c) and (d)).

In Figures 4.18 and 4.20, the filter bandwidth region, [749 – 790] nm, where the presence of the HWVN region of cyclohexane's spectrum is expected, is highlighted by two vertical dashed black lines. Observing Figure 4.18, the bands presented in this region are as

intense as the ones seen outside of it, which indicates that the Raman signal is masked by noise (dark blue line), even when the subtraction of noise is present (light blue and red lines).

The subtraction of two values of the noise of two distinct acquisitions can lead to negative spectral points, or even the full spectrum under the zero line, which is caused if the noise in the signal is more intense than the noise registered in the first acquisition. This can be justified by the fact that noise is of random nature, and it is affected by several aspects (e.g., room temperature, ambient lighting variations, etc.). Furthermore, those negative spectral points are more likely to happen with smaller number of frames used. So, in cyclohexane spectra which intensity was below the zero line, it was subtracted the minimum of the spectra.

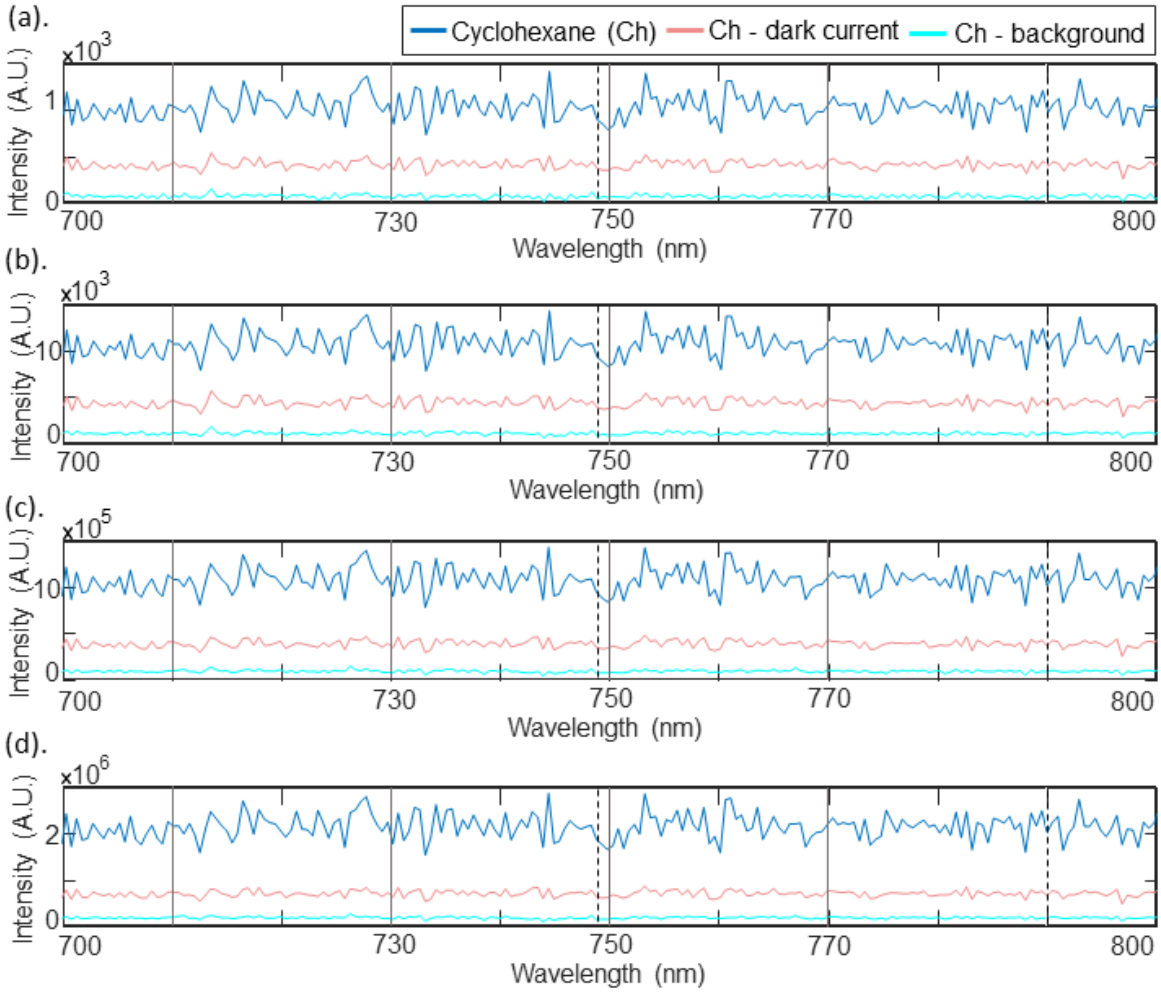

Figure 4.18 – Stacking, using laser 632.8 nm, with 1, 10, 1000, 2000 frames ((a) to (d), respectively), of cyclohexane (blue line), without dark current (red line) and background noise (light blue line).

As mentioned, Figure 4.19 represents the acquisitions of dark current (a) and background (b) noises with one frame (orange line). The average of 5 distinct frames is also computed and represented in the same figure (blue line).

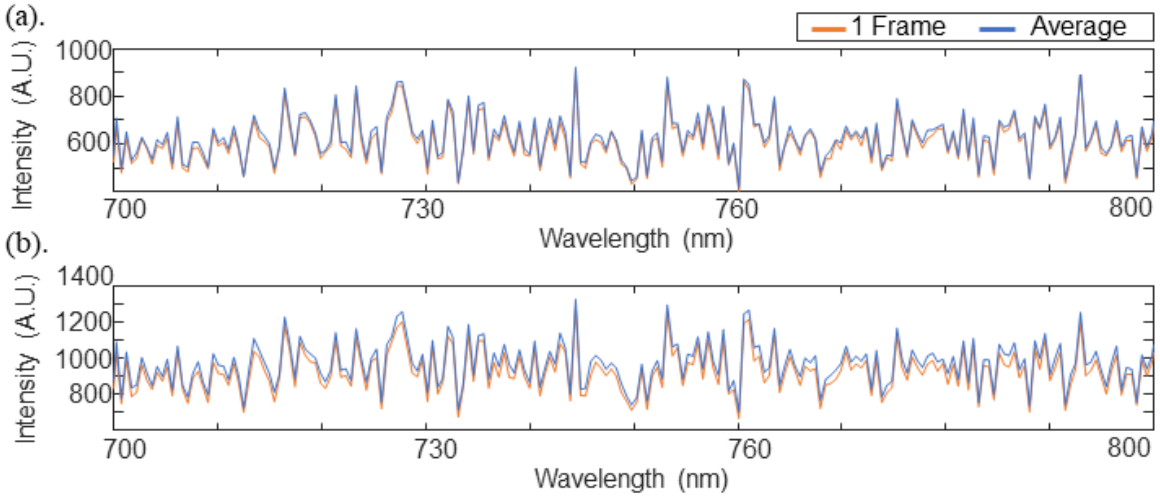

Figure 4.19 – Dark current noise (a) and background noise (b) spectra, using 632.8 nm laser of one frame (orange) and the average of five distinct frames (blue) of each noise. The same spectra of dark current noise and similar spectra of background noise were obtained with the 640 nm.

The same data processing is done for the acquisitions with the 640 nm laser. Figure 4.20 represents the stacking of the cyclohexane signal (blue line) using 640 nm laser, for 1, 10, 1000, and 2000 frames – Figure 4.20 (a), (b), (c) and (d) -, without dark current noise (red line), and without background noise (light blue line). The subtraction of the dark current noise (average of 5 frames) was the same as the subtracted array from the data acquired with the 632.8 nm laser since it is independent of the laser used (Figure 4.19 (a) blue line). The background noise subtracted is similar as the represented in Figure 4.19 (b), blue line, but substituting the laser used, in this case, 640 nm laser. The result is similar and considered not relevant to be represented.

Analysing each of the rows of both Figure 4.18 and 4.20, *i.e.*, spectra with the same number of frames, it is expected that the dark blue line spectrum without removal of noise would have higher intensity (number of counts) when compared to the red line spectrum with the removal of dark current noise. Also, since background noise includes dark current noise, it is expected that the light blue line spectrum with the removal of background noise will have an even lower intensity compared to the red line spectrum. This agrees with the results represented in Figures 4.18 and 4.20.

When the background noise is subtracted, it is expected that the baseline of the spectrum decreases, which has occurred in all spectra of Figures 4.18 and 4.20. However,

the Raman signal can still not be observed. This proves that the Raman signal SNR is too low and the designed system or some of its components were not able to detect it. Therefore, the detector should be replaced by one with higher quantum efficiency and sensitivity.

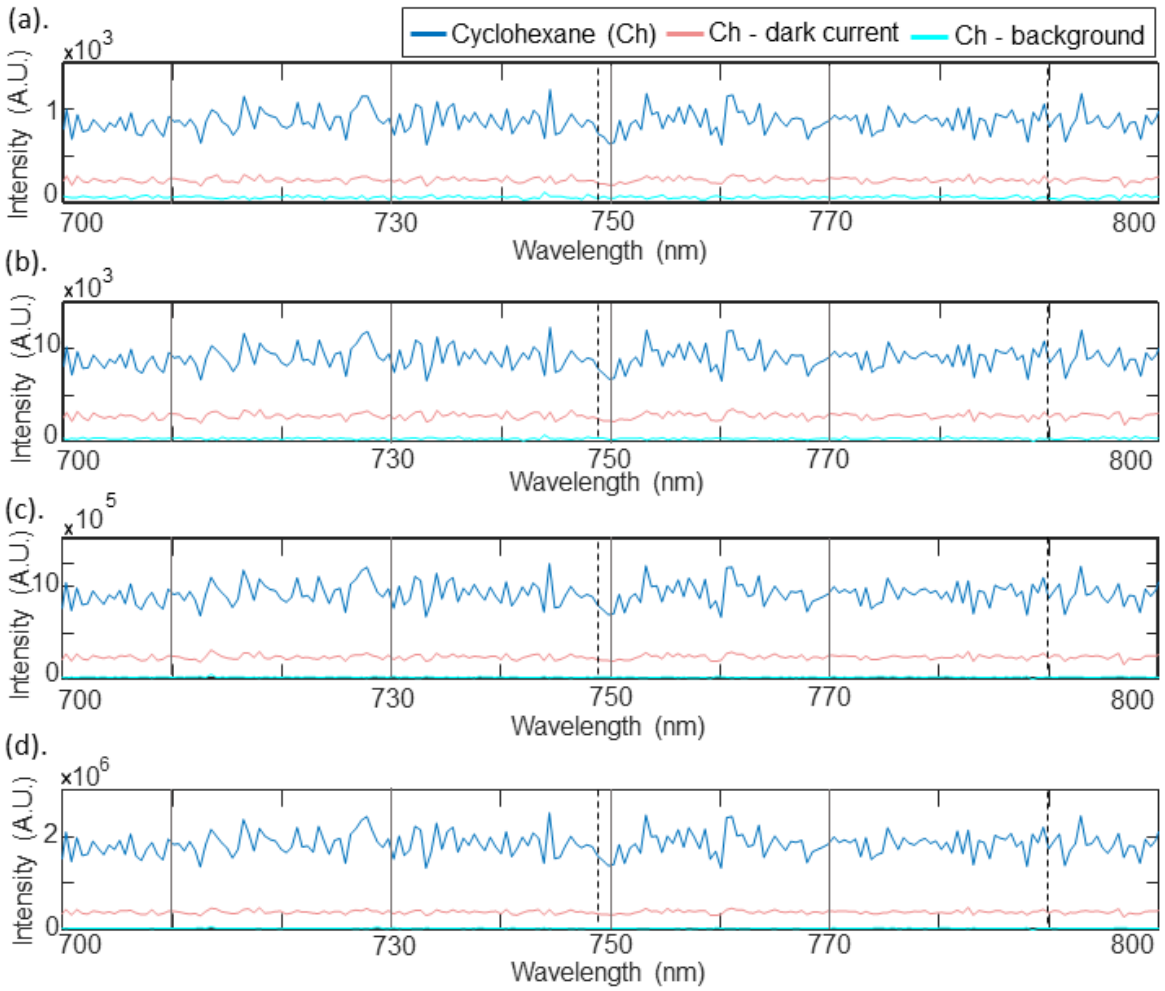

Figure 4.20 - Stacking, using laser 640 nm, with 1, 10, 1000, 2000 frames ((a) to (d), respectively), of cyclohexane (blue line) without dark current (red line) and background noise (light blue line).

Observing Figures 4.18 and 4.20, it can be concluded that the stacking method results in an increment of the intensity of the spectra, however, the noise is also amplified. Consequently, the cyclohexane Raman spectra, being a signal of low intensity, are not detected using the two red lasers. Furthermore, when the number of frames was increased to 5000, the spectrometer was still not able to distinguish the Raman spectrum of cyclohexane from background noise.

5. CONCLUSIONS AND FUTURE WORK

In chapter 5, the work developed in this dissertation project will be resumed, from the starting point to the work carried out until its completion. The main conclusions will be reviewed, in 5.1, and future developments will be proposed for the continuation of the project, in 5.2.

5.1. Final Remarks

The main goal of this dissertation was to develop an initial Raman spectrometer operating in the HWVN region of the spectrum with low tolerance to variations of position, and evaluation of its performance. To do so, first, the choice of the components with mathematical validation was completed, then the simulation of the setup was performed. Afterwards, the prototype was assembled in the optical table with the elaboration of alignment protocols and calibration procedures, and finally, as the ultimate goal, detection of HWVN Raman signals was tested.

Regarding the choice of components and respective simulation, it was concluded that, although the theoretical mathematical calculations for the lenses chosen were according to the requirements for melanoma applications, during the simulation, the spot size obtained was two orders of magnitude larger than the obtained theoretically. This can be justified by the software not having all the components used in the real setting. However, this software is still in development, so in the future, these issues could be solved. Nevertheless, the expanded beam values of simulation and physical setup were in accordance with the theoretical matrixial method.

It was also concluded that the main filter, 980 nm high-pass filter, was inefficient to reject laser light when implemented at an angle of 45º. Consequently, the setup assembled has a transmission configuration (0º), which is not suitable for *in vivo* biomedical applications.

Concerning the prototype setup, several mechanical parts were designed to minimize alignment variations. It was concluded that these 3D objects, *i.e.,* the sample holder, the camera fixation 3D parts, as well as the laser's supports, help to maintain the

position of the prototype components. In particular, the sample holder created allowed to place several sample formats, without the need for moving the optical components.

Regarding calibration procedures, both coarse and fine calibrations obtained a high value of R^2 (0.9993 and 1, respectively), which means that the correlation between the regression data was good. The coarse calibration resulted in a well-defined delimitation of the area visualized by the detector system, converting successfully the x-axis from pixel to wavelength units. The fine calibration, which compared the spectrum of the same material, Hg lamp, acquired in the prototype and a calibrated spectrometer, SPEX 1403, despite having a high R^2 value, had some issues: some bands in the prototype spectrum were missing. However, other bands after the calibration have correctly matched with the reference spectrum, for instance, all the bands used in the regression, and moreover other two bands, not included in the correlation. A possible explanation for the issue is a misalignment between the camera and the diffraction grating. Furthermore, this calibration is only valid in a small spectral range, [515-750] nm, giving no information about the rest of the prototype's wavelength range. Also, the prototype's resolution was inferior to the SPEX 1403, which can be justified by the imaging sensor's sensitivity being less than the required to resolve some of the close bands. This could be originated by the imaging sensor's lens not having a sufficient magnification factor to allow each detector's pixel to detect only one spectral band or insufficient distance between the grating and the detector.

Concerning the ultimate goal of this dissertation, the detection system available could not detect signals above 1100 nm, so the main laser was substituted by red lasers, making the HWVN region of the Raman spectrum detectable by the imaging sensor. Therefore, acquisitions using 1, 10, 1000 and 2000 frames (stacking) of cyclohexane Raman spectrum in the HWVN region, with background and dark current noise removal, were obtained with the prototype. However, the Raman signal was not successfully differentiated from noise with any of the lasers and/or the number of frames used. This can be justified by the low efficiency of the detector used. It was also concluded that the stacking method results in an increment of the intensity of the spectra, however, the noise is also amplified. Consequently, the Raman signal, due to having low intensity, was not detected even with 5000 frames' stacking.

In conclusion, despite the main goal of detecting Raman signal not being achieved, the prototype has effectively acquired spectra of several lamps, obtaining a

spectral resolution of less than 3 nm using the Hg lamp and has a field of view from 487 to 1114 nm. So, this leads us to believe that by substituting the detection system used with a more sensitive one, the prototype will achieve the expected results.

5.2. Future Work

The main goal of this project was to build a Raman Compressive Spectrometer that detects signals in the HWVN region of pigmented lesions, avoiding tissue autofluorescence and providing a fast, non-invasive and easy to perform diagnosis of early melanoma lesions. To accomplish this goal, in the continuity of this project, some improvements and alterations must be implemented to the initial Raman spectrometer developed in this dissertation:

1. Changing the configuration of the spectrometer from the transmission (0º) to reflective (90º) geometry in order to apply this technology to *in vivo* biological samples. To do so, a dichroic filter with high OD and that could effectively reject laser stray-light placed at an angle of 45º is needed. In this manner, the optical configuration would be simple and easy to reproduce, as already simulated in *3DOptix* software, presented in Appendix D.
2. Also, an InGaAs detector should replace the one available to use in this dissertation project. This is of great importance since the region of interest to distinguish melanoma from BML is between 1300 to 1550 nm of the HWVN spectral region, which is only detected by this type of detector.
3. Finally, a DMD must be added to select the specific wavelength of interest and to reduce the measurements acquisition time, making this technology suitable for clinical setting use.

REFERENCES

[1] W. H. Organization, 'GLOBOCAN 2020: Melanoma of skin Incidence and Mortality Statistics Worldwide and by Regions', 2020. https://gco.iarc.fr/today/home (accessed Apr. 08, 2021).

[2] M. Maranduca *et al.*, 'Synthesis and physiological implications of melanic pigments (Review)', *Oncol. Lett.*, vol. 17, no. 5, pp. 4183–4187, Feb. 2019, doi: 10.3892/ol.2019.10071.

[3] J.-F. Hamel *et al.*, 'A systematic review examining factors influencing health related quality of life among melanoma cancer survivors', *Eur. J. Cancer*, vol. 69, pp. 189–198, Dec. 2016, doi: 10.1016/j.ejca.2016.10.008.

[4] H. W. Higgins, K. C. Lee, A. Galan, and D. J. Leffell, 'Melanoma in situ Part I. Epidemiology, screening, and clinical features H.', *J. Am. Acad. Dermatol.*, vol. 73, no. 2, pp. 181–190, Aug. 2015, doi: 10.1016/j.jaad.2015.04.014.

[5] S. M. Swetter *et al.*, 'Guidelines of care for the management of primary cutaneous melanoma', *J. Am. Acad. Dermatol.*, vol. 80, no. 1, pp. 208–250, Jan. 2019, doi: 10.1016/j.jaad.2018.08.055.

[6] M. Patnana, J. E. Gershenwald, W.-J. Hwu, and C. S. Ng, 'Melanoma', in *Oncologic Imaging: A Multidisciplinary Approach*, Elsevier, 2012, pp. 633–652.

[7] Y. Zhang *et al.*, 'Assessment of Raman Spectroscopy for Reducing Unnecessary Biopsies for Melanoma Screening', *Molecules*, vol. 25, no. 12, p. 2852, Jun. 2020, doi: 10.3390/molecules25122852.

[8] A. M. Glazer, D. S. Rigel, R. R. Winkelmann, and A. S. Farberg, 'Clinical Diagnosis of Skin Cancer', *Dermatol. Clin.*, vol. 35, no. 4, pp. 409–416, Oct. 2017, doi: 10.1016/j.det.2017.06.001.

[9] A. N. MacLellan *et al.*, 'The use of noninvasive imaging techniques in the diagnosis of melanoma: a prospective diagnostic accuracy study', *J. Am. Acad. Dermatol.*, vol. 85, no. 2, pp. 353–359, Aug. 2021, doi: 10.1016/j.jaad.2020.04.019.

[10] S. C. Chen, D. M. Bravata, E. Weil, and I. Olkin, 'A Comparison of Dermatologists' and Primary Care Physicians' Accuracy in Diagnosing Melanoma', *Arch. Dermatol.*, vol. 137, no. 12, pp. 1627–1634, Dec. 2001, doi: 10.1001/archderm.137.12.1627.

[11] P. Carli, P. Nardini, E. Crocetti, V. De Giorgi, and B. Giannotti, 'Frequency and characteristics of melanomas missed at a pigmented lesion clinic: a registry-based study', *Melanoma Res.*, vol. 14, no. 5, pp. 403–407, Oct. 2004, doi: 10.1097/00008390-200410000-00011.

[12] R. Aldridge, L. Naysmith, E. Ooi, C. Murray, and J. Rees, 'The Importance of a Full Clinical Examination: Assessment of Index Lesions Referred to a Skin Cancer Clinic Without a Total Body Skin Examination Would Miss One in Three Melanomas', *Acta Derm. Venereol.*, vol. 93, no. 6, pp. 689–692, 2013, doi: 10.2340/00015555-1625.

[13] P. Guitera *et al.*, 'Dermoscopy and in vivo confocal microscopy are complementary techniques for diagnosis of difficult amelanotic and light-coloured skin lesions', *Br. J. Dermatol.*, vol. 175, no. 6, pp. 1311–1319, Dec. 2016, doi: 10.1111/bjd.14749.

[14] Y. Zhang *et al.*, 'Adaptive compressed sensing of Raman spectroscopic profiling data for discriminative tasks', *Talanta*, vol. 211, no. December 2019, p. 120681, May

2020, doi: 10.1016/j.talanta.2019.120681.
[15] I. P. Santos *et al.*, 'Improving clinical diagnosis of early-stage cutaneous melanoma based on Raman spectroscopy', *Br. J. Cancer*, vol. 119, no. 11, pp. 1339–1346, Nov. 2018, doi: 10.1038/s41416-018-0257-9.
[16] D. Wei, S. Chen, and Q. Liu, 'Review of Fluorescence Suppression Techniques in Raman Spectroscopy', *Appl. Spectrosc. Rev.*, vol. 50, no. 5, pp. 387–406, May 2015, doi: 10.1080/05704928.2014.999936.
[17] E. B. Hanlon *et al.*, 'Prospects for in vivo Raman spectroscopy', *Phys. Med. Biol.*, vol. 45, no. 2, pp. R1–R59, Feb. 2000, doi: 10.1088/0031-9155/45/2/201.
[18] S. Tfaili, G. Josse, C. Gobinet, J.-F. Angiboust, M. Manfait, and O. Piot, 'Shedding light on the laser wavelength effect in Raman analysis of skin epidermises', *Analyst*, vol. 137, no. 18, pp. 4241–4246, 2012, doi: 10.1039/c2an16115j.
[19] E. Cordero, F. Korinth, C. Stiebing, C. Krafft, I. Schie, and J. Popp, 'Evaluation of Shifted Excitation Raman Difference Spectroscopy and Comparison to Computational Background Correction Methods Applied to Biochemical Raman Spectra', *Sensors*, vol. 17, no. 8, p. 1724, Jul. 2017, doi: 10.3390/s17081724.
[20] I. P. Santos, P. J. Caspers, T. Bakker Schut, R. van Doorn, S. Koljenović, and G. J. Puppels, 'Implementation of a novel low-noise InGaAs detector enabling rapid near-infrared multichannel Raman spectroscopy of pigmented biological samples', *J. Raman Spectrosc.*, vol. 46, no. 7, pp. 652–660, Jul. 2015, doi: 10.1002/jrs.4714.
[21] A. Nijssen *et al.*, 'Discriminating basal cell carcinoma from perilesional skin using high wave-number Raman spectroscopy', *J. Biomed. Opt.*, vol. 12, no. 3, p. 034004, 2007, doi: 10.1117/1.2750287.
[22] C. A. Patil, I. J. Pence, C. A. Lieber, and A. Mahadevan-Jansen, '1064 nm dispersive Raman spectroscopy of tissues with strong near-infrared autofluorescence', *Opt. Lett.*, vol. 39, no. 2, pp. 303–306, Jan. 2014, doi: 10.1364/OL.39.000303.
[23] J. M. Cameron *et al.*, 'Vibrational spectroscopic analysis and quantification of proteins in human blood plasma and serum', in *Vibrational Spectroscopy in Protein Research*, 1st Editio., O. Yukihiro, M. Baransk, I. K. Lednev, and B. Wood, Eds. Elsevier, 2020, pp. 269–314.
[24] B. Sturm, F. Soldevila, E. Tajahuerce, S. Gigan, H. Rigneault, and H. B. de Aguiar, 'High-Sensitivity High-Speed Compressive Spectrometer for Raman Imaging', *ACS Photonics*, vol. 6, no. 6, pp. 1409–1415, Jun. 2019, doi: 10.1021/acsphotonics.8b01643.
[25] P. G. Vaz, D. Amaral, L. F. Requicha Ferreira, M. Morgado, and J. Cardoso, 'Image quality of compressive single-pixel imaging using different Hadamard orderings', *Opt. Express*, vol. 28, no. 8, pp. 11666–11681, Apr. 2020, doi: 10.1364/OE.387612.
[26] I. P. Santos *et al.*, 'Raman Spectroscopic Characterization of Melanoma and Benign Melanocytic Lesions Suspected of Melanoma Using High-Wavenumber Raman Spectroscopy', *Anal. Chem.*, vol. 88, no. 15, pp. 7683–7688, Aug. 2016, doi: 10.1021/acs.analchem.6b01592.
[27] S. Nafisi and H. I. Maibach, 'Skin penetration of nanoparticles', in *Emerging Nanotechnologies in Immunology*, Elsevier, 2018, pp. 47–88.
[28] J. A. McGrath and J. Uitto, 'Anatomy and Organization of Human Skin', in *Rook's Textbook of Dermatology*, 7th editio., vol. 1, C. Burns, Tony; Breathnach, Stephen, Cox, Neil; Griffiths, Ed. Oxford, UK: Wiley-Blackwell, 2010, pp. 1–53.
[29] M. Venus, J. Waterman, and I. McNab, 'Basic physiology of the skin', *Surg.*, vol. 28, no. 10, pp. 469–472, Oct. 2010, doi: 10.1016/j.mpsur.2010.07.011.

[30] T. Merghoub, D. Polsky, and A. N. Houghton, 'Molecular Biology of Melanoma', in *The Molecular Basis of Cancer*, Elsevier, 2008, pp. 463–470.
[31] G. Bosserhoff, Anja (Molecular Pathology, Institute of Pathololgy Regensburg, *Melanoma Development*, 1st ed. Vienna: Springer Vienna, 2011.
[32] A. Ndikumana MD, Robyn; Osmond, 'Melanoma in situ of the skin'. https://www.mypathologyreport.ca/melanoma-in-situ/ (accessed Aug. 19, 2021).
[33] K. V. Viola *et al.*, 'National utilization patterns of Mohs micrographic surgery for invasive melanoma and melanoma in situ', *J. Am. Acad. Dermatol.*, vol. 72, no. 6, pp. 1060–1065, Jun. 2015, doi: 10.1016/j.jaad.2015.02.1122.
[34] G. Champsas and O. Papadopoulos, 'The Role of the Sentinel Lymph Node Biopsy in the Treatment of Nonmelanoma Skin Cancer and Cutaneous Melanoma', in *Non-Melanoma Skin Cancer and Cutaneous Melanoma*, Cham: Springer International Publishing, 2020, pp. 647–704.
[35] H. W. Higgins, K. C. Lee, A. Galan, and D. J. Leffell, 'Melanoma in situ Part II. Histopathology, treatment, and clinical management H.', *J. Am. Acad. Dermatol.*, vol. 73, no. 2, pp. 193–203, Aug. 2015, doi: 10.1016/j.jaad.2015.03.057.
[36] J. E. Gershenwald *et al.*, 'Melanoma staging: Evidence-based changes in the American Joint Committee on Cancer eighth edition cancer staging manual', *CA. Cancer J. Clin.*, vol. 67, no. 6, pp. 472–492, Nov. 2017, doi: 10.3322/caac.21409.
[37] A. Alqathama, 'BRAF in malignant melanoma progression and metastasis: potentials and challenges.', *Am. J. Cancer Res.*, vol. 10, no. 4, pp. 1103–1114, 2020, [Online]. Available: http://www.ncbi.nlm.nih.gov/pubmed/32368388%0Ahttp://www.pubmedcentral.nih.gov/articlerender.fcgi?artid=PMC7191094.
[38] S. W. Menzies *et al.*, 'The Performance of SolarScan: An Automated Dermoscopy Image Analysis Instrument for the Diagnosis of Primary Melanoma', *Arch. Dermatol.*, vol. 141, no. 11, pp. 1388–1396, Nov. 2005, doi: 10.1001/archderm.141.11.1388.
[39] J. Zhao, H. Lui, S. Kalia, and H. Zeng, 'Real-time Raman spectroscopy for automatic in vivo skin cancer detection: an independent validation', *Anal. Bioanal. Chem.*, vol. 407, no. 27, pp. 8373–8379, Nov. 2015, doi: 10.1007/s00216-015-8914-9.
[40] A. Blundo, A. Cignoni, T. Banfi, and G. Ciuti, 'Comparative Analysis of Diagnostic Techniques for Melanoma Detection: A Systematic Review of Diagnostic Test Accuracy Studies and Meta-Analysis', *Front. Med.*, vol. 8, no. 637069, pp. 1–22, Apr. 2021, doi: 10.3389/fmed.2021.637069.
[41] P. Guitera, G. Pellacani, C. Longo, S. Seidenari, M. Avramidis, and S. W. Menzies, 'In Vivo Reflectance Confocal Microscopy Enhances Secondary Evaluation of Melanocytic Lesions', *J. Invest. Dermatol.*, vol. 129, no. 1, pp. 131–138, Jan. 2009, doi: 10.1038/jid.2008.193.
[42] E. Dimitrow *et al.*, 'Sensitivity and Specificity of Multiphoton Laser Tomography for In Vivo and Ex Vivo Diagnosis of Malignant Melanoma', *J. Invest. Dermatol.*, vol. 129, no. 7, pp. 1752–1758, Jul. 2009, doi: 10.1038/jid.2008.439.
[43] T. Gambichler *et al.*, 'A multicentre pilot study investigating high-definition optical coherence tomography in the differentiation of cutaneous melanoma and melanocytic naevi', *J. Eur. Acad. Dermatology Venereol.*, vol. 29, no. 3, pp. 537–541, Mar. 2015, doi: 10.1111/jdv.12621.
[44] E. Borisova, E. Pavlova, T. Kundurjiev, P. Troyanova, T. Genova, and L. Avramov, 'Light-induced autofluorescence and diffuse reflectance spectroscopy in clinical

diagnosis of skin cancer', in *Biophotonics: Photonic Solutions for Better Health Care IV*, May 2014, vol. 9129, p. 91291O, doi: 10.1117/12.2051406.

[45] S. B. Cartaxo *et al.*, 'FT-Raman spectroscopy for the differentiation between cutaneous melanoma and pigmented nevus', *Acta Cir. Bras.*, vol. 25, no. 4, pp. 351–356, Aug. 2010, doi: 10.1590/S0102-86502010000400010.

[46] A. Garcia-Uribe, E. B. Smith, J. Zou, M. Duvic, V. Prieto, and L. V. Wang, 'In-vivo characterization of optical properties of pigmented skin lesions including melanoma using oblique incidence diffuse reflectance spectrometry', *J. Biomed. Opt.*, vol. 16, no. 2, p. 020501, 2011, doi: 10.1117/1.3536509.

[47] N. Rajaram, J. S. Reichenberg, M. R. Migden, T. H. Nguyen, and J. W. Tunnell, 'Pilot clinical study for quantitative spectral diagnosis of non-melanoma skin cancer', *Lasers Surg. Med.*, vol. 42, no. 10, pp. 876–887, Dec. 2010, doi: 10.1002/lsm.21009.

[48] P. Mohr *et al.*, 'Electrical impedance spectroscopy as a potential adjunct diagnostic tool for cutaneous melanoma', *Ski. Res. Technol.*, vol. 19, no. 2, pp. 75–83, May 2013, doi: 10.1111/srt.12008.

[49] G. H. Litchman, J. W. Marson, R. M. Svoboda, and D. S. Rigel, 'Integrating Electrical Impedance Spectroscopy into Clinical Decisions for Pigmented Skin Lesions Improves Diagnostic Accuracy: A Multitiered Study', *Ski. J. Cutan. Med.*, vol. 4, no. 5, pp. 424–430, Aug. 2020, doi: 10.25251/skin.4.5.5.

[50] L. Rocha *et al.*, 'Analysis of an electrical impedance spectroscopy system in short-term digital dermoscopy imaging of melanocytic lesions', *Br. J. Dermatol.*, vol. 177, no. 5, pp. 1432–1438, Nov. 2017, doi: 10.1111/bjd.15595.

[51] P. Gerami, J. P. Alsobrook, T. J. Palmer, and H. S. Robin, 'Development of a novel noninvasive adhesive patch test for the evaluation of pigmented lesions of the skin', *J. Am. Acad. Dermatol.*, vol. 71, no. 2, pp. 237–244, Aug. 2014, doi: 10.1016/j.jaad.2014.04.042.

[52] C. Magalhaes, R. Vardasca, M. Rebelo, R. Valenca-Filipe, M. Ribeiro, and J. Mendes, 'Distinguishing melanocytic nevi from melanomas using static and dynamic infrared thermal imaging', *J. Eur. Acad. Dermatology Venereol.*, vol. 33, no. 9, pp. 1700–1705, Sep. 2019, doi: 10.1111/jdv.15611.

[53] E. Pérez, O. Reyes, and S. Ventura, 'Convolutional neural networks for the automatic diagnosis of melanoma: An extensive experimental study', *Med. Image Anal.*, vol. 67, p. 101858, Jan. 2021, doi: 10.1016/j.media.2020.101858.

[54] M. Phillips *et al.*, 'Assessment of Accuracy of an Artificial Intelligence Algorithm to Detect Melanoma in Images of Skin Lesions', *JAMA Netw. Open*, vol. 2, no. 10, p. e1913436, Oct. 2019, doi: 10.1001/jamanetworkopen.2019.13436.

[55] M. Janda *et al.*, 'Accuracy of mobile digital teledermoscopy for skin self-examinations in adults at high risk of skin cancer: an open-label, randomised controlled trial', *Lancet Digit. Heal.*, vol. 2, no. 3, pp. e129–e137, Mar. 2020, doi: 10.1016/S2589-7500(20)30001-7.

[56] J. K. Robinson and B. Jansen, 'Caring for Melanoma Survivors with Self-Detected Concerning Moles During COVID-19 Restricted Physician Access: a Cohort Study', *Ski. J. Cutan. Med.*, vol. 4, no. 3, pp. 248–251, May 2020, doi: 10.25251/skin.4.3.5.

[57] F. M. Walter and J. D. Emery, 'Further evaluation is required for smartphone-aided diagnosis of skin cancer', *Lancet Digit. Heal.*, vol. 2, no. 3, pp. e104–e105, Mar. 2020, doi: 10.1016/S2589-7500(20)30021-2.

[58] T. Gambichler *et al.*, 'Characterization of benign and malignant melanocytic skin lesions using optical coherence tomography in vivo', *J. Am. Acad. Dermatol.*, vol. 57,

no. 4, pp. 629–637, Oct. 2007, doi: 10.1016/j.jaad.2007.05.029.
[59] X. Meng *et al.*, 'Non-invasive optical methods for melanoma diagnosis', *Photodiagnosis Photodyn. Ther.*, vol. 34, p. 102266, Jun. 2021, doi: 10.1016/j.pdpdt.2021.102266.
[60] J. Zhao, H. Zeng, S. Kalia, and H. Lui, 'Using Raman Spectroscopy to Detect and Diagnose Skin Cancer In Vivo', *Dermatol. Clin.*, vol. 35, no. 4, pp. 495–504, Oct. 2017, doi: 10.1016/j.det.2017.06.010.
[61] M. Gniadecka, H. C. Wulf, O. F. Nielsen, D. H. Christensen, and J. Hercogova, 'Distinctive Molecular Abnormalities in Benign and Malignant Skin Lesions: Studies by Raman Spectroscopy', *Photochem. Photobiol.*, vol. 66, no. 4, pp. 418–423, Oct. 1997, doi: 10.1111/j.1751-1097.1997.tb03167.x.
[62] L. Lim *et al.*, 'Clinical study of noninvasive in vivo melanoma and nonmelanoma skin cancers using multimodal spectral diagnosis', *J. Biomed. Opt.*, vol. 19, no. 11, p. 117003, Nov. 2014, doi: 10.1117/1.JBO.19.11.117003.
[63] Y. A. Khristoforova *et al.*, 'Portable spectroscopic system for in vivo skin neoplasms diagnostics by Raman and autofluorescence analysis', *J. Biophotonics*, vol. 12, no. 4, p. e201800400, Apr. 2019, doi: 10.1002/jbio.201800400.
[64] P. J. Larkin, 'Basic Principles', in *Infrared and Raman Spectroscopy*, 2nd editio., vol. 34, Elsevier, 2018, pp. 7–28.
[65] S. K. Paidi, R. Pandey, and I. Barman, 'Emerging trends in biomedical imaging and disease diagnosis using Raman spectroscopy', in *Molecular and Laser Spectroscopy*, Elsevier, 2020, pp. 623–652.
[66] Y. K. Lin, H. Y. Leong, T. C. Ling, D.-Q. Lin, and S.-J. Yao, 'Raman spectroscopy as process analytical tool in downstream processing of biotechnology', *Chinese J. Chem. Eng.*, vol. 30, pp. 204–211, Feb. 2021, doi: 10.1016/j.cjche.2020.12.008.
[67] B. Yu, M. Ge, P. Li, Q. Xie, and L. Yang, 'Development of surface-enhanced Raman spectroscopy application for determination of illicit drugs: Towards a practical sensor', *Talanta*, vol. 191, pp. 1–10, Jan. 2019, doi: 10.1016/j.talanta.2018.08.032.
[68] S. R. Khandasammy *et al.*, 'Bloodstains, paintings, and drugs: Raman spectroscopy applications in forensic science', *Forensic Chem.*, vol. 8, pp. 111–133, May 2018, doi: 10.1016/j.forc.2018.02.002.
[69] M. Gao, S. Liu, J. Chen, K. C. Gordon, F. Tian, and C. M. McGoverin, 'Potential of Raman spectroscopy in facilitating pharmaceutical formulations development – An AI perspective', *Int. J. Pharm.*, vol. 597, no. 120334, pp. 1–12, Mar. 2021, doi: 10.1016/j.ijpharm.2021.120334.
[70] S. Holler, E. Mansley, C. Mazzeo, M. Donovan, M. Sobrero, and B. Miles, 'Raman Spectroscopy of Head and Neck Cancer: Separation of Malignant and Healthy Tissue Using Signatures Outside the "Fingerprint" Region', *Biosensors*, vol. 7, no. 4, p. 20, May 2017, doi: 10.3390/bios7020020.
[71] H. Li, T. Ning, F. Yu, Y. Chen, B. Zhang, and S. Wang, 'Raman Microspectroscopic Investigation and Classification of Breast Cancer Pathological Characteristics', *Molecules*, vol. 26, no. 4, pp. 921:1–11, Feb. 2021, doi: 10.3390/molecules26040921.
[72] A. Sinica, K. Brožáková, T. Brůha, and J. Votruba, 'Raman spectroscopic discrimination of normal and cancerous lung tissues', *Spectrochim. Acta Part A Mol. Biomol. Spectrosc.*, vol. 219, pp. 257–266, Aug. 2019, doi: 10.1016/j.saa.2019.04.055.
[73] M. Bahreini, A. Hosseinzadegan, A. Rashidi, S. R. Miri, H. R. Mirzaei, and P. Hajian, 'A Raman-based serum constituents' analysis for gastric cancer diagnosis: In vitro

study', *Talanta*, vol. 204, pp. 826–832, Nov. 2019, doi: 10.1016/j.talanta.2019.06.068.
[74] M. Kirsch, G. Schackert, R. Salzer, and C. Krafft, 'Raman spectroscopic imaging for in vivo detection of cerebral brain metastases', *Anal. Bioanal. Chem.*, vol. 398, no. 4, pp. 1707–1713, Oct. 2010, doi: 10.1007/s00216-010-4116-7.
[75] E. Ryzhikova *et al.*, 'Raman spectroscopy and machine learning for biomedical applications: Alzheimer's disease diagnosis based on the analysis of cerebrospinal fluid', *Spectrochim. Acta Part A Mol. Biomol. Spectrosc.*, vol. 248, no. 119188, pp. 1386–1425, Mar. 2021, doi: 10.1016/j.saa.2020.119188.
[76] K. Niciński *et al.*, 'Detection of circulating tumor cells in blood by shell-isolated nanoparticle – enhanced Raman spectroscopy (SHINERS) in microfluidic device', *Sci. Rep.*, vol. 9, no. 1, p. 9267, Dec. 2019, doi: 10.1038/s41598-019-45629-7.
[77] Y. G. Chung, Q. Tu, D. Cao, S. Harada, H. J. Eisen, and C. Chang, 'Raman Spectroscopy Detects Cardiac Allograft Rejection with Molecular Specificity', *Clin. Transl. Sci.*, vol. 2, no. 3, pp. 206–210, Jun. 2009, doi: 10.1111/j.1752-8062.2009.00106.x.
[78] B. N. Zamora-Mendoza *et al.*, 'Surface-enhanced raman spectroscopy: A non invasive alternative procedure for early detection in childhood asthma biomarkers in saliva', *Photodiagnosis Photodyn. Ther.*, vol. 27, pp. 85–91, Sep. 2019, doi: 10.1016/j.pdpdt.2019.05.009.
[79] C. V. RAMAN and K. S. KRISHNAN, 'A New Type of Secondary Radiation', *Nature*, vol. 121, no. 3048, pp. 501–502, Mar. 1928, doi: 10.1038/121501c0.
[80] Q. Tu and C. Chang, 'Diagnostic applications of Raman spectroscopy', *Nanomedicine Nanotechnology, Biol. Med.*, vol. 8, no. 5, pp. 545–558, Jul. 2012, doi: 10.1016/j.nano.2011.09.013.
[81] G. W. Auner *et al.*, 'Applications of Raman spectroscopy in cancer diagnosis', *Cancer Metastasis Rev.*, vol. 37, no. 4, pp. 691–717, Dec. 2018, doi: 10.1007/s10555-018-9770-9.
[82] H. Mitsutake, R. Poppi, and M. Breitkreitz, 'Raman Imaging Spectroscopy: History, Fundamentals and Current Scenario of the Technique', *J. Braz. Chem. Soc.*, vol. 30, no. 11, pp. 2243–2258, 2019, doi: 10.21577/0103-5053.20190116.
[83] M. M. Mariani and V. Deckert, 'Raman Spectroscopy: Principles, Bene.ts, and Applications', in *Methods in Physical Chemistry*, vol. 1, Weinheim, Germany: Wiley-VCH Verlag GmbH & Co. KGaA, 2012, pp. 419–444.
[84] E. Brauchle and K. Schenke-Layland, 'Raman spectroscopy in biomedicine – non-invasive in vitro analysis of cells and extracellular matrix components in tissues', *Biotechnol. J.*, vol. 8, no. 3, pp. 288–297, Mar. 2013, doi: 10.1002/biot.201200163.
[85] S. Pahlow *et al.*, 'Application of Vibrational Spectroscopy and Imaging to Point-of-Care Medicine: A Review', *Appl. Spectrosc.*, vol. 72, no. SI, pp. 52–84, Sep. 2018, doi: 10.1177/0003702818791939.
[86] X. Feng *et al.*, 'Raman biophysical markers in skin cancer diagnosis', *J. Biomed. Opt.*, vol. 23, no. 05, p. 57002, May 2018, doi: 10.1117/1.JBO.23.5.057002.
[87] H. Schulz, 'Spectroscopic Technique: Raman Spectroscopy', in *Modern Techniques for Food Authentication*, Elsevier, 2018, pp. 139–191.
[88] J. Zhang, Y. Fan, Y. Song, and J. Xu, 'Accuracy of Raman spectroscopy for differentiating skin cancer from normal tissue', *Medicine (Baltimore).*, vol. 97, no. 34, p. e12022, Aug. 2018, doi: 10.1097/MD.0000000000012022.
[89] N. Tarcea *et al.*, 'UV Raman spectroscopy—A technique for biological and

mineralogical in situ planetary studies', *Spectrochim. Acta Part A Mol. Biomol. Spectrosc.*, vol. 68, no. 4, pp. 1029–1035, Dec. 2007, doi: 10.1016/j.saa.2007.06.051.
[90] S. Koljenović *et al.*, 'Tissue characterization using high wave number Raman spectroscopy', *J. Biomed. Opt.*, vol. 10, no. 3, p. 031116, 2005, doi: 10.1117/1.1922307.
[91] M. Monici, 'Cell and tissue autofluorescence research and diagnostic applications', in *Biotechnology Annual Review*, vol. 11, no. SUPPL., Elsevier, 2005, pp. 227–256.
[92] M. Sharma, E. Marple, J. Reichenberg, and J. W. Tunnell, 'Design and characterization of a novel multimodal fiber-optic probe and spectroscopy system for skin cancer applications', *Rev. Sci. Instrum.*, vol. 85, no. 8, pp. 083101–1:10, Aug. 2014, doi: 10.1063/1.4890199.
[93] C. A. Lieber and A. Mahadevan-Jansen, 'Automated Method for Subtraction of Fluorescence from Biological Raman Spectra', *Appl. Spectrosc.*, vol. 57, no. 11, pp. 1363–1367, Nov. 2003, doi: 10.1366/000370203322554518.
[94] J. Zhao, H. Lui, D. I. McLean, and H. Zeng, 'Automated Autofluorescence Background Subtraction Algorithm for Biomedical Raman Spectroscopy', *Appl. Spectrosc.*, vol. 61, no. 11, pp. 1225–1232, Nov. 2007, doi: 10.1366/000370207782597003.
[95] M. Chi *et al.*, 'An Improved Background-Correction Algorithm for Raman Spectroscopy Based on the Wavelet Transform', *Appl. Spectrosc.*, vol. 73, no. 1, pp. 78–87, Nov. 2019, doi: 10.1177/0003702818805116.
[96] C. M. Galloway, E. C. Le Ru, and P. G. Etchegoin, 'An Iterative Algorithm for Background Removal in Spectroscopy by Wavelet Transforms', *Appl. Spectrosc.*, vol. 63, no. 12, pp. 1370–1376, Dec. 2009, doi: 10.1366/000370209790108905.
[97] P. A. Mosier-Boss, S. H. Lieberman, and R. Newbery, 'Fluorescence Rejection in Raman Spectroscopy by Shifted-Spectra, Edge Detection, and FFT Filtering Techniques', *Appl. Spectrosc.*, vol. 49, no. 5, pp. 630–638, May 1995, doi: 10.1366/0003702953964039.
[98] Z.-M. Zhang *et al.*, 'An intelligent background-correction algorithm for highly fluorescent samples in Raman spectroscopy', *J. Raman Spectrosc.*, vol. 41, no. 6, pp. 659–669, Jun. 2010, doi: 10.1002/jrs.2500.
[99] K. Chen, H. Zhang, H. Wei, and Y. Li, 'Improved Savitzky–Golay-method-based fluorescence subtraction algorithm for rapid recovery of Raman spectra', *Appl. Opt.*, vol. 53, no. 24, pp. 5559–5569, Aug. 2014, doi: 10.1364/AO.53.005559.
[100] M. D. Morris, P. Matousek, M. Towrie, A. W. Parker, A. E. Goodship, and E. R. C. Draper, 'Kerr-gated time-resolved Raman spectroscopy of equine cortical bone tissue', *J. Biomed. Opt.*, vol. 10, no. 1, p. 014014, 2005, doi: 10.1117/1.1827605.
[101] P. Matousek, M. Towrie, and A. W. Parker, 'Fluorescence background suppression in Raman spectroscopy using combined Kerr gated and shifted excitation Raman difference techniques', *J. Raman Spectrosc.*, vol. 33, no. 4, pp. 238–242, Apr. 2002, doi: 10.1002/jrs.840.
[102] G. Rusciano, A. C. De Luca, A. Sasso, and G. Pesce, 'Enhancing Raman Tweezers by Phase-Sensitive Detection', *Anal. Chem.*, vol. 79, no. 10, pp. 3708–3715, May 2007, doi: 10.1021/ac070050n.
[103] J. P. Nolan, E. Duggan, E. Liu, D. Condello, I. Dave, and S. A. Stoner, 'Single cell analysis using surface enhanced Raman scattering (SERS) tags', *Methods*, vol. 57, no. 3, pp. 272–279, Jul. 2012, doi: 10.1016/j.ymeth.2012.03.024.
[104] C. L. Evans, E. O. Potma, M. Puoris'haag, D. Côté, C. P. Lin, and X. S. Xie,

'Chemical imaging of tissue in vivo with video-rate coherent anti-Stokes Raman scattering microscopy', *Proc. Natl. Acad. Sci.*, vol. 102, no. 46, pp. 16807–16812, Nov. 2005, doi: 10.1073/PNAS.0508282102.

[105] C. W. Freudiger *et al.*, 'Label-Free Biomedical Imaging with High Sensitivity by Stimulated Raman Scattering Microscopy', *Science*, vol. 322, no. 5909, p. 1857, Dec. 2008, doi: 10.1126/SCIENCE.1165758.

[106] H. Wang, J. Zhao, A. M. D. Lee, H. Lui, and H. Zeng, 'Improving skin Raman spectral quality by fluorescence photobleaching', *Photodiagnosis Photodyn. Ther.*, vol. 9, no. 4, pp. 299–302, Dec. 2012, doi: 10.1016/j.pdpdt.2012.02.001.

[107] M. A. da S. Martins, D. G. Ribeiro, E. A. Pereira dos Santos, A. A. Martin, A. Fontes, and H. da S. Martinho, 'Shifted-excitation Raman difference spectroscopy for in vitro and in vivo biological samples analysis', *Biomed. Opt. Express*, vol. 1, no. 2, pp. 617–626, Sep. 2010, doi: 10.1364/BOE.1.000617.

[108] S. Guo, O. Chernavskaia, J. Popp, and T. Bocklitz, 'Spectral reconstruction for shifted-excitation Raman difference spectroscopy (SERDS)', *Talanta*, vol. 186, pp. 372–380, Aug. 2018, doi: 10.1016/j.talanta.2018.04.050.

[109] L. F. Santos, R. Wolthuis, S. Koljenović, R. M. Almeida, and G. J. Puppels, 'Fiber-Optic Probes for in Vivo Raman Spectroscopy in the High-Wavenumber Region', *Anal. Chem.*, vol. 77, no. 20, pp. 6747–6752, Oct. 2005, doi: 10.1021/ac0505730.

[110] L. CA, M. SK, B. D, E. DL, and M.-J. A, 'Raman microspectroscopy for skin cancer detection in vitro', *J. Biomed. Opt.*, vol. 13, no. 2, p. 024013, 2008, doi: 10.1117/1.2899155.

[111] J. Zhao, H. Lui, D. I. McLean, and H. Zeng, 'Integrated real-time Raman system for clinical in vivo skin analysis', *Ski. Res. Technol.*, vol. 14, no. 4, pp. 484–492, Nov. 2008, doi: 10.1111/j.1600-0846.2008.00321.x.

[112] Z. Huang, H. Zeng, I. Hamzavi, D. I. McLean, and H. Lui, 'Rapid near-infrared Raman spectroscopy system for real-time in vivo skin measurements', *Opt. Lett.*, vol. 26, no. 22, pp. 1782–1784, Nov. 2001, doi: 10.1364/OL.26.001782.

[113] H. Lui, J. Zhao, D. McLean, and H. Zeng, 'Real-time Raman Spectroscopy for In Vivo Skin Cancer Diagnosis', *Cancer Res.*, vol. 72, no. 10, pp. 2491–2500, May 2012, doi: 10.1158/0008-5472.CAN-11-4061.

[114] J. T. Motz *et al.*, 'Real-time Raman system for in vivo disease diagnosis', *J. Biomed. Opt.*, vol. 10, no. 3, p. 031113, 2005, doi: 10.1117/1.1920247.

[115] A. J. Moy, X. Feng, M. K. Markey, J. S. Reichenberg, and J. W. Tunnell, 'Noninvasive skin cancer diagnosis using multimodal optical spectroscopy', in *Photonic Therapeutics and Diagnostics XII*, Feb. 2016, vol. 9689, p. 968905, doi: 10.1117/12.2211172.

[116] J. Schleusener *et al.*, 'Design and technical evaluation of fibre-coupled Raman probes for the image-guided discrimination of cancerous skin', *Meas. Sci. Technol.*, vol. 25, no. 3, p. 035701, Mar. 2014, doi: 10.1088/0957-0233/25/3/035701.

[117] J. Schleusener *et al.*, 'In vivo study for the discrimination of cancerous and normal skin using fibre probe-based Raman spectroscopy', *Exp. Dermatol.*, vol. 24, no. 10, pp. 767–772, Oct. 2015, doi: 10.1111/exd.12768.

[118] I. A. Bratchenko *et al.*, 'In vivo diagnosis of skin cancer with a portable Raman spectroscopic device', *Exp. Dermatol.*, vol. 30, no. 5, pp. 652–663, May 2021, doi: 10.1111/exd.14301.

[119] P. Zhang, G. Wang, X. Zhang, and Y. Li, 'Single-Acquisition 2-D Multifocal Raman Spectroscopy Using Compressive Sensing', *Anal. Chem.*, vol. 92, no. 1, pp. 1326–

1332, Jan. 2020, doi: 10.1021/acs.analchem.9b04495.
[120] Y. Zhang *et al.*, 'Adaptive compressed sensing of Raman spectroscopic profiling data for discriminative tasks', *Talanta*, vol. 211, p. 120681, May 2020, doi: 10.1016/j.talanta.2019.120681.
[121] F. Sinjab, Z. Liao, and I. Notingher, 'Applications of Spatial Light Modulators in Raman Spectroscopy', *Appl. Spectrosc.*, vol. 73, no. 7, pp. 727–746, Jul. 2019, doi: 10.1177/0003702819834575.
[122] Z. J. Smith, S. Strombom, and S. Wachsmann-Hogiu, 'Multivariate Optical Computing for Biological Samples using a Digital Micromirror Device', in *Frontiers in Optics 2011/Laser Science XXVII*, 2011, vol. 19, no. 18, pp. 16950–16962, doi: 10.1364/FIO.2011.FTuO4.
[123] Z. Liao, F. Sinjab, G. Gibson, M. Padgett, and I. Notingher, 'DMD-based software-configurable spatially-offset Raman spectroscopy for spectral depth-profiling of optically turbid samples', *Opt. Express*, vol. 24, no. 12, p. 12701, Jun. 2016, doi: 10.1364/OE.24.012701.
[124] F. Sinjab *et al.*, 'Tissue diagnosis using power-sharing multifocal Raman micro-spectroscopy and auto-fluorescence imaging', *Biomed. Opt. Express*, vol. 7, no. 8, pp. 2993–3006, Aug. 2016, doi: 10.1364/BOE.7.002993.
[125] D. Cebeci, B. Mankani, and D. Ben-Amotz, 'Recent Trends in Compressive Raman Spectroscopy Using DMD-Based Binary Detection', *J. Imaging*, vol. 5, no. 1, pp. 1–15, Dec. 2018, doi: 10.3390/jimaging5010001.
[126] C. Scotté *et al.*, 'Assessment of Compressive Raman versus Hyperspectral Raman for Microcalcification Chemical Imaging', *Anal. Chem.*, vol. 90, no. 12, pp. 7197–7203, Jun. 2018, doi: 10.1021/acs.analchem.7b05303.
[127] O. G. Rehrauer, V. C. Dinh, B. R. Mankani, G. T. Buzzard, B. J. Lucier, and D. Ben-Amotz, 'Binary Complementary Filters for Compressive Raman Spectroscopy', *Appl. Spectrosc.*, vol. 72, no. 1, pp. 69–78, Jan. 2018, doi: 10.1177/0003702817732324.
[128] Avantes, 'Understanding Spectrometer Resolution Specifications - Avantes'. https://avantesusa.com/understanding-spectrometer-resolution-specifications/ (accessed Sep. 05, 2021).
[129] J. Balsam, H. A. Bruck, Y. Kostov, and A. Rasooly, 'Image stacking approach to increase sensitivity of fluorescence detection using a low cost complementary metal-oxide-semiconductor (CMOS) webcam', *Sensors Actuators B Chem.*, vol. 171–172, pp. 141–147, Aug. 2012, doi: 10.1016/j.snb.2012.02.003.

APPENDIX A - DEVELOPMENT AND DESIGN OF THE 3D OBJECTS

In the work, several mechanical parts were developed to allow an alignment with low tolerances for positional variations and the minimum number of degrees of freedom required. The 3D objects created were: the Universal Sample Cage (USC) System (already presented in chapter 3 – Materials and Methods, section 3.3.1), the Detector Fixation System (DFS) and the lasers and lamp supports, which will be addressed in this Appendix.

The mechanical parts were designed in the *Autodesk Inventor Professional 2021* software. Then, the files were edited into the *Ultimaker Cura 4.8.0* software, associated with the A *3D printer Ultimaker 2+* where they were made. In this software is it possible to choose some properties related to the specified printing, such as the profile, the material used, the speed, among others. The material used to imprint all the parts was Polylactic acid (PLA) material.

A.1. Laser's Supports

A collimated beam is obtained when the initial laser position is fixed, and the laser projection angle is zero. However, sometimes, this angle can be slightly deviated, and therefore it is important to compensate it so that the final beam is the most constant in size and height throughout the entire assembled system. With this in mind, bases were designed for each laser used.

A.2.1. - JDS Uniphase Helium Neon Gas Laser

The base created to support the red laser of excitation wavelength of 632.8 nm (JDS Uniphase) was designed in order to verify some prerequisites:

- a rail that allowed to efficiently fit a screw with a nut to fix it.

- two stable bases with a thread each, so that both can be connected to a BE1 Thorlabs Adapter ring. This ring was fixed to the optical table with a CF175 Thorlabs table clamping fork, which allows the laser to be independent of the horizontal alignment in the optical table.

The result of the designed part for this laser is presented in Figure A.1.

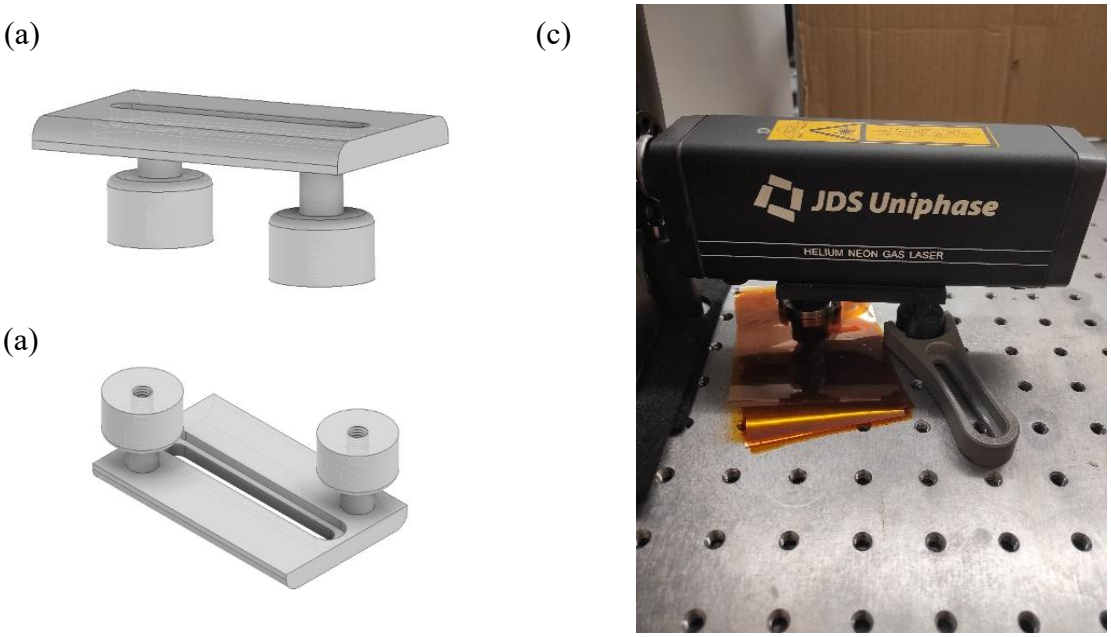

Figure A.1 – Design of the base for JDS Uniphase laser. Front view (a) and top view (b), where the rail and the two bases with treads can be seen. Photo of the laser with the printed base with the ring adapter and table clamping forks to immobilize the system (c).

A.2.2. - Bioray Coherent Laser Diode

The base design to fix the red laser of excitation wavelength of 640 nm is an adapter to an original connector of the laser fixation system. The 3D object is attached to the laser connector with 4 mm screws in the extremity's holes designed in the superior face of the base (Figure A.2).

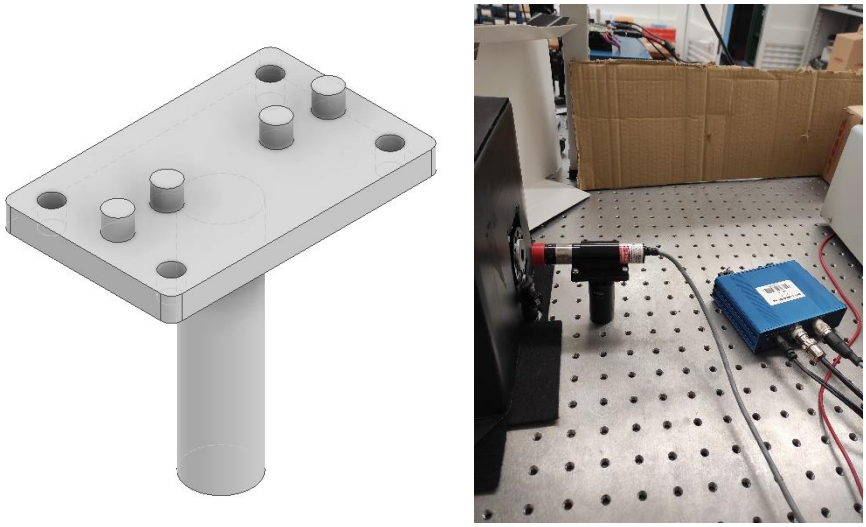

Figure A.2 – Design of the Bioray Coherent laser diode base (left). Assembly of the imprinted object in the optical table, with a compatible post holder (right).

The main feature of this base is the possibility to adjust the height of the laser through the lifting of the post in the compatible post holder. Furthermore, it allows the horizontal rotation of the laser in order to improve the final collimation of the exit laser beam.

A.2. Detection Fixation System (DFS)

Due to the need to immobilize the detection system, a camera position correction system was designed to allocate the camera, eliminating its degrees of freedom, and thus not allowing the camera's field of view to vary, as represented in Figure A.3 (c). Hence, the so called Detection Fixation System (DFS) is composed of three individual parts: two side pieces – as shown in Figure A.3 (a) - to cancel the rotation angle and a lower piece to fix the camera to a post - represented in Figure A.3 (b) - to obtain a camera's constant height.

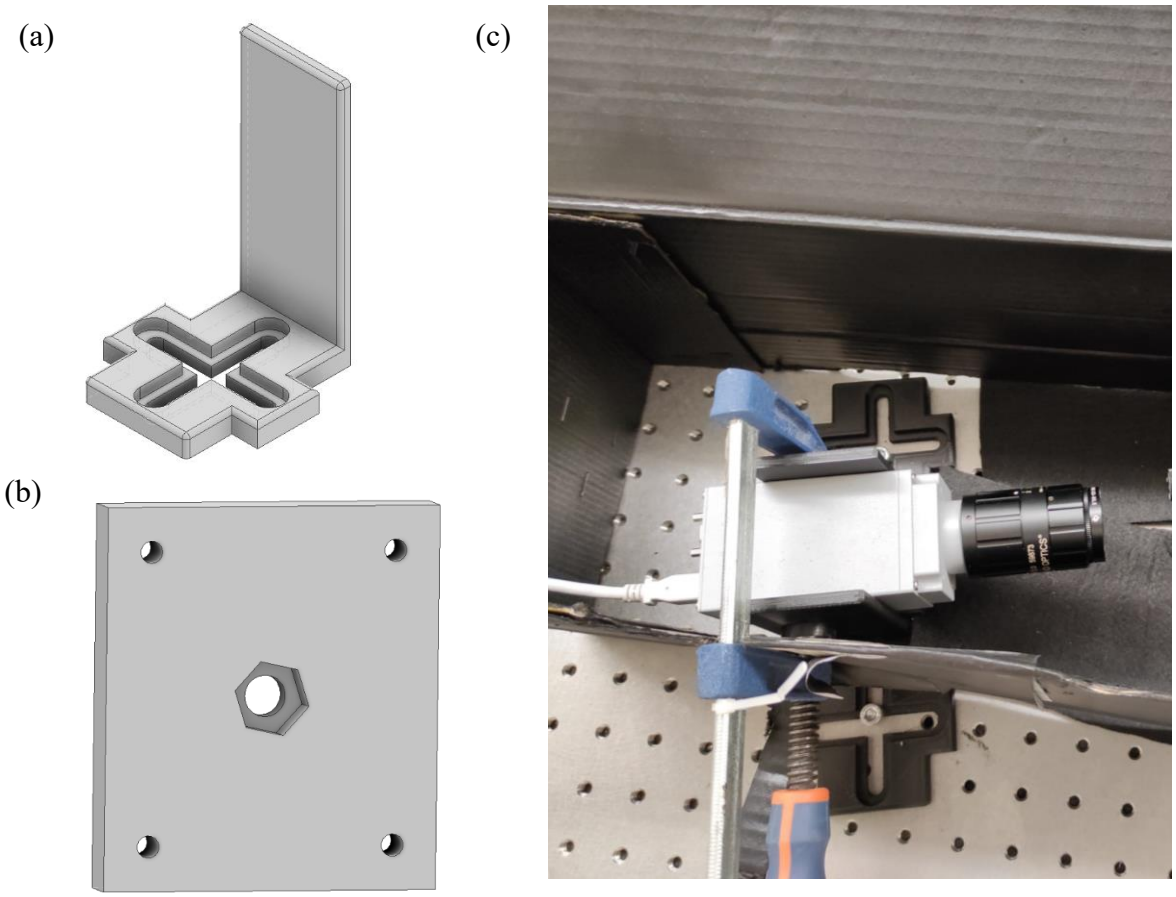

Figure A.3 – Detector Fixation system (DFS) included two lateral parts, in (a), and a base to attach the camera to a post and post holder, in (b). DFS implemented in the prototype assembly, in (c).

A.3. Halogen Lamp Post

In addition to the parts seen before, a final part was also designed in order to place the halogen lamp (Figure A.4). This adapter immobilizes the lamp, as well as functioning as its post, being inserted in the sample post holder. However, since the halogen lamp is only used in the Coarse alignment it will be not needed further and will be substituted by the USC system.

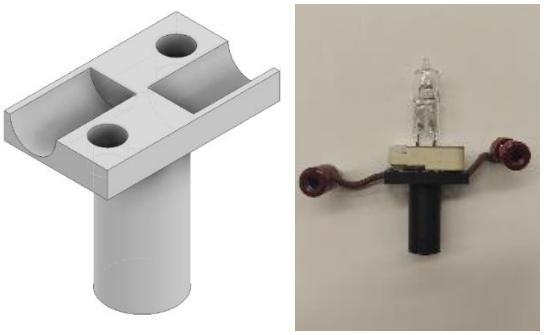

Figure A.4 – Halogen Lamp mount adapter.

APPENDIX B - POWER METER DEVICE

To measure the signal power of the laser or through the several optical elements in the setup, a power meter was built. Thereby, setup optimization and the minimization of signal losses within the optical system elements was possible.

The power meter is composed of a photodiode power sensor (S130C, Thorlabs), which delivers a current, dependent on the wavelength and input power according to equation B.1, connected to a transimpedance amplifier circuit, present in Figure B.1, to convert the input current source into an output voltage, and finally, an *Arduino* that reads the analogue value and converts it to a meaningful value of power, which the operator can read and interpret.

$Responsivity\ (\lambda) = {}^{I_{pd}}/_{P}$, with I_{pd} equals to photodiodes' photocurrent (in this sensor: 4.117mA) and P the incident light power. (B.1)

Transimpedance amplifier: This circuit is composed of an operational amplifier (Op-amp) coupled in negative feedback to a resistor ($R_1 = 1.2k\Omega$) and a capacitor ($C_1 = 220nF$) connected in parallel between the amplifier negative input and the output side of the Op-amp (Vout). The circuit is fed by a current source (Photodiode) in the positive pin of the Op-amp (Figure B.1). To stabilize the circuit bandwidth the capacitor value is given by the following equation:

$C_1 \leq \frac{1}{2\pi\ x\ R_1\ x\ f_{bf}}$, where f_{bf} is the required bandwidth frequency. (B.2)

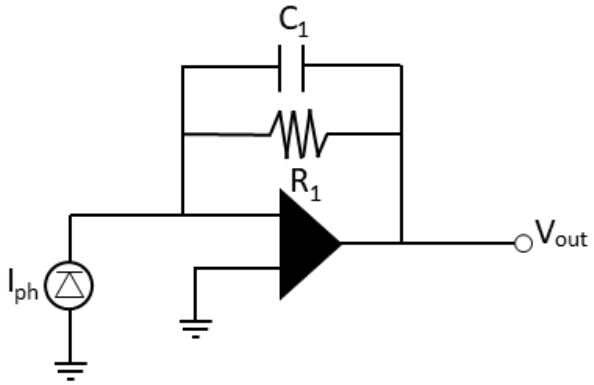

Figure B.1 - Transimpedance Amplifier Circuit. Capacitor (C_1), Resistance (R_1), Photodiode (I_{ph}) Output voltage (V_{out}).

Arduino: Firstly, the serial communication at 9600 bits per second is initiated, and then an infinite loop is started. The centre pin of the potentiometer is attached to pin A0 of Arduino Nano, and the outside pin is on +5V and ground pins. The analogue input (voltage), K, is continuously read on pin 0 and converted to a number between 0 and 1023, which is proportional to the voltage applied to the pin. Then, this value is transformed by the *analogRead()* function delivering a voltage, from 0 to 4.8V, in order to avoid saturation ($Voltage = K * 4.8/1023$).

Then, since the photodiode sensor is wavelength dependent, the power value is computed, using equation B.3, and printed on the serial monitor of the *Arduino* software. To do so, the manufacturer supplied a datasheet with the calibrated values of responsivity vs. wavelengths. Consequently, according to the excitation wavelength of the laser used, the responsivity value should be written in the Arduino console.

$$Power = \frac{Voltage/R_1}{Responsivity\ (\lambda)} \tag{B.3}$$

The result of the built-in power meter is represented in Figure B.2.

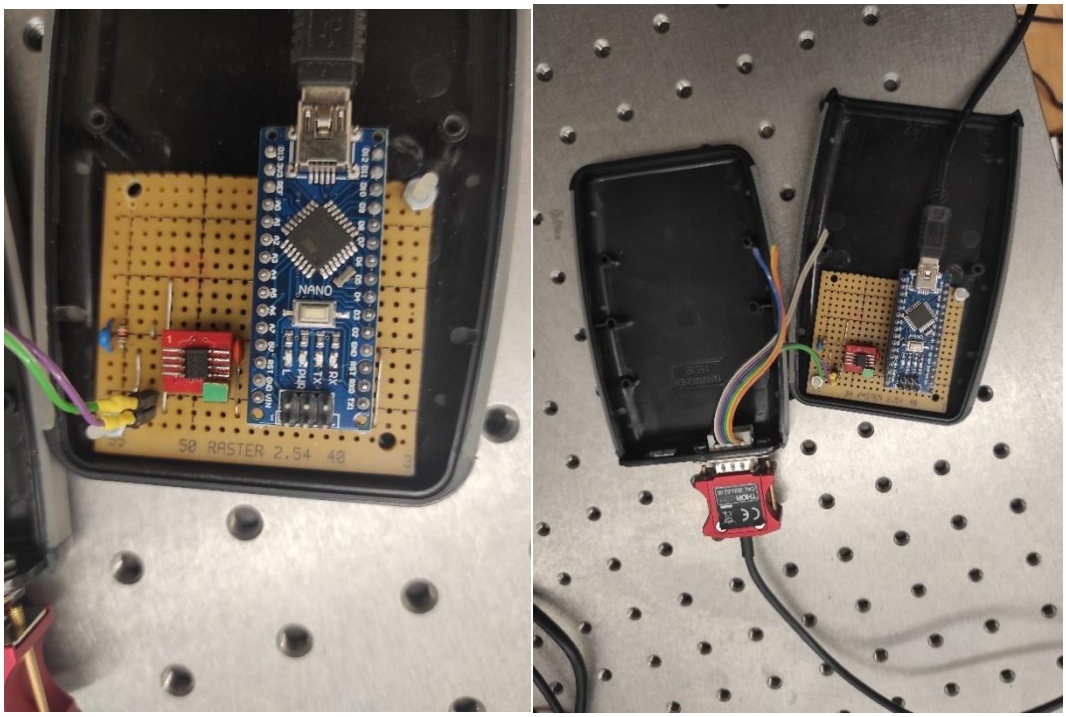

Figure B.2 – Developed power-meter instrument.

APPENDIX C – OPTICAL FIBRE SYSTEM

A Fibre Optic System (OFS) was assembled in order to simulate a sample that emits visible light (red in this case), to facilitate the alignment of the optical system components of the transmission branch and the spectrograph of the prototype developed in this dissertation.

The OFS, represented by the letter "m" in Figure C.1, was composed of three 30 mm^2 cages with Ø 25.4 mm of diameter, which incorporates: 1st cage - a red laser of 635nm (Bioray Coherent laser diode, PN: 0221-700-01); 2nd cage - an 11 mm focal length lens (C220TME-C Thorlabs) was incorporated to focus the laser light into the optical fibre; 3rd cage - an optical fibre of 62.5±2.5 µm core diameter with FC/PC connectors attached in the endings of the fibre (M31L03, Thorlabs). Additionally, each ending of the optical fibre had a cylindrical metallic adapter of Ø 11 mm of diameter coupled with the FC/PC connector.

Therefore, to undertake a system with high movement stability two cylindric adapters, described in section 3.3.1.1 from the optical fibre (represented by letter 'f' in the figure), were designed to connect to the OFS system (letter 'm' in the figure) and another adapter to place the fibre in the sample cage holder (USC) (letter 's' in the figure).

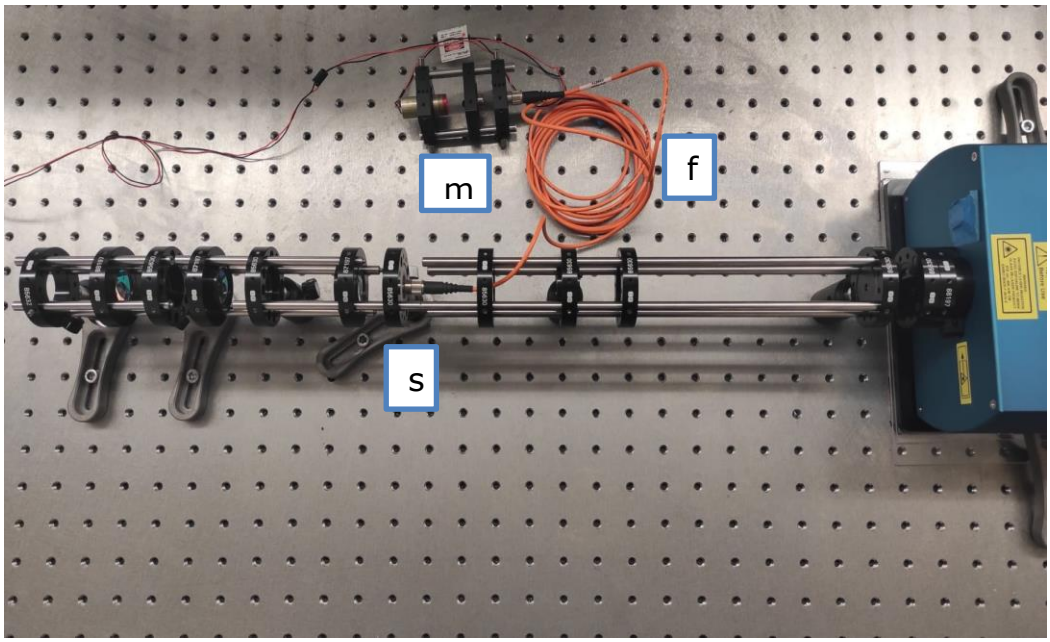

Figure C.1 – Optical Fibre System, OFS, ('m') with the optical fibre ('f'), and fibre-coupled into the sample mount ('s').

APPENDIX D – COMPRESSIVE RAMAN SYSTEM

A compressive SWIR-Raman spectrometer is the ultimate goal of this project, in order to apply it to early melanoma diagnosis in the clinical setting avoiding tissue-autofluorescence. This configuration is simpler, allows fast acquisitions, as well as being inexpensive.

Minor differences are needed to change the already developed Raman spectrometer into a compressive SWIR-Raman spectrometer, as represented in Figure D.1 (left side), which are:

(i) changing the configuration from transmission geometry to reflection to apply RS to biological applications, as already simulated in the *software 3DOptix* and, also, implemented in the optical table as represented in Figure D.1 (right side);

(ii) and, substituting the detector system for a DMD and an InGaAs photodiode (represented by (3) in Figure D.1). The DMD will permit subsampling of the spectra of lesions and so fast acquisition times, hence will make the device applicable for clinical setting diagnosis. The NIR-laser and the HWVN are extremely important to avoid tissue autofluorescence. Therefore, a detector with a detection range above 1100 nm is needed, such as InGaAs photodiode, due to having a wider detection range (up to 2500 nm). This will allow the detection of the HWVN spectral region, for instance, 1300 to 1550 nm, *i.e.*, the ROI for differentiating melanoma and benign melanocytic lesions, using a NIR-laser.

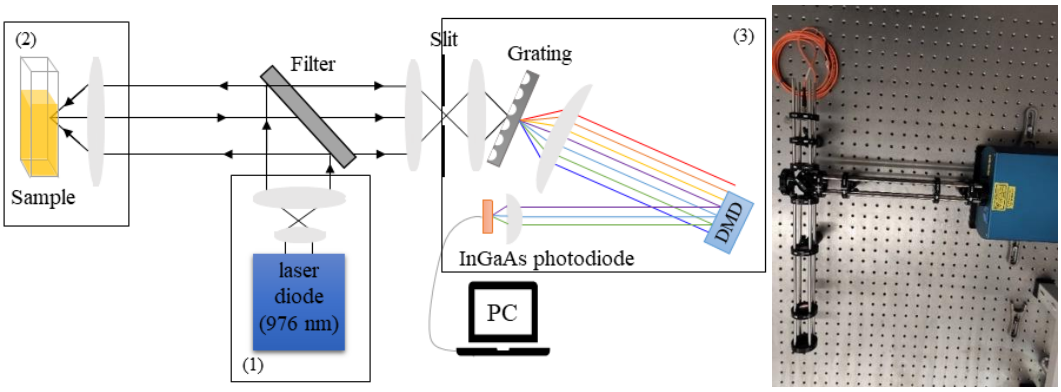

Figure D.1 – (left) Simplified schematics of the compressive Raman instrument configuration. (right) Physical setup of a reflection configuration.